Fakultät für Physik und Astronomie

Ruprecht-Karls-Universität Heidelberg

Diplomarbeit

im Studiengang Physik

vorgelegt von

Felix Kahlhöfer

geboren in Bergisch Gladbach

2010

Sensitivität von

Flüssig-Xenon-Detektoren

für Leichte Dunkle Materie

Die Diplomarbeit wurde von Felix Kahlhöfer

ausgeführt am

Max-Planck-Institut für Kernphysik

unter der Betreuung von

Herrn Prof. Manfred Lindner

Department of Physics and Astronomy

University of Heidelberg

Diploma thesis

in Physics

submitted by

Felix Kahlhoefer

born in Bergisch Gladbach

2010

Sensitivity of Liquid Xenon Detectors

for Low Mass Dark Matter

This diploma thesis has been carried out by Felix Kahlhoefer

at the

Max-Planck-Institut fuer Kernphysik

under the supervision of

Prof. Manfred Lindner

Sensitivität von Flüssig-Xenon-Detektoren für Leichte Dunkle Materie

Experimente zum direkten Nachweis von dunkler Materie auf der Basis von Flüssig-Xenon-Detektoren zählen zu den vielversprechendsten Strategien um die Eigenschaften der dunklen Materie zu ergründen. In dieser Arbeit erörtern wir die Sensitivität solcher Detektoren für Kernrückstöße mit einer Energie unter 10 keV, wie man sie für Dunkle-Materie-Teilchen mit einer Masse von weniger als 10 GeV erwartet. Das Interesse an leichter dunkler Materie rührt her von der angeblichen Beobachtung eines entsprechenden Signals in den beiden Experimenten DAMA und CoGeNT. In dieser Diplomarbeit zeigen wir, dass auch Flüssig-Xenon-Detektoren wie XENON100 in der Lage sein sollten, solche leichte dunkle Materie zu beobachten, und somit die laufende Diskussion beilegen können. Zuerst betrachten wir die Detektorauflösung und bestimmen die Akzeptanz von Flüssig-Xenon-Detektoren im Bereich niedriger Energien. Anschließend beschäftigen wir uns mit der Produktion und dem Nachweis von Szintillationslicht in flüssigem Xenon und berechnen dazu die relative Szintillationseffizienz. Außerdem führen wir Monte Carlo Simulationen durch, um die Lichtsammeleffizienz eines vorgegebenen Detektors vorherzusagen. Zum Abschluss diskutieren wir die Phänomenologie für den direkten Nachweis von fermionischer dunkler Materie. Dazu berechnen wir die Wirkungsquerschnitte für die Streuung von dunkler Materie an Atomkernen in verschiedenen Modellen und bestimmen die resultierenden Ausschlussbereiche aktueller Experimente.

Sensitivity of Liquid Xenon Detectors for Low Mass Dark Matter

Dark matter direct detection experiments based on liquid xenon detectors are one of the most promising strategies to determine the nature of dark matter. In this thesis, we discuss the sensitivity of such detectors for nuclear recoils with energy below 10 keV corresponding to dark matter particles with a mass of less than 10 GeV. The interest in low mass dark matter has been roused by the claimed observation of a corresponding signal in the experiments DAMA and CoGeNT. We demonstrate that liquid xenon detectors like XENON100 should also be able to observe such low mass dark matter particles and can consequently settle the present discussion. First, we discuss the detector resolution and determine the acceptance of liquid xenon detectors in the low energy region. Next, we analyze the production and detection of scintillation light in liquid xenon, calculating the relative scintillation efficiency. Moreover, we perform Monte Carlo simulations to predict the light collection efficiency for a given detector. Finally, we discuss the phenomenology of direct detection for fermionic dark matter. We calculate the cross sections for the interaction between dark matter and nuclei in different models and give the corresponding exclusion limits of recent experiments.

Contents

Poets say science takes away from the beauty of the stars — mere globs of gas atoms. I too can see the stars on a desert night, and feel them. But do I see less or more? The vastness of the heavens stretches my imagination — stuck on this carousel my little eye can catch one-million-year-old light. A vast pattern — of which I am a part... What is the pattern, or the meaning, or the why? It does not do harm to the mystery to know a little about it. For far more marvelous is the truth than any artists of the past imagined it.

(Richard Feynman)

Acknowledgments

First of all, I thank Manfred Lindner for giving me the opportunity to write this diploma thesis. It was him who first directed my attention to the topic of dark matter and who introduced me to the XENON Collaboration. I am very grateful for his guidance and his encouragement. Moreover, I would like to thank Manfred Lindner for offering me the possibility to visit the Gran Sasso Underground Laboratory and to attend the Workshop on the Interconnection between Particle Physics and Cosmology (PPC 2010) in Turin, which have been great experiences from both personal and scientific point of view.

Next, it is a pleasure to thank those people who have collaborated with me on different parts of my thesis and supervised my work. I thank Fedor Bezrukov for the very productive collaboration on the relative scintillation efficiency of liquid xenon and some very inspiring discussions. I have benefited a lot from his wide knowledge. I also thank Thomas Schwetz for all the insight he has shared with me on the phenomenology of dark matter and the analysis of direct detection experiments. Moreover, I would like to express my gratitude that he shared with me his program codes to calculate exclusion limits, and for his idea to attempt a general operator analysis of four-fermion interactions. Also, I am indebted to Hardy Simgen for initiating me into the world of experimental physics, more precisely the XENON technology, and for his help with Geant4. In this context, I would also like to thank Marc Weber and Sebastian Lindemann, who have made available their support on many occasions. Most notably, I am grateful for the inspiring collaboration with Marc on the Monte Carlo simulations of the nuclear recoil band.

Furthermore, this thesis would not have been possible without the help and support of the entire XENON Collaboration, most notably Rafael Lang, Teresa Marrodan-Undagoitia, Alexander Kish, Emilija Pantic, Marc Schumann, and Laura Baudis, who have repeatedly given me advice and answered my questions. I am grateful that the collaboration allowed me to participate in the weekly teleconferences and the XENON1T meeting in Heidelberg. I especially thank Rafael Lang for various helpful discussions and his great patience.

I am deeply thankful for having had so many nice people around during my time at the Max-Planck-Institut für Kernphysik. First of all, I would like to show my gratitude to my office mates Nico Kronberg and Julian Heeck, not only for answering an

Introduction

To observe the motion of astrophysical objects and understand the laws that describe their trajectories has traditionally been one of the central interests of physicists. It has led to the discovery of the laws of gravitation, the confirmation of the theory of general relativity, and to our present understanding of the universe. At the same time, such observations still raise questions that we cannot yet answer. In 1933, Zwicky observed that the velocity distribution of galaxies in the Coma cluster cannot be explained by the gravitational potential inferred from the luminous matter alone. The observation that large amounts of non-luminous matter, so-called *dark matter*, must be present in the universe has been confirmed many times since then — but our understanding of the nature of this dark matter has made only little progress.

Today, the central strategy of astrophysics is the spectral analysis of radiation from different kinds of sources. This strategy has led to the discovery of Hubble's law of the expansion of the universe and to the understanding of the Cosmic Microwave Background (CMB). Together, these observations build the foundations of our modern understanding of cosmology, the so-called Big Bang scenario. We now have a highly sophisticated model, called ΛCDM, that can explain a large variety of astrophysical observations with only six parameters.

The parameters of ΛCDM can be determined from a global analysis of experimental data. The results imply that baryons, the constituents of ordinary matter, contribute only 4–5% to the energy density of the universe. Dark matter, in fact, is far more abundant, accounting for approximately 23% of the energy density. The remaining 72% are not matter at all but vacuum energy, also known as dark energy. On the one hand, these results strongly confirm the observation that dark matter must be present in the universe. On the other hand, we must admit that the great success of ΛCDM implies that we only understand a tiny fraction of the content of the universe. The remainder is dark, meaning that it eludes conventional detection techniques.

Over the past few decades, the puzzle of dark matter has gained more and more interest. The reason is that dark matter turns out to be closely related to central problems of particle physics. In fact, the most promising models that extend the Standard Model of particle physics in order to solve the hierarchy problem, namely

supersymmetry and extra dimensions, naturally predict a good candidate for the dark matter particle. This connection between modern cosmology and modern particle physics makes the nature of dark matter such a fascinating and important problem.

In this chapter, we will give a general introduction to the topic of this thesis. In section 1.1 we introduce the relevant preliminaries from cosmology and discuss the ΛCDM model. An account of the experimental evidence for dark matter will be given in section 1.2. We will summarize our present knowledge about dark matter and discuss possible models in section 1.3. Finally, in section 1.4, we will connect these general considerations with the topic of this thesis, giving a motivation for and an outline of the following chapters. For a more detailed introduction to the topic of dark matter, we refer to [1–3].

1.1 The standard model of cosmology

Today, most cosmologists agree that the universe has evolved from a singular state, called the Big Bang. Therefore, the universe was extremely dense initially, but has expanded since, and is expected to continue this expansion. In the process, it has undergone various transitions, which we can still trace today, for example nucleosynthesis and recombination. All these observations are well described by the ΛCDM model. The name of the model indicates the necessary ingredients: *Vacuum energy* (described by a cosmological constant Λ) and *Cold Dark Matter*.[1] Only if both of these contribute significantly to the total energy density, we are able to explain the observed history of the universe.

To describe the expansion of the universe since the Big Bang, one introduces a scale factor $a(t)$ with the present value $a_0 = 1$. The rate of expansion is given by the Hubble parameter

$$H(t) \equiv \frac{\dot{a}(t)}{a(t)} \, , \tag{1.1}$$

whose present value (also called the Hubble constant) is $H_0 = 73 \pm 3 \, \mathrm{km \, s^{-1} \, Mpc^{-1}}$. This value can be obtained from Hubble's law by measuring the cosmological redshift z, defined by $1 + z = a_0/a$, for nearby galaxies. Note that H_0 is often quoted in dimensionless form: $h = H_0/100 \, \mathrm{km \, s^{-1} \, Mpc^{-1}} = 0.73 \pm 0.03$.

The time evolution of H is given by the Friedmann equations, which describe the expansion of an isotropic and homogeneous universe as a function of its total energy density ρ_{tot}:

$$H^2 + \frac{k}{a^2} = \frac{8\pi G}{3} \rho_{\mathrm{tot}} \, . \tag{1.2}$$

---

[1]We shall explain what *cold* means in this context in section 1.3.

Here, G is the gravitational constant and k is the spatial curvature, which can be $k = -1$, 0, or 1, corresponding to an open, flat, or closed universe, respectively. If the energy density is equal to the critical value

$$\rho_{\text{tot}} = \rho_{\text{c}} \equiv \frac{3H_0^2}{8\pi G} \, , \tag{1.3}$$

the Friedmann equations describe a flat universe with $k = 0$.

In general, we distinguish different contributions to the total energy density which may have different *equations of state*. An equation of state relates the density ρ_i and the pressure p_i of a substance i. Usually, it has the form $p_i = w\rho_i$, leading to a time evolution of the density given by $\rho_i \propto a^{-3(1+w)}$ [4]. For matter, $w = 0$, so that $\rho_{\text{m}} \propto a^{-3}$. Radiation has $w = 1/3$, so that $\rho_{\text{r}} \propto a^{-4}$ and its density is negligible today. Finally, we include a vacuum energy induced by a cosmological constant Λ, which has $w = -1$ and consequently a density ρ_Λ independent of time. It will be convenient to express each density relative to the critical energy density given in equation (1.3), so we define

$$\Omega_i = \frac{\rho_i}{\rho_{\text{c}}} \, . \tag{1.4}$$

Equation (1.2) can then be written as

$$\left(\frac{H}{H_0}\right)^2 = \Omega_{\text{m}} \left(\frac{a}{a_0}\right)^3 + \Omega_{\text{k}} \left(\frac{a}{a_0}\right)^2 + \Omega_\Lambda \, , \tag{1.5}$$

where $\Omega_{\text{k}} = -k/a_0^2 H_0^2$ and $\Omega_\Lambda = \Lambda/3H_0^2$. The matter energy density Ω_{m} can be split into two parts, $\Omega_{\text{m}} = \Omega_{\text{b}} + \Omega_{\text{CDM}}$, where Ω_{b} is the baryon density and Ω_{CDM} is the cold dark matter density. In the following section, we shall see that Ω_{CDM} contributes significantly (in fact dominantly) to the total amount of matter.

1.2 Observational evidence for dark matter

In general, there are two ways to explain a discrepancy between the expected and the observed trajectories of gravitationally interacting objects: We can either change the amount of gravitating matter by introducing dark matter, or we can modify the laws of gravity. The second approach, known as *Modified Newtonian Dynamics*, has repeatedly been suggested as an alternative to dark matter. The idea is to introduce a new large scale, above which the gravitational force deviates from its known form. However, evidence for dark matter can be observed at very different scales, so it is difficult to explain all observations with a single new scale. Without striving for completeness, we will review the most important of these observations, starting at the smallest scale, the scale of galaxies.
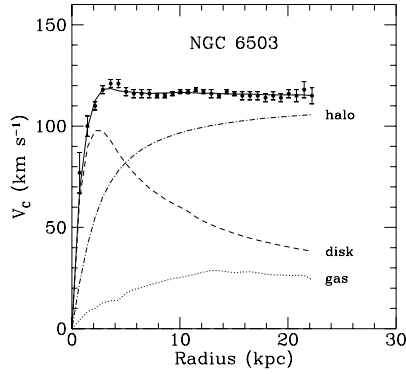
Figure 1.1: Rotation curve of NGC 6503. The dotted, dashed, and dash-dotted lines are the contributions of gas, disk, and dark matter, respectively. Figure taken from [5].
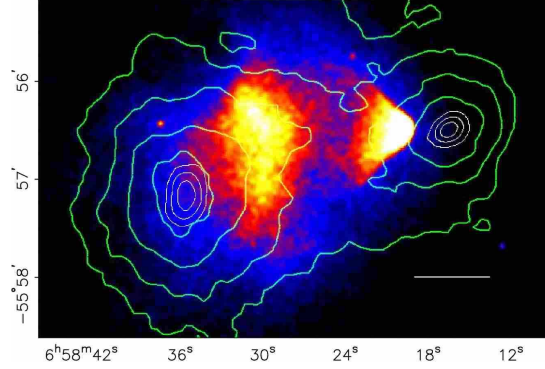
Figure 1.2: The Bullet Cluster 1E0657-558 — a collision of two clusters. The colored picture is an x-ray image of the visible matter, the green contours show the distribution of the total mass inferred from gravitational lensing. One observes a clear discrepancy between visible and gravitating matter. Figure taken from [6].

The most convincing evidence for dark matter on galactic scales comes from the observation that the outer regions of galaxies are rotating faster than expected from the laws of gravitation. According to Newtonian dynamics, one would expect that

$$
v_{\mathrm{rot}}(r) = \sqrt{\frac{GM(r)}{r}} \, , \tag{1.6}
$$

where $M(r)$ is the integral of the galaxy's mass density from 0 to r. Without dark matter, $M(r)$ should be constant beyond the optical disc, and consequently $v(r) \propto r^{-1/2}$ for large r. However, systematic measurements of *rotation curves*, meaning the velocities of stars and gas as a function of their radial distance from the galactic center, give a quite different picture. One observes a constant $v(r)$ at large distances [5], indicating that the mass density $M(r)$ must increase proportional to r even in regions where no luminous matter is observed (see figure 1.1).

The conclusion of this observation is that galaxies must have a non-luminous mass component having $\rho(r) \propto r^{-2}$ at large distances. This component is often referred to as the *dark matter halo* of a galaxy. While evidence for dark matter halos has been collected for a large number of galaxies, including elliptical galaxies, dwarf spheroidal galaxies, and spiral galaxy satellites (see [1] for further references), their precise form and density distribution is still unknown and subject to intense discussion.

Similar observations can be made on the scale of galaxy clusters, for example by comparing the temperature of a cluster with the observed amount of luminous mass. Another very impressive piece of evidence comes from gravitational lensing

data, which determine the mass of a cluster from the distortion of the images of background objects. Such measurements allow to demonstrate clearly the mismatch between the distribution of visible and gravitating matter (see figure 1.2).

Nevertheless, the observations discussed so far do not allow for a determination of the total amount of dark matter in the universe, namely Ω_{CDM}. This quantity, as well as the other contributions to the total energy density can, however, be measured on cosmological scales. The most precise results come from the analysis of the *Cosmic Microwave Background*. The most recent measurements of the *Wilkinson Microwave Anisotropy Probe* (WMAP7) give [7]

$$\Omega_\Lambda = 0.734 \pm 0.029 \tag{1.7}$$
$$\Omega_{\mathrm{CDM}} = 0.222 \pm 0.026 \tag{1.8}$$
$$\Omega_{\mathrm{b}} = 0.0448 \pm 0.0028 \ . \tag{1.9}$$

Note that these results imply that $\Omega_{\mathrm{m}} + \Omega_\Lambda \approx 1$ and $\Omega_{\mathrm{k}} \approx 0$, meaning that we appear to live in a spatially flat universe. We conclude that only about a quarter of the total energy density of the universe is due to matter. And again less than a quarter of the total matter content of the universe is baryonic. A similar value for Ω_{b} is independently obtained from Big Bang nucleosynthesis. We have to conclude that most of the matter in the universe is made out of particles that we have not yet been able to observe.

1.3 Theory of dark matter

In spite of the strong evidence for dark matter at very different scales, the nature of the dark matter particle remains unknown. In this section, we summarize our present knowledge about the properties that any candidate for the dark matter particle must possess. The most important requirement is that a sufficiently large abundance of the particle is produced in the early universe so that it can account for the observed dark matter density. From this consideration, it turns out that none of the known particles of the Standard Model can form the main constituent of dark matter. Consequently, we have to look at possible new particles which arise in extensions of the Standard Model.

1.3.1 Relic densities

In the early universe, all particle species are expected to be in thermal equilibrium, meaning that the number density n^{eq} of a particle with mass m_χ and g degrees of freedom is given by

$$n^{\mathrm{eq}} = g \left(\frac{m_\chi T}{2\pi} \right)^{3/2} \mathrm{e}^{-m_\chi/T} \ , \tag{1.10}$$

where T is the temperature. As the universe expands and cools down, T drops below m_χ. At this point, the number of particles becomes Boltzmann suppressed, so that annihilations of particles of this species become less likely. As soon as the interaction rate of the particle species becomes smaller than the expansion rate of the universe, it will fall out of local thermodynamic equilibrium. It will decouple and form a thermal relic. The temperature at which this decoupling happens is called the *freeze-out temperature* T_F.

We can calculate the density of such a thermal relic starting from the Boltzmann equation, which reads in this case

$$\frac{\mathrm{d}n}{\mathrm{d}t} + 3Hn = -\langle \sigma v \rangle \left(n^2 - (n^{\mathrm{eq}})^2 \right) \ , \tag{1.11}$$

where $\langle \sigma v \rangle$ is the thermal average of the total annihilation cross section of the particle multiplied by its velocity. For heavy particles, $\langle \sigma v \rangle$ can be expanded in powers of v^2 to give

$$\langle \sigma v \rangle = a + b \langle v^2 \rangle + \mathcal{O}(\langle v^4 \rangle) \ . \tag{1.12}$$

Without going through the details of the calculation, we give the final result for the relic density:

$$\Omega_\chi h^2 \approx \frac{1.07 \cdot 10^9 \, \mathrm{GeV}^{-1}}{M_{\mathrm{Pl}}} \frac{x_F}{\sqrt{g_*}(a + 3b/x_F)} \ . \tag{1.13}$$

Here, $x_F = m_\chi / T_F$, M_{Pl} is the Planck mass and g_* counts the number of relativistic degrees of freedom at $T = T_F$. x_F is not easy to determine exactly, but in most cases roughly given by $x_F \approx 20$. In [1], the authors give a simplified version of equation (1.13):

$$\Omega_\chi h^2 \approx \frac{3 \cdot 10^{-27} \, \mathrm{cm}^3 \, \mathrm{s}^{-1}}{\langle \sigma v \rangle} \ . \tag{1.14}$$

For any proposed dark matter candidate, we can use this formula to see whether Ω_χ matches with the expected value for Ω_{CDM}. However, there are more requirements besides the correct abundance that a dark matter candidate must fulfill.

1.3.2 Dark matter properties

First of all, we know from the CMB that most of dark matter must be *non-baryonic*. Baryonic dark objects, usually called Massive Compact Halo Objects (MACHOs), for example brown dwarf stars or large gas giants like Jupiter, are known to exist, but contribute only a small fraction to the total amount of dark matter. From primordial nucleosynthesis and the Lyman alpha forest, we can also exclude diffuse baryons as

the main constituent of dark matter.

Moreover, we know that dark matter should be *collisionless* (for example to explain the observation of the Bullet Cluster in figure 1.2). Finally, to account for the observed abundance, it must either be *stable* or have a lifetime that is large compared to the age of the universe.

From these considerations, neutrinos may seem like the perfect candidate for dark matter, since we know that they are massive and interact only weakly. Clearly, neutrinos do contribute to the total amount of dark matter. However, there are two problems with neutrinos. First, it turns out that they are simply not abundant enough to be the dominant component of dark matter, unless there is a different mechanism to produce them. The greater problem is that, because of their low mass, neutrinos were still relativistic when they decoupled from thermal equilibrium. Such relativistic dark matter particles are referred to as *hot dark matter*. Large amounts of hot dark matter tend to erase local density fluctuations in the universe and therefore prevent the formation of small-scale structures. Therefore, we know that light neutrinos cannot account for all of the dark matter.

1.3.3 Candidates for dark matter

Whatever is the dominant component of dark matter, it must be cold (meaning non-relativistic), collisionless, stable and non-baryonic [8]. Excellent candidates for dark matter are so-called *Weakly Interacting Massive Particles* (WIMPs). Like neutrinos, these particles have only weak interactions with ordinary matter but their mass is much larger. In fact, it would be natural for such a particle to have a mass around the electroweak scale, meaning $m_\chi \approx 100 - 1000 \,\mathrm{GeV}$. On dimensional grounds, the cross section of such a particle should then be

$$\langle \sigma v \rangle \approx \frac{g_{\mathrm{weak}}^4}{16\pi^2 m_\chi^2} \ . \tag{1.15}$$

Substituting this expression into equation (1.14), we indeed get the correct order of magnitude for Ω_χ. Weak-scale particles automatically have the correct relic density and consequently make excellent candidates for dark matter. This observation is known as the *WIMP miracle*.

The second reason for the great popularity of WIMP candidates for dark matter is that they arise naturally in extensions of the Standard Model. Almost all theories that attempt to solve the gauge hierarchy problem introduce new particles at the electroweak scale. If one of these particles can be made stable, it is automatically a good candidate for dark matter. In supersymmetric extensions of the Standard Model, this particle would be the lightest supersymmetric particle, which is usually expected to be the neutralino. In models with universal extra dimensions one similarly obtains a stable heavy particle, the lightest Kaluza-Klein particle.

However, it is certainly not necessary that the dark matter particle is a WIMP. Viable candidates, which are well motivated by extensions of the Standard Model, include gravitinos, axions and sterile neutrinos. These candidates have in common that they all have much smaller masses and much weaker interactions than WIMPs and are consequently extremely difficult to detect experimentally. Of course, many more candidates for dark matter have been proposed and it is beyond the scope of this thesis to mention all of them. Nevertheless, the point we wish to make is that although WIMPs are the most attractive candidates for dark matter, one should be open-minded towards alternatives.

1.4 Motivation and outline

The identity of dark matter is one of the central problems of modern physics. Many experiments have been performed, are currently running or will be built to solve it. So far, most experiments have only given null results, allowing to exclude some dark matter candidates and set strong bounds on others. Those experiments, which actually have observed a signal that may be due to dark matter, give a contradictory and even more puzzling picture (see chapter 2.3). Recent observations indicate that the dark matter mass may be much smaller than the weak scale — in conflict with the WIMP idea. It will be the task of present and future dark matter experiments to confirm or refute this observation, and the task of theoretical physicists to refine existing models or propose new ones to consistently interpret experimental data.

In this thesis, we want to discuss and examine possible ways to shed light on the mysteries of dark matter. If the dark matter particle is a WIMP, direct detection experiments based on liquid xenon have a good chance to detect it. We want to demonstrate that — in contrast to recent claims [9] — they are also highly competitive for the detection of dark matter with lower mass. Consequently, it is reasonable to expect that within the near future, liquid xenon detectors will either observe a dark matter signal or exclude current experimental claims with high significance.

In chapter 2, we discuss experimental strategies to detect dark matter. The focus of this thesis is on direct detection experiments, which attempt to observe dark matter interactions in low background underground detectors. We discuss the expected experimental signatures and how they depend on the dark matter properties and astrophysical input. Moreover, we give an overview over present direct detection experiments and recent notable results, with a special emphasis on the XENON experiment.

Then, in chapter 3, we go into more detail on the expected performance of XENON100. This performance depends crucially on the sensitivity of the detector at low energies. Consequently, we discuss the low energy threshold and the energy resolution of the detector. We also estimate the fluctuations of the expected signals, and determine the detector acceptance at low recoil energies.

Another important open question related to the performance of the XENON100 experiment concerns the relative scintillation efficiency of nuclear recoils in liquid xenon. Experiments currently disagree on the behavior of this quantity at low energies. In chapter 4, we first review existing theoretical models for the processes that lead to the production of scintillation light, and then present our own calculation of the relative scintillation efficiency.

In chapter 5, we turn to future experiments based on the liquid xenon technology. Our goal is to estimate the sensitivity of such experiments, again with a special focus on the low energy region. Using Monte Carlo simulations, we can determine the light yield for different potential detector designs and calculate the low energy thresholds. To investigate whether the expected sensitivity is limited by radioactive background, we also perform Monte Carlo simulations of internal background from γ-rays.

We return to more theoretical questions in chapter 6, investigating different models for dark matter to see how the signatures in direct detection experiments may change. Our goal is to present a systematic analysis of all possible interactions between fermionic dark matter and quarks and calculate the resulting cross sections for non-relativistic scattering of dark matter on nuclei. Such an analysis will allow to develop a general understanding of whether the results from different direct detection experiments are in conflict or not.

Finally, a summary and our conclusions, as well as suggestions for further work, will be given in chapter 7. In the appendices, we summarize the notation and conventions used in this thesis and provide additional details on the calculations and the Monte Carlo simulations.

A comment on units

Given that this thesis comprises both theoretical and experimental approaches to dark matter detection, we have to deal with the different systems of units in the two fields. For the microscopic descriptions of particle interactions, we use natural units, setting $c = \hbar = k_B = 1$. For example, we use eV for both masses and energies. Nevertheless, we prefer to give distances in m, using the conversion factor $\hbar c = 197\,\mathrm{MeV\,fm} = 1$. Note that, for simplicity, we refrain from using atomic units in chapter 4. Consequently, the Bohr radius is $a_0 = 53\,\mathrm{pm}$, the Bohr velocity is $v_0 = \alpha = 1/137$ and the electron charge is given by $e^2 = \alpha\hbar c = 1.44\,\mathrm{MeV\,fm}$.

For macroscopic quantities, as they appear in the context of liquid xenon detectors (for example the fiducial mass, the detector dimensions or the runtime of an experiment), we use SI units. Also, it is conventional to use the unit km/s for astrophysical velocities, for instance the galactic escape velocity. We stick to this convention, but assume implicitly that these velocities are divided by $c_{\mathrm{SI}} = 3 \cdot 10^5\,\mathrm{km/s}$ when using them in the context of particle interactions.

CHAPTER 2

Detection of dark matter

In the previous chapter, we have presented substantial evidence that dark matter contributes significantly to the energy density of the universe. From such observations we can also infer some basic properties of dark matter, for example that it must be mostly non-baryonic. Nevertheless, many central questions concerning the particles that constitute dark matter, especially regarding their mass, their spin or their interactions with visible matter, cannot be answered this way.

To learn more about the nature of dark matter particles, we must find a way to actually detect them experimentally. For this purpose, many collaborations around the world have developed experimental strategies and built various kinds of detectors. There are three different experimental strategies for solving the dark matter puzzle: Direct detection experiments, indirect detection experiments and collider experiments. Most likely, only a combination of these strategies will allow to solve all problems related to dark matter.

Direct detection experiments attempt to observe dark matter particles as they pass through the Earth. Even though dark matter is expected to have only very scarce interactions, its density in the galactic halo of the Milky Way should be sufficiently large that scattering processes with nuclei do occur occasionally. The resulting nuclear recoils can be measured with dedicated low background detectors.

Indirect detection experiments aim to observe the products of dark matter annihilations, which occur in regions of high dark matter density — such as the center of the galaxy or the core of the sun. The annihilation products could include neutrinos, positrons, anti-protons and γ-rays, which would have a characteristic energy spectrum. These particles could then be observed with many ground-based and space-based telescopes.

Collider experiments, finally, attempt to actually produce dark matter by colliding Standard Model particles at high energies. The goal is to invert the annihilation process that occurs in the early universe, or to produce other new heavy particles that subsequently decay into the dark matter particle. However, since dark matter particles are long-lived and neutral, they will appear in the detectors only as missing momentum and energy, making an actual identification very difficult.

In this thesis, we will focus on direct detection experiments. We present the calculation of the direct detection event rate in section 2.1 and also discuss the astrophysical input and related uncertainties. In section 2.2, we will describe how to extract possible signals and give an overview of the existing direct detection experiments. Section 2.3 discusses some recent experimental results and the implications of these findings for future experiments. To conclude this chapter, we will discuss in section 2.4 in detail the XENON experiment, which will be the central topic for the rest of this thesis.

2.1 Direct detection of dark matter

As dark matter particles pass through the Earth, they will occasionally undergo elastic collisions with nuclei. Direct detection experiments attempt to measure the energy (called E_{nr}) that is transferred to the recoiling nucleus in such a scattering process. In this section, we want to calculate and discuss the probability distribution of nuclear recoil energies, or said differently, the energy spectrum that we expect to see in a detector for such scattering events.

2.1.1 Differential event rates

The central quantity relevant for the direct detection of dark matter is the *differential event rate* $\mathrm{d}R/\mathrm{d}E_{\mathrm{nr}}$. The unit of the differential event rate is the number of events per kg detector mass per day runtime per keV energy, which is often called differential rate unit (dru). One obtains the *total event rate R* (in events per kg per day) by integrating the differential event rate from the lower to the upper energy threshold of the detector. To obtain the total number of expected events, we must multiply the total event rate with the *exposure* of the experiment, which is the product of detector mass and runtime of the experiment. For more details on the calculation of event rates, we refer to appendix B.

We shall denote the mass of the dark matter particle with m_χ and the mass of the nuclei in the target with m_{N}. We furthermore introduce the reduced mass $\mu_{\mathrm{N}} = m_\chi m_{\mathrm{N}}/(m_\chi + m_{\mathrm{N}})$. Analogously, the quantities m_{p} and μ_{p} refer to the mass and the reduced mass of a single proton. The number density of dark matter particles is equal to ρ_0/m_χ, where the local energy density of dark matter is given by $\rho_0 = (0.30 \pm 0.05)\,\mathrm{GeV\,cm^{-3}}$ [10]. To obtain the dark matter flux, we must multiply the number density with the dark matter velocity v. This velocity, however, is not the same for all dark matter particles. Instead, we have a distribution of velocities described by a function $f(v)$, which we will discuss in section 2.1.2.

The differential event rate is given by the product of the dark matter flux, the density of target nuclei and the differential interaction cross section, integrated over

all contributing dark matter velocities:

$$\frac{\mathrm{d}R}{\mathrm{d}E_{\mathrm{nr}}} = \frac{\rho_0}{m_{\mathrm{N}} m_\chi} \int\limits_{v_{\mathrm{min}}}^{\infty} v f(v) \frac{\mathrm{d}\sigma}{\mathrm{d}E_{\mathrm{nr}}}(v, E_{\mathrm{nr}})\, \mathrm{d}v \; . \tag{2.1}$$

To determine, which velocities can contribute to a given nuclear recoil energy, we must look at the kinematics of the collision between dark matter particle and nucleus. Since all velocities are non-relativistic, we can easily express the nuclear recoil energy in terms of the dark matter velocity and the scattering angle θ in the center-of-mass frame

$$E_{\mathrm{nr}} = \mu_{\mathrm{N}}^2 v^2 (1 - \cos\theta)/m_{\mathrm{N}} \; . \tag{2.2}$$

Consequently, to obtain a recoil energy of E_{nr}, the dark matter velocity must at least be

$$v_{\mathrm{min}} = \sqrt{\frac{m_{\mathrm{N}} E_{\mathrm{nr}}}{2\mu_{\mathrm{N}}^2}} \; . \tag{2.3}$$

2.1.2 The dark matter velocity distribution

In the standard halo model, the distribution of dark matter velocities is described by an isotropic Gaussian distribution

$$\tilde{f}(v)\, \mathrm{d}^3 v = \frac{1}{(\pi v_{\mathrm{c}}^2)^{3/2}} \exp\left(-\frac{v^2}{v_{\mathrm{c}}^2}\right) \mathrm{d}^3 v \; , \tag{2.4}$$

where $v_{\mathrm{c}} = (220 \pm 20)\,\mathrm{km\,s^{-1}}$ is the *local circular velocity*. Strictly speaking, the velocity that appears in equation (2.4) is the velocity in the Galactic rest frame. Since we are interested in the distribution of velocities relative to the Earth, we must replace $\boldsymbol{v}$ by $\boldsymbol{v} + \boldsymbol{v}_{\mathrm{E}}$, where the motion of the Earth is given by [11]

$$v_{\mathrm{E}} = |\boldsymbol{v}_{\mathrm{E}}| = v_{\mathrm{c}} \left[1.05 + 0.07 \cos\left(\frac{2\pi(t - t_{\mathrm{p}})}{1\,\mathrm{yr}}\right)\right] \; , \tag{2.5}$$

with $t_{\mathrm{p}} = \mathrm{June\,2nd} \pm 1.3\,\mathrm{days}$ (for more details, see [12]). Consequently, we get

$$\begin{aligned}
\int \tilde{f}(v)\, \mathrm{d}^3 v &= \int \frac{1}{(\pi v_{\mathrm{c}}^2)^{3/2}} \exp\left(-\frac{|\boldsymbol{v} + \boldsymbol{v}_{\mathrm{E}}|^2}{v_{\mathrm{c}}^2}\right) \mathrm{d}^3 v \\
&= \int \frac{v}{\sqrt{\pi} v_{\mathrm{c}} v_{\mathrm{E}}} \left[\exp\left(-\frac{(v - v_{\mathrm{E}})}{v_{\mathrm{c}}^2}\right) - \exp\left(-\frac{(v + v_{\mathrm{E}})}{v_{\mathrm{c}}^2}\right)\right] \mathrm{d}v \qquad (2.6) \\
&\equiv \int f(v)\, \mathrm{d}v \; .
\end{aligned}$$

Another correction to the velocity distribution comes from the fact that no dark matter particles with a velocity above the *galactic escape velocity* $v_{\text{esc}} = (544\pm50)\,\text{km}\,\text{s}^{-1}$ can be bound in the galactic halo. Consequently we must modify equation (2.6) in such a way that $f(v) = 0$ for $v > v_{\text{esc}}$ [13]:

$$f(v)\,\mathrm{d}v = \frac{1}{k}\left[\exp\left(-\frac{(v-v_{\text{E}})}{v_{\text{c}}^2}\right) - \exp\left(-\frac{(v+v_{\text{E}})}{v_{\text{c}}^2}\right)\right]\Theta\left(v_{\text{esc}} - |\boldsymbol{v}+\boldsymbol{v}_{\text{E}}|\right)\,\mathrm{d}v\;,\quad(2.7)$$

where

$$k = (\pi v_{\text{c}})^{3/2}\left[\mathrm{Erf}\left(\frac{v_{\text{esc}}}{v_{\text{c}}}\right) - \frac{2}{\sqrt{\pi}}v_{\text{esc}}v_{\text{c}}\exp\left(-\frac{v_{\text{esc}}^2}{v_{\text{c}}^2}\right)\right]\qquad(2.8)$$

ensures that $\int_0^\infty f(v)\,\mathrm{d}v = 1$.

2.1.3 Cross sections

The differential cross section $\mathrm{d}\sigma/\mathrm{d}E_{\text{nr}}$ in equation (2.1) contains the input from particle physics to the differential event rate. It depends fundamentally on the interaction between dark matter and quarks, which result from the underlying particle physics model. We will discuss in chapter 6 how to calculate the cross section for a large number of models. In this section, we will only state the results that are necessary for us to calculate the differential event rate. It turns out that we can distinguish between interactions that are independent of the nuclear spin (so-called *SI interactions*) and interactions that depend on it (so-called *SD interactions*). In this chapter, as well as for chapters 3 to 5, we will only consider SI interactions.

In this case, we can separate the energy and velocity dependence of the cross section by writing

$$\left(\frac{\mathrm{d}\sigma}{\mathrm{d}E_{\text{nr}}}\right)_{\text{SI}} = \frac{m_{\text{N}}\sigma_0 F^2(E_{\text{nr}})}{2\mu_{\text{N}}^2 v^2}\;.\qquad(2.9)$$

Here, $F^2(E_{\text{nr}})$ is the *nuclear form factor*, which reflects the loss of coherence with increasing momentum transfer. It corresponds essentially to the Fourier transform of the nucleon density. One usually assumes the parameterization

$$F^2(q) = \left(\frac{3j_1(qR_1)}{qR_1}\right)^2 \exp\left(-q^2 s^2\right)\;,\qquad(2.10)$$

where $q = \sqrt{2m_{\text{N}}E_{\text{nr}}}$ is the momentum transfer and j_1 is a spherical Bessel function. The parameters s and R_1 describe the size and the form of the nucleus. They are usually taken to be $s \approx 1\,\text{fm}$ and $R_1 = \sqrt{R^2 - 5s^2}$ with $R \approx 1.2\,\text{fm}\sqrt{A}$, where A is the mass number of the target nucleus.

In the most simple cases, the fundamental cross section σ_0 does not depend on the momentum transfer and the velocity. It depends only on the couplings of dark matter to protons and neutrons, called f_p and f_N, respectively. We can write [14]

$$\sigma_0 = \frac{[Zf_\mathrm{p} + (A - Z)f_\mathrm{N}]^2}{f_\mathrm{p}^2} \frac{\mu_\mathrm{N}^2}{\mu_\mathrm{p}^2} \sigma_\mathrm{p}^\mathrm{SI} \,, \tag{2.11}$$

where Z is the atomic number of the target nucleus and $\sigma_\mathrm{p}^\mathrm{SI}$ is the dark matter proton cross section. f_p and f_N can in principle be calculated from quark couplings to dark matter and the quark content of the nucleons. However, for most cases, one obtains $f_\mathrm{p} \approx f_\mathrm{N}$, so that equation (2.11) simplifies to

$$\sigma_0 = A^2 \frac{\mu_\mathrm{N}^2}{\mu_\mathrm{p}^2} \sigma_\mathrm{p}^\mathrm{SI} \,. \tag{2.12}$$

2.1.4 Dark matter spectra

Substituting equation (2.12) and equation (2.9) into equation (2.1), we get

$$\frac{\mathrm{d}R}{\mathrm{d}E_\mathrm{nr}} = \frac{\rho_0 A^2}{2\mu_\mathrm{p}^2 m_\chi} \sigma_\mathrm{p}^\mathrm{SI} F^2(E_\mathrm{nr}) \int_{v_\mathrm{min}}^{\infty} \frac{f(v)}{v} \, \mathrm{d}v \,. \tag{2.13}$$

With $f(v)$ from equation (2.7), the integral can be performed analytically (see for instance [15]) to give a function $g(v_\mathrm{min})$. Figure 2.1 shows some typical differential event rates. We make the following observations:

- The differential event rate decreases exponentially with increasing recoil energy. This decrease is partly due to a decreasing nuclear form factor $F(E_\mathrm{nr})$, reflecting the loss of coherence, and partly due to a decreasing velocity integral $g(v_\mathrm{min})$ reflecting the smaller number of dark matter particles that have a sufficiently large velocity to contribute.

- The differential event rate is proportional to A^2, so that scattering at low recoil energies is strongly enhanced for targets with high mass number. At the same time, the differential event rate falls more steeply for heavier targets, because the nuclear form factor $F(E_\mathrm{nr})$ decreases more quickly.

- Similarly, for lower dark matter mass, the differential event rates will be larger at low recoil energy because of the overall factor m_χ^{-1} and smaller at high recoil energy, because v_min grows more quickly if m_χ is small.

In fact, for $m_\chi \ll m_\mathrm{N}$ we have $\mu_\mathrm{N} \approx m_\chi$ and thus $v_\mathrm{min} = \sqrt{m_\mathrm{N} E_\mathrm{nr}/2m_\chi^2}$. Since we have $g(v_\mathrm{min}) = 0$ for $v_\mathrm{min} > v_\mathrm{esc} + v_\mathrm{E}$, the velocity cutoff at v_esc implies an energy

(a) A xenon target with $m_N = 131.3$ u.

(b) A germanium target with $m_N = 72.6$ u.
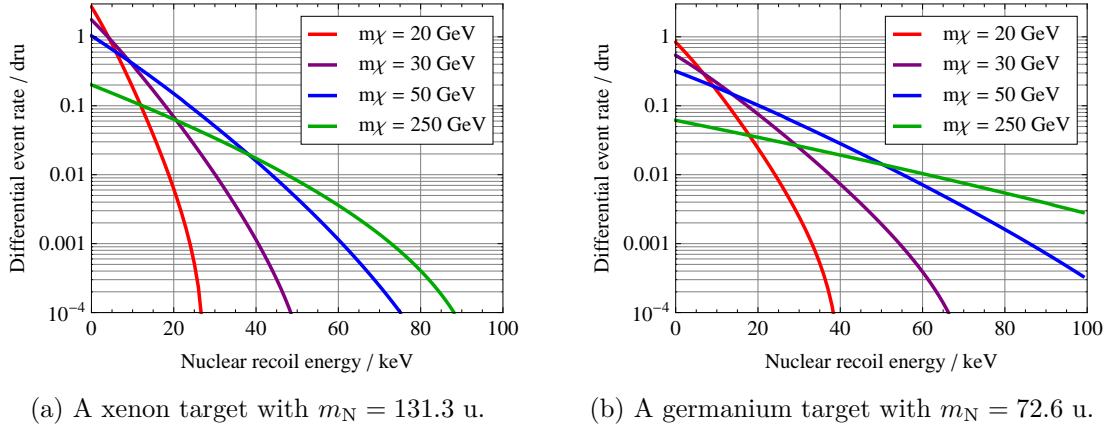
Figure 2.1: Differential event rate for various dark matter masses and different target materials. In each case, we have set $\sigma_p^{SI} = 10^{-41}\,\mathrm{cm}^2$, which is rather large for dark matter.

cutoff for the differential event rate. For $m_\chi \ll m_N$, we obtain

$$\frac{\mathrm{d}R}{\mathrm{d}E_{nr}} = 0 \ \ \text{for} \ \ E_{nr} > \frac{2m_\chi^2 (v_{esc} + v_E)^2}{m_N} \ . \tag{2.14}$$

This bound becomes stronger as the dark matter mass decreases, so that all events occur at very low recoil energy. This fact makes the experimental observation of low mass dark matter very difficult (see chapter 3).

2.1.5 Astrophysical uncertainties

To conclude this section, we would like to point out that large uncertainties are present in the differential event rates shown in figure 2.1. All astrophysical input, meaning the dark matter density ρ_0, the circular velocity v_c and the escape velocity v_{esc} are known with 10% accuracy at best. Moreover, the velocity distribution might not be purely Gaussian. These uncertainties persist in all conclusions drawn from direct detection experiments. To be able to compare results from different experiments, it is generally agreed to use the above values for the astrophysical quantities. Nevertheless, the conclusions drawn from such a comparison (for example whether different experiments are compatible or not) may still depend on these choices. For a discussion of related problems, see [15, 16].

2.2 Direct detection experiments

We now turn to the discussion of experimental strategies for the direct detection of dark matter. First of all, note that the differential event rates are extremely small. For a dark matter particle with $\sigma_{\mathrm{p}}^{\mathrm{SI}} < 10^{-42}\,\mathrm{cm}^2$ we expect less than one event per day per kg for common target materials. Consequently, one needs experiments with an extremely low background in order to be able to observe a dark matter signal at all. Nevertheless, the differential event rate in equation (2.13) has three characteristic features that offer the possibility to identify dark matter experimentally: *energy dependence*, *material dependence* and the *time dependence* of v_{E}.

The most obvious feature of the differential event rate is the exponential suppression with higher recoil energy. To observe this characteristic spectrum, we must have a detector that can accurately measure the nuclear recoil energy down to a threshold of only a few keV. Doing so with detectors of different target materials would also allow to identify the second important signature, namely that the event rate is proportional to A^2 (the so-called material dependence).

Many different collaborations worldwide follow this approach. The most challenging task for each experiment is to reject background from particles that scatter elastically with electrons. The presently strongest constraints for the proton cross section $\sigma_{\mathrm{p}}^{\mathrm{SI}}$ come from CDMS-II [17] and XENON10 [18]. CDMS-II uses germanium and silicon detectors cooled to less than $50\,\mathrm{mK}$, while XENON10 employs a liquid xenon dual-phase time projection chamber. While both experiments have not seen a conclusive dark matter signal, the CoGeNT collaboration, also using a germanium detector, has recently presented some noteworthy results, which may indicate the observation of dark matter [19]. We will discuss these results in more detail in section 2.3.

Furthermore, KIMS [20], using a CsI(Tl) target, COUPP [21], using CF_3I, and PICASSO [22], using a C_4F_{10} target, give the best bounds on spin-dependent interactions. The experiments ZEPLIN-III [23], using a liquid xenon target, and CRESST-II [24], employing $CaWO_4$, strongly constrain inelastic dark matter [25]. Since we will not go into more detail on these models for the moment, we shall not discuss these experiments further and refer to [14] for a detailed analysis.[1]

A very different approach to direct detection of dark matter comes from noting that the differential event rate is time-dependent, because $f(v)$ depends on $v_{\mathrm{E}}(t)$ — see equation (2.5). Consequently, both the energy spectrum and the total event rate are expected to vary over the course of the year. One can try to search experimentally for such a modulation of the signal. The advantage of this method is that background rejection is less important, because a *constant* background should not spoil the modulation.

This approach has been pursued by the DAMA collaboration with the experiments

---

[1]Note that we have not mentioned experiments that are currently running or close to completion and are expected to give competitive results in the near future. Also, we have neglected experiments that have been competitive in the past but are no more.

DAMA/NaI and DAMA/LIBRA [26], both using NaI(Tl) scintillators. In fact, the collaboration observes clear evidence for an annual modulation of the signal. The origin of this modulation, however, is unclear. The interpretation of these results will be the topic of the following section.

2.3 Evidence for dark matter?

As we have mentioned in the previous section, two collaborations claim to have observed a dark matter signal: CoGeNT and DAMA. The CoGeNT collaboration observes a large number of events close to the low energy threshold of their detector, which is the lowest threshold achieved by any dark matter experiment. Although the observed spectrum is compatible with an exponentially falling background, it has not been possible to identify a source for such a background. Consequently, one may treat the signal as originating from dark matter. Because of the steep decrease of the observed signal, the corresponding dark matter particle would have to be light, meaning $m_\chi \approx 10\,\mathrm{GeV}$.

The DAMA collaboration observes an annual modulation of their signal with 8.2σ significance. Moreover, the measured phase agrees with the phase expected from the motion of the Earth around the sun. Although many suggestions have been made concerning the possible origins of such modulations and the presented evidence has not been able to convince all critics, it is tempting to interpret this modulation signal as an observation of dark matter. Since the modulation is observed only at low recoil energies, the data again points towards a dark matter particle with low mass.

Nevertheless, with standard assumptions, the results from CoGeNT and DAMA are not compatible with each other, because they favor different parameter regions. What is worse, the results are also in conflict with the data presented by CDMS and XENON. If either of the signals observed by CoGeNT or DAMA were due to standard SI interaction of dark matter, both CDMS and XENON should most likely have observed a signal. The parameter regions favored by CoGeNT and DAMA and the regions excluded by CDMS and XENON are shown in figure 2.2.

It turns out that, there is a marginal compatibility between CoGeNT and the combined data from CDMS and XENON, while a naive interpretation of the DAMA signal in terms of SI interactions of dark matter is ruled out. Of course, one could think of more complicated models or try to vary the astrophysical input in order to reduce this tension. Also, a different interpretation of the experimental data might improve the compatibility (see for example the ongoing discussion on channeling in DAMA [27]). For an exhaustive discussion of these questions, we refer to [28].

In this thesis, we do not want to take a position on the question whether the signals observed by CoGeNT and DAMA are due to dark matter or not. The point we wish to make is that it is desirable to be able to check the parameter region preferred by CoGeNT and DAMA with a higher statistical significance in order to
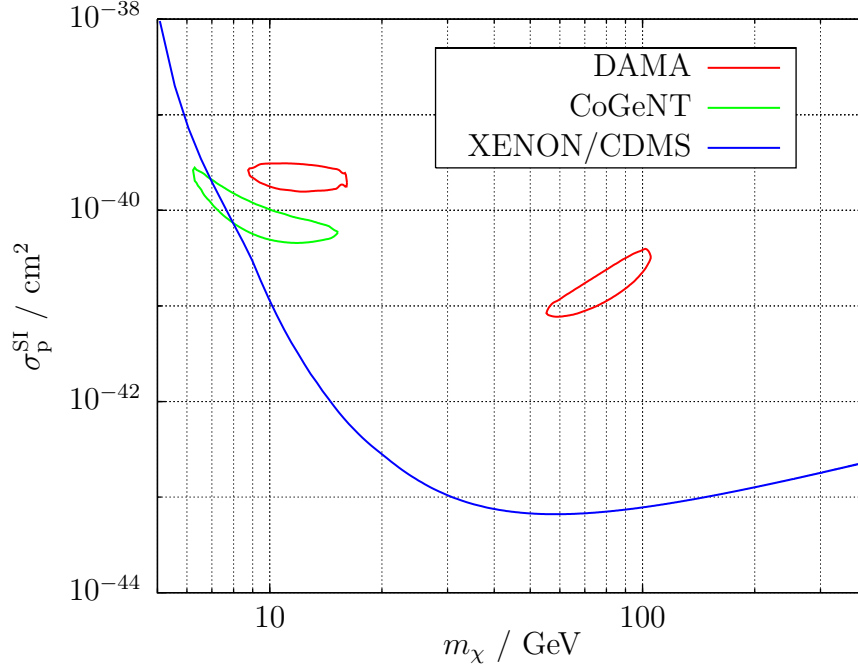
Figure 2.2: The parameter regions favored at 3σ confidence by DAMA and CoGeNT. The region above the blue line is excluded by the combined results from XENON and CDMS with 3σ significance. One observes a marginal compatibility with CoGeNT, while the DAMA results are excluded. For details on how to calculate exclusion limits, we refer to appendix B.

confirm or rule out the dark matter hypothesis. We believe that the most promising detector for this purpose is XENON100, followed possibly by even larger liquid xenon detectors. For this reason, we will now turn to a detailed description of the liquid xenon technology and the design of the XENON100 detector. The following chapters will then be devoted to an analysis of the sensitivity of such detectors for low mass dark matter.

2.4 The XENON100 experiment

XENON100 is an ultra-low background detector, filled with 161 kg of extremely pure liquid xenon, currently taking data at the Gran Sasso Underground Laboratory in Italy. While being conceptually very similar to XENON10, the new detector employs a much larger detector mass. In this section, we will discuss the detector's principle of operation and introduce the terminology relevant for the rest of this thesis. A more detailed description of the liquid xenon technology can be found in [3, 29].

There are several reasons why liquid xenon is extremely useful for the direct
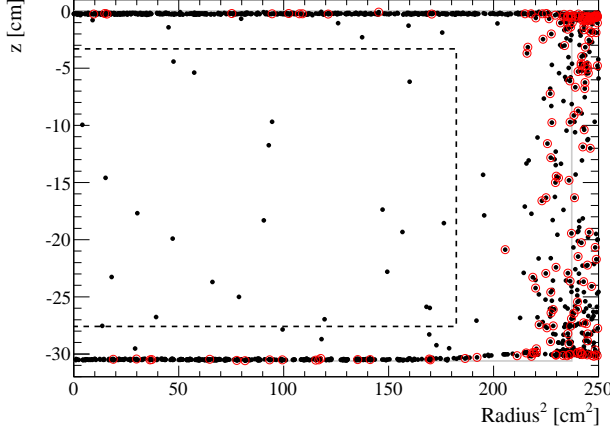
Figure 2.3: A typical distribution of background events in the liquid xenon sensitive volume. Events that are identified as nuclear recoils are marked with a red circle. The dashed line indicates the 40 kg fiducial volume. Figure taken from [30].
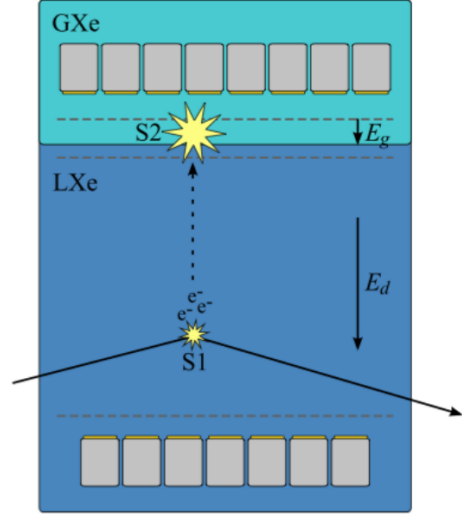
Figure 2.4: A typical scattering event in a liquid xenon detector. E_d and E_g denote the electric fields used to drift the electrons and extract them into the gas phase, respectively. Figure courtesy of the XENON Collaboration.

detection of dark matter. First of all, it is an excellent scintillator and offers a high ionization yield as response to energy deposition. In fact, liquid xenon has the highest scintillation and ionization yield of all liquid noble gases and moreover does not require wave-length shifters. One can detect both light and charge simultaneously to give very good background rejection (see below). Moreover, liquid xenon is comparably inexpensive, so the detector can easily be scaled to larger masses. Finally, because of its large atomic mass ($Z = 54$, $A = 131.3$), liquid xenon benefits from the factor A^2 that appears in the differential event rate for dark matter and also has a strong self-shielding, meaning a high stopping power for γ-rays.

The most important property of dark matter detectors is an efficient rejection of background. Because of the strong self-shielding of liquid xenon, most background events occur close to the surface of the sensitive volume (see figure 2.3). If we are able to reconstruct the position of each primary event in three dimensions, we can reduce the background by employing a *fiducial volume cut*. For this reason, the XENON100 detector is a dual-phase time projection chamber (TPC) that is monitored by two arrays of photomultiplier tubes (PMTs).

An interaction in the sensitive liquid xenon (LXe) volume leads to two distinct signals. The first signal, called $S1$, results from the *primary scintillation* of liquid xenon at the position of the interaction. To measure the ionization signal as well,

one applies a high voltage electric field that extracts the electrons into the gas phase. In the gaseous xenon (GXe) the charge cloud then produces a *secondary scintillation signal*, called $S2$, via the proportional scintillation mechanism (see figure 2.4). The z-position[1] of the primary event can be inferred from the delay of the $S2$ signal due to the drift velocity of the electrons, while the x- and y-position can be reconstructed from the PMT hit pattern of the $S2$ signal.

The $S1$ signal, on the other hand, is used for the reconstruction of the primary recoil energy. For scattering events that produce a recoiling electron (such as Compton scattering of γ-rays), the electron recoil energy is given by

$$E_{\mathrm{er}} = \frac{S1}{L_{\mathrm{y}} \cdot S_{\mathrm{ee}}} \ . \tag{2.15}$$

Here $S1$ is given in photoelectrons (phe) and L_{y} is the light yield of the detector, obtained from calibration with γ-rays. S_{ee} is a quenching factor that reflects the suppression of scintillation light in the presence of an electric field. For XENON100, it is $S_{\mathrm{ee}} = 0.58$ [30]. Note that L_{y} itself depends on E_{er}, so equation (2.15) can only be solved numerically. For example, $L_{\mathrm{y}} = 2.2\,\mathrm{phe/keV}$ for $E_{\mathrm{er}} = 122\,\mathrm{keV}$ (corresponding to the energy of γ-rays from the decay of $^{57}\mathrm{Co}$).

For nuclear recoils (from neutron scattering or, in fact, dark matter interactions), the reconstruction of the energy scale is more involved. The reason is that in this case scintillation light is strongly suppressed due to nuclear quenching (see chapter 4). One usually defines the so-called *relative scintillation efficiency*, $\mathcal{L}_{\mathrm{eff}}$, as the ratio of the scintillation yield for nuclear recoils and the scintillation yield for electron recoils with an energy of $122\,\mathrm{keV}$ at zero electric field. We can then write

$$E_{\mathrm{nr}} = \frac{S1}{\mathcal{L}_{\mathrm{eff}} \cdot L_{\mathrm{y}}} \frac{S_{\mathrm{ee}}}{S_{\mathrm{nr}}} \ , \tag{2.16}$$

where $S_{\mathrm{nr}} = 0.95$ is the quenching factor for nuclear recoils in an electric field [29]. The relative scintillation efficiency $\mathcal{L}_{\mathrm{eff}}$ is energy dependent, but unfortunately not very well known. We show different measurements of $\mathcal{L}_{\mathrm{eff}}$ as well as a global fit in figure 2.5. Unless stated otherwise, we shall from now on use the lower 90% confidence contour (referred to as the conservative choice) for $\mathcal{L}_{\mathrm{eff}}$. In chapter 4, however, we will also develop a theoretical model to predict $\mathcal{L}_{\mathrm{eff}}$.

One must keep in mind that both E_{er} and E_{nr} are *reconstructed energies*. Not only do they depend on our assumptions for the light yield and the quenching factors, but they are also affected by the energy resolution of the detector. Moreover, the reconstruction will be completely wrong if we misidentify an electron recoil as a nuclear recoil or vice versa. Consequently, reconstructed energies are no more than the best guess for the actual recoil energy. To emphasize this fact, we will denote

---

[1]The z-axis is by convention the symmetry axis of the TPC.
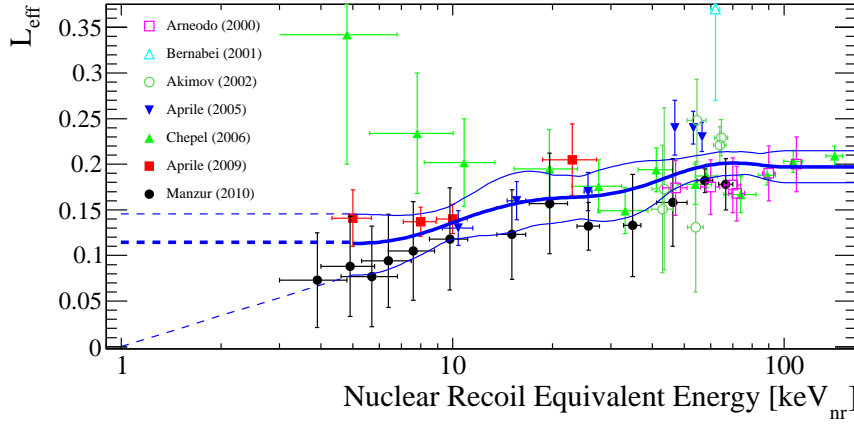
Figure 2.5: Experimental data for the relative scintillation efficiency $\mathcal{L}_{\mathrm{eff}}$. The thick blue line indicates the global fit, while the thin blue lines indicate the upper and lower 90% confidence contour. Dashed lines indicate possible extrapolations for $E_{\mathrm{nr}} < 4\,\mathrm{keV}$, where no measurements are available. Figure taken from [30].

reconstructed energies with keVee for electron recoils and keVnr for nuclear recoils, while reserving the unit keV for true physical recoil energies.

We have already mentioned the fiducial volume cut that is used to drastically reduce the background level. However, to achieve yet a stronger background rejection, the XENON100 detector employs several additional techniques. First of all, there is an active veto, composed of an additional layer of liquid xenon, which is optically separated from the sensitive volume and monitored by additional PMTs. This veto allows to effectively reduce background from external sources such as cosmic ray muons.

What remains as the dominant contribution to the background are radioactive contaminations of the detector materials as well as intrinsic background (see chapter 5.4). Since γ-rays scatter mostly off electrons, while dark matter almost exclusively interacts with nuclei, we must find a way to distinguish electron recoils and nuclear recoils. For liquid xenon detectors this distinction is made by comparing the magnitude of the $S1$ and the $S2$ signal. Calibration data from γ-ray and neutron sources shows that the ratio $S2/S1$ is much larger for electron recoils than it is for nuclear recoils (see figure 2.6).[1] Consequently, we can effectively reject background from electron scattering by requiring that $\log_{10}(S2/S1) < f(S1)$, where the function $f(S1)$ is referred to as the *nuclear recoil cut*. This cut will be the topic of chapter 3.3.2.

Background from neutron scattering, finally, can be reduced by applying a *single scatter cut*. Neutrons are likely to scatter more than once inside the sensitive volume,

---

[1]This surprising observation is believed to be due to the different track structure for nuclear recoils, leading to different recombination rates.
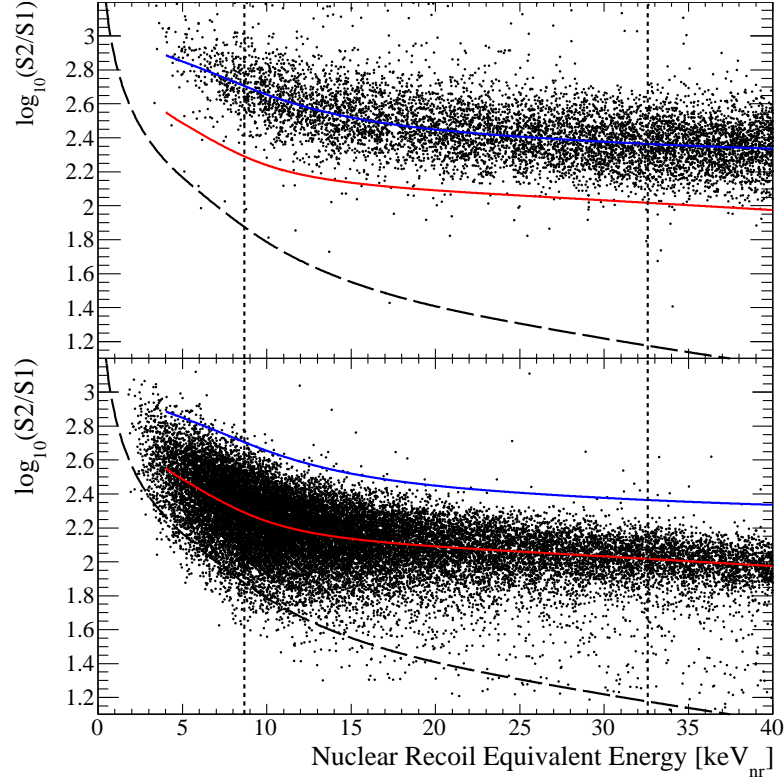
Figure 2.6: Electronic (top) and nuclear (bottom) recoil bands. The data points are from ^{60}Co and AmBe calibration, respectively. For the x-axis, the $S1$ signal has been converted to nuclear recoil energy, using equation (2.16). The blue and red lines correspond to the median of the electronic and nuclear recoil band, respectively. The vertical dashed lines indicate the $S1$ search window $4\,\mathrm{phe} \leq S1 \leq 20\,\mathrm{phe}$, while the long dashed line shows the $S2$ threshold $S2 > 300\,\mathrm{phe}$. Figure taken from [30].

while dark matter particles will never have more than one interaction. Thus, we can effectively reject neutrons by requiring that we observe only one $S2$ signal above a given threshold. We will discuss this cut again in chapters 3.3.1 and 5.4.

Unless the XENON100 detector actually observes a significant number of nuclear recoil events in the search region $4 \leq S1 \leq 20$, it will strongly improve the exclusion limits for SI interactions. In fact, at $m_\chi \approx 50\,\mathrm{GeV}$, XENON100 will be sensitive to cross sections as low as $\sigma_\mathrm{p}^\mathrm{SI} \approx 2 \cdot 10^{-45}\,\mathrm{cm}^2$. The sensitivity of the experiment for $m_\chi \leq 10\,\mathrm{GeV}$, however, is highly controversial (see for example [31]). It depends on many factors such as the detector resolution, the cut acceptance and the effective scintillation yield. In the following chapters, we will examine each of these problems and demonstrate that liquid xenon detectors are indeed capable of checking the parameter region preferred by CoGeNT and DAMA.

Detector performance at low energies

In the following two chapters we will discuss the performance of liquid xenon detectors for low energy nuclear recoils, meaning $E_{\mathrm{nr}} \approx 1 - 10\,\mathrm{keV}$. For any dark matter direct detection experiment a high sensitivity at these energies is very important. The reason is that the dark matter spectrum decreases exponentially with increasing recoil energy, so the expected total event rate in a detector will increase significantly if the low energy sensitivity can be improved. If the dark matter particle is heavy, the recoil spectrum decreases only slowly with energy (see figure 2.1), so a lower acceptance can still be compensated by a larger exposure. For light dark matter, however, all events occur at very low recoil energies, so an insufficient sensitivity in this region will render the detector essentially blind for such particles.

As we have mentioned in chapter 2, there have recently been some experimental indications that dark matter might be lighter than generally expected, possibly of order $10\,\mathrm{GeV}$. Clearly, one would like to probe this parameter region with liquid xenon detectors in order to confirm or exclude these observations. However, to illustrate the difficulty related to this task, we can make a simple estimate of the maximum recoil energy that such a light dark matter particle would deposit in the detector. Using equation (2.14) and substituting $m_\chi = 10\,\mathrm{GeV}$, we get $E_{\mathrm{nr}}^{\mathrm{max}} \approx 11\,\mathrm{keV}$.

The XENON100 experiment employs a threshold of $S1 \geq 4\,\mathrm{phe}$, corresponding to an energy threshold of roughly $10\,\mathrm{keVnr}$ (see figure 2.6). From the calculation above, we would naively draw the conclusion that the XENON100 experiment — and all upcoming liquid xenon experiments with a similar threshold — are almost completely insensitive to dark matter particles with $m_\chi < 10\,\mathrm{GeV}$. Fortunately, we have neglected a very important property of liquid xenon detectors: the detector resolution. At recoil energies where only few photoelectrons are observed, we must expect large relative fluctuations in the $S1$ signal. Because of such fluctuations, a nuclear recoil that would on average produce only two or three photoelectrons has a significant probability to pass the $S1 \geq 4\,\mathrm{phe}$ threshold. The detector resolution is consequently very important for the low energy sensitivity of liquid xenon detectors.

Clearly, to calculate exclusion bounds from the XENON experiment, we need to quantify the probability distribution of $S1$ signals for a given recoil energy. We will

discuss the relevant statistics and propose a model to describe these fluctuations in section 3.1, also discussing the fluctuations of the $S2$ signal. In section 3.2 we will propose a method to test this model using Monte Carlo simulations of the nuclear recoil band. From such simulations, we can also learn a lot about the acceptance of the detector at low energies. Consequently, we will discuss the different cuts used in the XENON100 experiment and try to estimate their acceptance in section 3.3. Finally, we will put all the pieces together and present an novel framework to calculate exclusion limits in section 3.4. In this context we will also discuss, how inhomogeneities inside the detector can further increase fluctuations.

To avoid confusion, note that we are not concerned with possible improvements of the detector sensitivity in this chapter — our purpose is to determine the sensitivity for a given detector. Although our discussion can be applied to a large variety of detectors, we will use the properties of the XENON100 detector for concreteness. A discussion of ways to improve the low energy sensitivity in future liquid xenon detectors will be left for chapter 5.

3.1 Detector resolution

3.1.1 $S1$ fluctuations

Writing down equation (2.16), we have pretended that there is a one-to-one relation between nuclear recoil energies and the produced number of $S1$ photoelectrons. The finite detector resolution, however, leads to fluctuations in the number of photoelectrons even for a fixed recoil energy. Consequently, $S1$ cannot be expressed simply as a function of the nuclear recoil energy, but rather as a probability distribution with an expectation value μ_{S1} that depends on E_{nr}:

$$p(S1 = n_1) = p_1(n_1, \mu_{\mathrm{S1}}(E_{\mathrm{nr}})) \,. \tag{3.1}$$

It should be clear from the discussion above, that in order to determine the sensitivity of a liquid xenon detector for low energy nuclear recoils, we need to know the probability distribution $p_1(n_1, \mu_{\mathrm{S1}}(E_{\mathrm{nr}}))$. To determine p_1, we need to look carefully at the detection process of scintillation light.

The idea is that the number of photons produced initially is much larger than the number of photoelectrons actually detected. For a nuclear recoil energy of $10\,\mathrm{keV}$ we expect roughly 60 photons to be produced at the position of the scattering event (see chapter 4), but only about 4 photoelectrons will be detected.

This strong reduction comes mostly from the *light collection efficiency* of the detector and the *quantum efficiency* of the PMTs. For XENON100, the light collection efficiency is $LCE \approx 0.25$ meaning that only one out of four photons

produced initially will actually hit a PMT.[1] The PMTs used in XENON100, on the other hand, have a quantum efficiency of $QE \approx 0.25$, meaning that only one out of four photons that hit a PMT actually produce a photoelectron. Consequently, the probability that a photon produces a photoelectron is only about 6%. This probability applies independently to each photon, so the production of photoelectrons essentially corresponds to a Bernoulli trial.

From these considerations, we expect the number of photoelectrons to follow Binomial statistics, meaning that

$$p_1(n_1, \mu_{S1}(E_{nr})) = \binom{N_{ph}}{n_1} p^{n_1} (1-p)^{N_{ph}-n_1} \ , \tag{3.2}$$

where N_{ph} is the number of photons produced initially and $p = QE \cdot LCE$ is the probability to produce a photoelectron. Note that N_{ph} depends on μ_{S1}, because we require that $p \cdot N_{ph} = \mu_{S1}(E_{nr})$.[2] For small p and large N_{ph} the Binomial distribution can be well approximated by the Poisson distribution, which is much more convenient for actual calculations:

$$p_1(n_1, \mu_{S1}(E_{nr})) = \frac{\mu_{S1}(E_{nr})^{n_1} \, e^{-\mu_{S1}(E_{nr})}}{n_1!} \ . \tag{3.3}$$

In the derivation of p_1, we have not considered the production process of scintillation photons. Nevertheless, for very small numbers of photoelectrons, the detection process gives the dominant contribution to fluctuations, details of the production process turn out to be subdominant. Thus, we will assume in the following, that $S1$ fluctuations can be well described by a Poisson distribution. We will consider in detail subdominant contributions to $S1$ fluctuations in section 3.4 and show that even the tails of the $S1$ distribution are well described by Poisson statistics. In addition, we show in section 3.2 that our assumption reproduces the shape of the nuclear recoil band with good agreement.

3.1.2 *S2* fluctuations

Having discussed the statistics that describe fluctuations of the $S1$ signal, we now turn to the analogous discussion for the $S2$ signal. In general, the $S2$ signal is much larger than the $S1$ signal, because every electron extracted into the gas phase produces about 20 photoelectrons. Consequently, the $S2$ signal does not limit the sensitivity of liquid xenon detectors in the low energy region. Nevertheless, we will need a proper description of $S2$ fluctuations for a simulation of the nuclear recoil

---

[1]We will discuss the light collection efficiency in more detail in section 3.4 and chapter 5.

[2]The value obtained for N_{ph} will not necessarily be an integer. However, as $N_{ph} \gg 1$, rounding should not give a large error.

band, as we shall see in section 3.2.

We will assume that $S1$ and $S2$ fluctuations are uncorrelated. This assumption does not hold strictly, because one observes experimentally an anticorrelation of the two signals. The explanation is that the number of electron-ion pairs that recombine to produce a scintillation photon changes from event to event. However, while the anticorrelation of the two signals is large for electron recoils, it is observed to be much smaller for nuclear recoils, because a large fraction of the scintillation light does not originate from recombination but from direct excitations (see chapter 4.3).

In contrast to the $S1$ signal, the $S2$ signal is amplified, meaning that the number of produced photoelectrons n is much larger than the number of initially produced electrons N_{q}. Consequently, the fluctuations in the production process, which we could neglect for the $S1$ signal, will dominate the distribution of $S2$ signals. Unfortunately, while we understand the detection process quite well, the distribution describing the production of electrons is not very well known.

The most reasonable assumption is that the fluctuations of N_{q} can again be described by Poisson statistics:

$$p_{\mathrm{q}}(N_{\mathrm{q}}, \mu_{\mathrm{q}}(E_{\mathrm{nr}})) = \frac{\mu_{\mathrm{q}}(E_{\mathrm{nr}})^{N_{\mathrm{q}}} \, \mathrm{e}^{-\mu_{\mathrm{q}}(E_{\mathrm{nr}})}}{N_{\mathrm{q}}!} \; , \tag{3.4}$$

where $\mu_{\mathrm{q}}(E_{\mathrm{nr}})$ is determined from measurements of the ionization yield of liquid xenon (see figure 3.2). If each electron produces r photoelectrons in the amplification process, the distribution of photoelectrons is then roughly a normal distribution with mean $\mu_{\mathrm{S2}} = r\mu_{\mathrm{q}}$ and standard deviation $\sigma_{\mathrm{S2}} = r\sqrt{\mu_{\mathrm{q}}} = \sqrt{r\mu_{\mathrm{S2}}}$:

$$p_2(n_2, E_{\mathrm{nr}}) = \frac{1}{\sqrt{2\pi r\mu_{\mathrm{S2}}(E_{\mathrm{nr}})}} \exp\left(-\frac{(n_2 - \mu_{\mathrm{S2}}(E_{\mathrm{nr}}))^2}{2r\mu_{\mathrm{S2}}(E_{\mathrm{nr}})}\right) \; . \tag{3.5}$$

For the XENON100 experiment, the amplification factor r has been determined from calibration data to equal $r = 17.6\,\mathrm{phe/e^-}$ [32].

3.2 Simulation of the nuclear recoil band

Equation (3.3) and equation (3.5) as well as the assumption that the two signals are uncorrelated summarize our model for the distribution functions that describe the fluctuations of $S1$ and $S2$ signals. To test our model and check the underlying assumptions, we would like to make predictions that can be compared to experimental data. What we want to predict is the shape of the nuclear recoil band, which can be determined experimentally from calibration with AmBe (see figure 2.6).

Monte Carlo simulations of the nuclear recoil band are a difficult task, because we must be careful to precisely reproduce the experimental conditions. First of all, we need to know the energy spectrum of neutron recoils expected for calibration
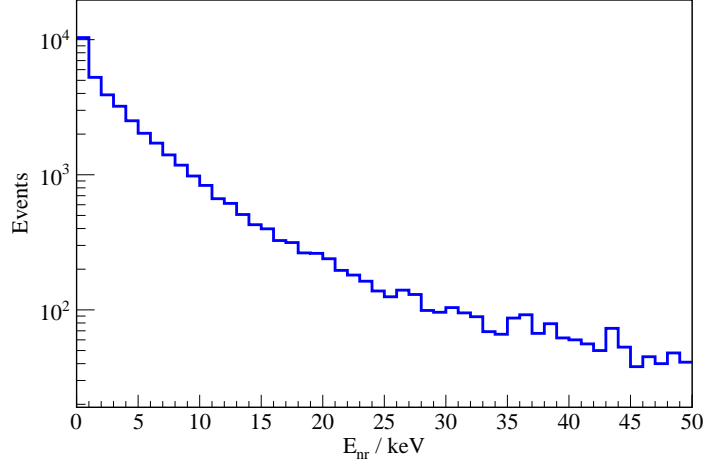
Figure 3.1: The neutron recoil energy spectrum for single scatters obtained from Geant4 simulations of the XENON100 detector.

with AmBe. Such an energy spectrum can be extracted from the Geant4 simulations performed by the XENON100 collaboration (see figure 3.1).[1] From these simulations, we can also obtain additional information for each event, for example the number of energy deposition steps and the position of each scattering process.[2]

To reproduce actual signals in the detector, we must convert the energy spectrum into $S1$ and $S2$ signals. First, we calculate the expectation values μ_{S1} and μ_{S2} using the best-fit choice for $\mathcal{L}_{\text{eff}}$ from figure 2.5 and the ionization yield measured by Manzur et al. [33] (see figure 3.2). Then, we randomly generate $S1$ and $S2$ signals according to the respective distribution functions. An additional Gaussian smearing with $\sigma = 1$ is applied to both signals to account for the finite PMT resolution.

Next, we need to make sure that we correctly treat the time and position resolution of the detector. In an event with more than one scattering process, the detector cannot distinguish the different $S1$ signals, because it cannot resolve the time between two scattering processes. Consequently, to compare simulated signals to experimental ones, we must add up all $S1$ signals occurring in one event, carefully taking into account the position dependence of the light collection efficiency. On the other hand, the S2 signals can be distinguished if the z-position is separated by at least $3\,\text{mm}$, so we add up $S2$ signals only for neutron recoils that occur very close to each other. As it is done in the analysis of the experimental data, if there remains more than one $S2$ signal, we keep only the largest one.[3]

---

[1]The relevant data files were kindly provided by Alexander Kish.

[2]Note that the term "event" refers to the propagation of one neutron through the detector. Consequently one event may comprise more than one scattering process.

[3]In the experimental analysis, events with more than one $S2$ signal are usually removed by the single scatter cut (see section 3.3.2). However, we do not impose such a cut because we do not
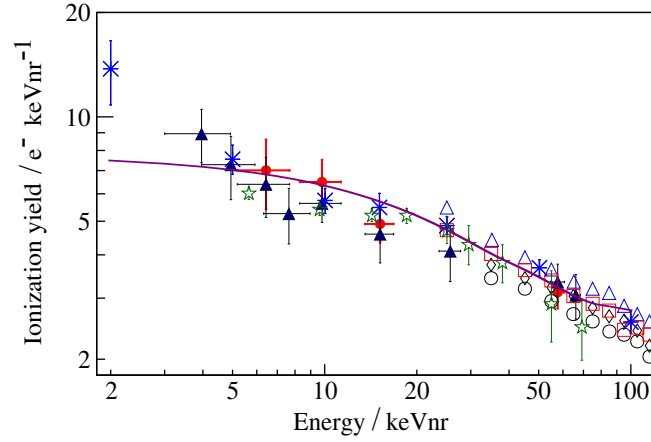
Figure 3.2: The adapted fit for the ionization yield Q_y in electrons produced per nuclear recoil energy (violet line). The data points are taken from [33]. Note that most measurements have been performed at stronger electric field than the one employed by XENON100 ($E = 0.5\,\mathrm{kV/cm}$).

In the next step, we need to make sure that we include only events in our simulation that would also be recorded during a calibration run. We require that the largest $S2$ signal must be greater than $300\,\mathrm{phe}$ and lie inside the $40\,\mathrm{kg}$ fiducial volume (see figure 2.3). Note that we do not impose any restrictions on the magnitude of the $S1$-signal, so we include events with $S1 < 4\,\mathrm{phe}$. In this region, the acceptance of the detector is expected to be pretty low (because the signal can hardly be distinguished from noise), but this problem should not affect the shape of the nuclear recoil band. We will come back to the discussion of the acceptance in section 3.3.

For all simulated events we plot $\log_{10}(S2/S1)$ versus $S1$. We take the logarithm because for normally distributed $S1$ and $S2$, the quotient $S2/S1$ is similar to a log-normal distribution, so $\log_{10}(S2/S1)$ should be approximately normally distributed. Therefore, we can use the median and the upper and lower 15.87% and 2.27% quantiles to approximate the mean and the 1σ and 2σ region of the nuclear recoil band for each $S1$ bin. The resulting plot is shown in figure 3.3. We indeed obtain good agreement with experimental data in the absolute position of the nuclear recoil band, which is essentially determined by our choice of the scintillation yield and the ionization yield, and the width of the band, which is essentially determined by our assumptions on the distribution of $S1$ and $S2$ signals.

Only at large values of $S1$, we observe a deviation between the experimental and the simulated nuclear recoil band. The most likely explanation is that we have chosen slightly too small values for Q_y. Also note that the 2σ region of the nuclear

---

want to reduce the number of events without necessity.
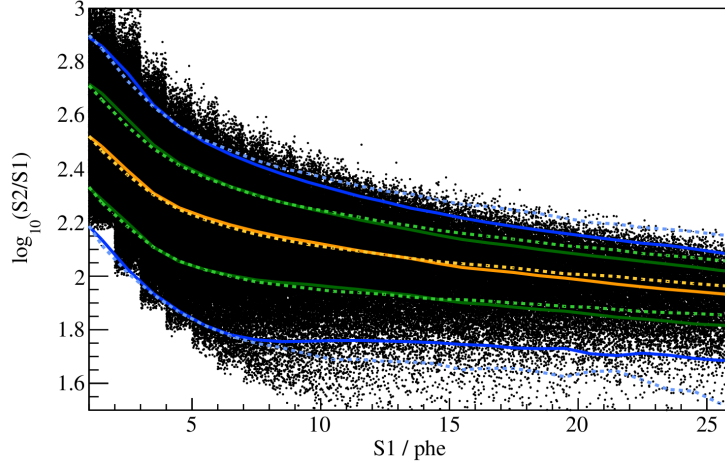
Figure 3.3: A Monte Carlo simulation of the nuclear recoil band. The yellow solid line corresponds to the median value, the green and blue solid lines indicate the 1σ and 2σ region respectively (more precisely, the upper and lower 15.87% and 2.27% quantiles). The dashed lines show the corresponding values for experimental data.

recoil band is somewhat broader in the experimental data than in the simulation. The reason is that one observes experimentally a small number of anomalous events leading to non-Gaussian tails in the nuclear recoil band that broaden the 2σ region. The most likely explanation for these events is that they happen close to the surface of the detector and suffer from incomplete collection of photons and electrons.

The simulated nuclear recoil band would look quite different had we taken the conservative choice of $\mathcal{L}_{\mathrm{eff}}$ instead of the best-fit one. This observation is a first hint that the relative scintillation efficiency does not decrease at very low recoil energies but rather remains constant. We will come back to this question in the next chapter, but we will stick to the conservative choice for $\mathcal{L}_{\mathrm{eff}}$ in this chapter nevertheless to give a conservative estimate of the detector sensitivity. The central information that we wanted to obtain from the simulation of the nuclear recoil band is that indeed our model for the distribution functions of $S1$ and $S2$ signals is very accurate.

3.3 Cut acceptances

As we have pointed out in section 3.2, not every scattering process with sufficiently large $S1$ and $S2$ signals will indeed be accepted as a valid event. The reason is that we must require every signal to fulfill certain conditions in order to ensure data quality and reject noise. For example, to prevent signals from PMT dark counts, we require a two-fold coincidence for every $S1$ signal, meaning that we accept an event only if two PMTs observe an $S1$ signal simultaneously. While such a cut is necessary
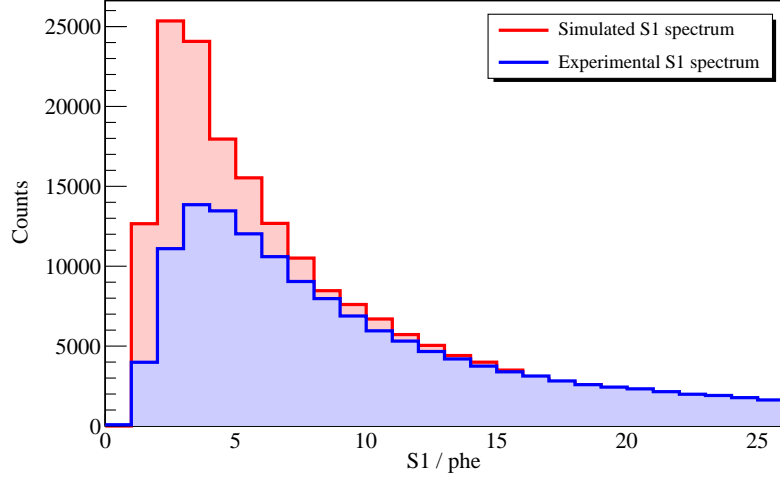
Figure 3.4: Comparison of the $S1$ spectra obtained from the projection of the nuclear recoil band on the x-axis. The red histogram shows the results from Monte Carlo simulations, while the blue histogram shows the corresponding $S1$ spectrum from calibration data. We have chosen the normalization in such a way that the two spectra agree approximately for large values of $S1$.

to obtain meaningful data, there is a certain risk that it also removes valid events.

We define the *acceptance* of a cut as the probability that the cut accepts a valid event and the *efficiency* of a cut as the probability that it rejects an invalid event. Clearly, we can increase the efficiency of a cut by making the cut more stringent, but doing so will reduce its acceptance and vice versa. In general, the acceptance will be a function of $S1$, which we denote by $a_{\mathrm{cut}}(S1)$. If $a_{\mathrm{cut}}(S1)$ is very small at small $S1$, the sensitivity of the detector in the low energy region will be reduced.

Problems with noise and data quality are not present in Monte Carlo simulations. We can therefore use the simulations discussed in section 3.2 to determine the cut acceptance of the detector. For this purpose, we want to make a quantitative comparison of experimental and simulated data rather than a qualitative one as in figure 3.3. To do so, we project the nuclear recoil band on the x-axis and calculate the number of events in each $S1$ bin (called the *S1 spectrum*).

Figure 3.4 shows the $S1$ spectra for calibration data and the data obtained from Monte Carlo simulations. The relative scale of the two spectra is arbitrary and has been chosen in such a way that the two spectra match approximately for large $S1$. We can see that both spectra show a similar behavior, with a maximum at about $S1 = 3\,\mathrm{phe}$. The decrease for larger values of $S1$ results from the exponential decrease of the neutron recoil spectrum (see figure 3.1). The decrease for smaller values of $S1$, on the other hand, does not have a physical reason, but is due to the cuts that we apply to the data.

The key observation is that the two spectra agree quite well at large energies, but
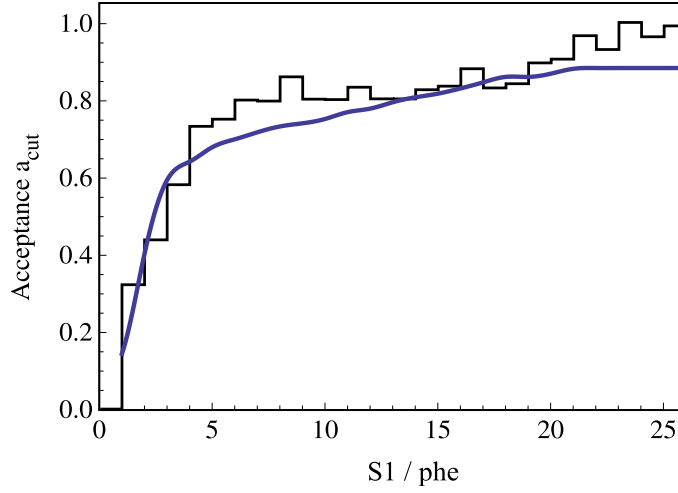
Figure 3.5: Determination of the cut acceptance $a_{\mathrm{cut}}(S1)$ from Monte Carlo simulations. The histogram is calculated by dividing the experimental $S1$ spectrum shown in figure 3.4 by the simulated one. The blue line indicates the published results for the acceptance function from reference [30]. Note that the normalization of the histogram is arbitrary, so we have chosen it in such a way that $a_{\mathrm{cut}} = 0.9$ for $S1 = 20\,\mathrm{phe}$.

begin to deviate as $S1$ decreases below $10\,\mathrm{phe}$. This deviation is the result of the cut acceptance of the detector. For the Monte Carlo simulation, the only relevant cut is the requirement $S2 > 300$. For the experimental data, the number of $S1$ signals is reduced further by the acceptance of the data quality cuts. We can quantify the acceptance function a_{cut} by dividing the $S1$ spectrum from calibration data by the simulated spectrum. Again, since we do not know the relative scale of the two spectra, we cannot determine the normalization of the acceptance function.

We present our result for the acceptance function in figure 3.5. The normalization has been chosen arbitrarily so that $a_{\mathrm{cut}} = 0.9$ at $S1 = 20\,\mathrm{phe}$. For comparison, we also plot the acceptance function that has been published together with the first results of the XENON100 experiment [30]. The two functions indeed agree remarkably well. Only in the region above $S1 = 20\,\mathrm{phe}$, we observe that the ratio of experimental $S1$ signals and simulated $S1$ signals continues to increase, although we would expect the acceptance function to be more or less constant. This increase could either point to shortcomings of the neutron energy spectrum that we take from Geant4 simulations, or to the presence of anomalous events in the calibration data. In fact, the non-Gaussian tails that we have observed already in figure 3.3, may also account for the slower decrease of the experimental $S1$ spectrum towards larger recoil energies. Because we are only interested in the region $4 \leq S1 \leq 20$, we will use the published values for a_{cut} for all calculations in the following.

So far, we have only considered the cuts that are needed to reject noise and ensure

data quality. However, for the dark matter search we must apply two additional cuts in order to reject background from neutrons and γ-rays (see chapter 2.4). These cuts are the *single scatter cut*, which is used to identify and remove neutrons, and the *nuclear recoil cut*, which distinguishes between electron recoils and nuclear recoils in order to reject background from γ-rays. However, the acceptance for these two cuts is difficult to determine and presently unknown. In the remainder of this section, we will discuss the related difficulties.

3.3.1 Single scatter cut

Neutrons typically scatter more than once inside the active volume. We can therefore effectively remove background from neutrons by requiring that there should be only one $S2$ peak in a valid event. Unfortunately, it turns out that even valid single scatter events sometimes have more than one $S2$ peak due to noise or delayed electrons. Removing all events with more than one $S2$ peak would therefore dramatically reduce the cut acceptance for valid single scatter events.

To maintain a high acceptance for single scatters, one usually relaxes the single scatter cut and removes only those events that have a second $S2$ peak above 300 phe. Of course, doing so will also reduce the rejection efficiency for multiple scatters. In consequence, we must expect a larger number of background events. Moreover, what is even worse, if we cannot efficiently reject multiple scatters, the nuclear recoil band from AmBe calibration will be distorted. The reason is that we cannot distinguish the different $S1$ signals of multiple scatters but measure only their sum (see section 3.2). Thus, if we cannot reject all multiple scatters, we will get a number of events that have a large $S1$ signal compared to their $S2$ signal. For these events $\log_{10}(S2/S1)$ will be comparably small, so the nuclear recoil band for multiple scatters lies below the nuclear recoil band for single scatters (see figure 3.6).

This effect would not be a problem if the number of single scatters were much larger than the number of multiple scatters that are not rejected. Unfortunately, because of the exponentially falling neutron spectrum (see figure 3.1), we must expect large numbers of multiple scatters with only one $S2$ peak above 300 phe. In fact, we obtain from Monte Carlo simulations, that the number of multiple scatter events, which pass the relaxed single scatter cut, is almost as big as the number of true single scatters (in figure 3.6, there are $8.0 \cdot 10^4$ multiple scatters compared to $9.1 \cdot 10^4$ single scatters). Consequently, the contribution of multiple scatters will effect a significant distortion of the nuclear recoil band.

This distortion is a serious problem because it means that we cannot easily infer the nuclear recoil band for true single scatter from calibration with neutrons. To mitigate this problem, one could consider to apply a stronger single scatter cut, for example by requiring that any additional $S2$ peak must be smaller than 100 phe. For this modified cut, multiple scatters contribute only about 20% to the total number of events. Moreover, scattering processes with an $S2$ signal below 100 phe will in most
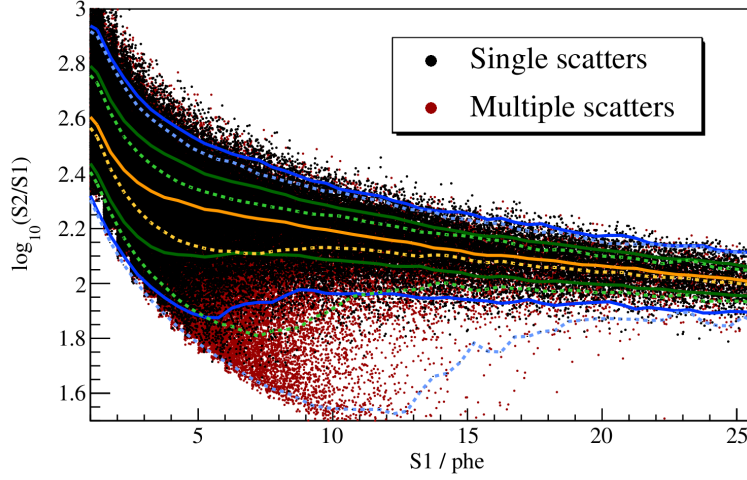
Figure 3.6: A Monte Carlo simulation of the nuclear recoil band. The black dots are true single scatters, while the red dots are multiple scatters that pass the single scatter cut (only one $S2$ signal above 300 phe). Solid lines indicate the median (yellow), as well as the 1σ (green) and 2σ (blue) region for true single scatters. The dashed lines show the corresponding values for multiple scatter events.

cases give only a negligible contribution to the sum of $S1$ signals. Consequently, we can hope for a much smaller distortion of the nuclear recoil band. At the same time, however, the modification reduces the acceptance of the single scatter cut, which will affect the sensitivity of the detector.

To understand the acceptance and the rejection efficiency of the single scatter cut and determine the nuclear recoil band for true single scatters is certainly one of the most important open problems for the data analysis of XENON100. As it is not yet clear, which single scatter cut the XENON collaboration will decide to use, we cannot at this point determine the corresponding acceptance function. We will assume in the following, however, that the acceptance of the single scatter cut does not limit the sensitivity of XENON100 in the low energy region.

3.3.2 Nuclear recoil cut

We can discriminate electron recoils and nuclear recoils, because for comparable $S1$ signals the former have much larger $S2$ signals. Consequently, to reject electron recoils, we discard all events that have a large ratio of $S2/S1$. To achieve a sufficiently high rejection efficiency,[1] one in fact removes all events that lie above the median of the nuclear recoil band (the yellow line in figure 3.3). By construction, this cut will also remove 50% of all nuclear recoils and consequently reduce dramatically the

---

[1]As we shall see in chapter 5, the rejection efficiency must be 99% or better.

(a) $\mu_{S1} = 10$ and $\mu_{S2} = 1400$ (b) $\mu_{S1} = 3$ and $\mu_{S2} = 500$
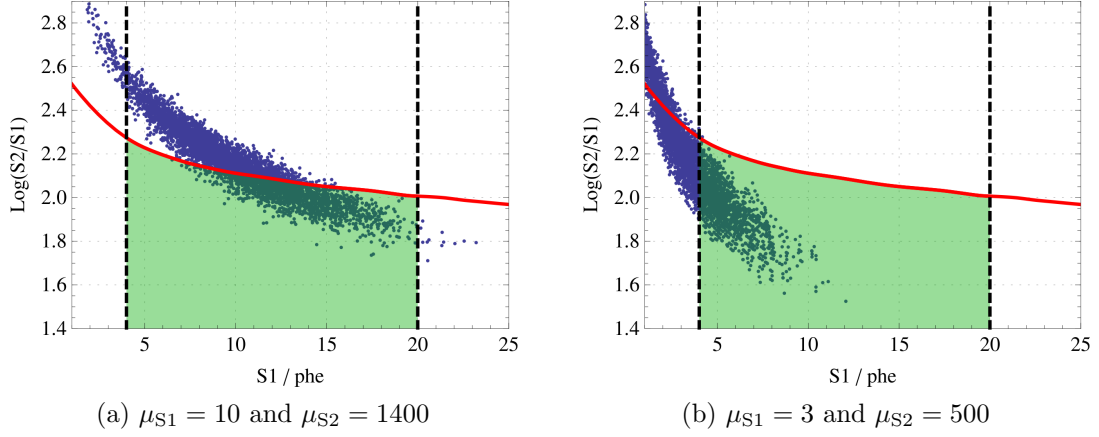
Figure 3.7: Distribution of events in the $\log_{10}(S2/S1)$ versus $S1$ plane for fixed expectation values of $S1$ and $S2$. The red line indicates the nuclear recoil cut. The green shaded area corresponds to the acceptance region after the requirement $4 \leq S1 \leq 20$ and the nuclear recoil cut have been applied.

acceptance of the detector.

Naively, we could try to include this cut by simply multiplying the cut acceptance from figure 3.5 with 0.5. However, at this point we encounter a very fundamental problem related to the determination of cut acceptances. As Sorensen first pointed out in [34], if we apply several cuts to our data set, the acceptance probabilities of the different cuts may not be independent, so we cannot simply multiply them. To make this statement more precise, we shall rephrase it in mathematical terms. If $p(c1)$ is the probability that an event passes cut 1 and $p(c2)$ is the probability that this event passes cut 2, then we can express the probability that is passes both cuts as $p(c1 \wedge c2) = p(c2|c1) \cdot p(c1)$, where $p(c2|c1)$ is the conditional probability that the event passes cut 2 if it has already passed cut 1. Consequently, the naive multiplication of cut acceptances, such as $p(c1 \wedge c2) = p(c2) \cdot p(c1)$, will only be valid if $p(c2|c1) = p(c2)$. In the following, we will give a simple example for two cuts, which are not independent, so that $p(c2|c1) \neq p(c2)$. Therefore, a simple multiplication of cut acceptances will not do in this case.[1]

The cuts that we want to consider are the nuclear recoil cut (nr cut) and the requirement $4 \leq S1 \leq 20$. In the following, we want to demonstrate that

$$a_{\mathrm{nr}} \equiv p(\mathrm{nr\ cut}|4 \leq S1 \leq 20) \neq p(\mathrm{nr\ cut}) = 0.5 . \tag{3.6}$$

To understand why these two cuts are not independent, remember that, because of the poor energy resolution of the detector, nuclear recoils with a fixed energy will

---

[1]In fact, this problem occurs whenever a cut depends not only on $S1$, but also on $S2$.

scatter widely in the $\log_{10}(S2/S1)$ versus $S1$ plane. As an example, we show in figure 3.7a a large number of events that have been generated using the distributions from section 3.1 with $\mu_{S1} = 10$ and $\mu_{S2} = 1400$. If we only consider events inside the $S1$ search window, we observe that some of them fall above and others below the nuclear recoil cut. In this case, the nuclear recoil cut effectively reduces the number of accepted events, so $a_{nr} < 1$.

However, if we now make the same plot for the choices $\mu_{S1} = 3$ and $\mu_{S2} = 500$, we get a somewhat different picture (see figure 3.7b). Almost all events that pass the $S1 \geq 4$ requirement, automatically pass the nuclear recoil cut as well. The reason is obvious: The events that we have simulated here produce on average less than 4 photoelectrons. If 4 or more photoelectrons are produced due to fluctuations, the $S1$ signal will be large compared to the $S2$ signal (remember that we assume $S1$ and $S2$ fluctuations to be independent). Consequently, such an event will have a low value of $\log_{10}(S2/S1)$. In this case, the nuclear recoil cut is almost without effect - all recoils with large value of $\log_{10}(S2/S1)$ are already removed by the $S1$ cut. Consequently, in this case $a_{nr} \approx 1$.

For this reason, the nuclear recoil cut acceptance depends on the recoil energy and can in fact be much larger than 50% towards lower energies. In order to properly calculate the cut acceptance, we must take into account the probability distributions for S1 and S2 signals. If we define a function $f(S1)$ to parameterize the nuclear recoil cut, meaning that we require $\log_{10}(S2/S1) < f(S1)$, we can translate this inequality into

$$S2 < S1 \cdot 10^{f(S1)} \equiv g(S1) . \tag{3.7}$$

Using $p(c2|c1) = p(c1 \wedge c2)/p(c1)$, the nuclear recoil cut acceptance $a_{nr}(E_{nr})$ is given by:

$$a_{nr}(E_{nr}) = \frac{\sum\limits_{n_1=4}^{20} p_1(n_1, \mu_{S1}(E_{nr})) \cdot \sum\limits_{n_2=300}^{g(n_1)} p_2(n_2, \mu_{S2}(E_{nr}))}{\sum\limits_{n_1=4}^{20} p_1(n_1, \mu_{S1}(E_{nr}))} . \tag{3.8}$$

Again, we cannot presently calculate $a_{nr}(E_{nr})$, because the nuclear recoil band for single scatters and therefore $g(S1)$ has not yet been extracted from calibration data (see the discussion in the previous section). Until the cuts have been finalized and we have a proper description of the nuclear recoil band, we must use the simple approximation that the nuclear recoil cut acceptance is 50% for all recoil energies. Since we expect that $a_{nr}(E_{nr}) > 0.5$ at low recoil energies, taking $a_{nr} = 0.5$ everywhere should give a conservative estimate of the acceptance in this region. On the other hand, a constant nuclear recoil cut acceptance will overestimate the acceptance for high recoil energies, but here only few events are expected anyways.

3.4 The total acceptance function

In this section, we will put all the pieces together and introduce a convenient framework to discuss the sensitivity of liquid xenon detectors. The idea is to split the calculation of exclusion limits into two parts: The first part contains everything related to the performance of the detector and the second part contains the actual physics of dark matter. In fact, all relevant detector properties can be summarized in one simple function which we will call the *total acceptance function $A(E_{nr})$*. For a given nuclear recoil energy E_{nr}, $A(E_{nr})$ gives the probability that a nuclear recoil with this energy leads to a signal within the search window (meaning within a given range of photoelectrons). Multiplying the total acceptance function with the differential WIMP spectrum dR/dE_{nr} then gives the actual differential event rate in the detector (see also appendix B).

The question is how to obtain $A(E_{nr})$. Neglecting fluctuations, we could simply convert E_{nr} into photoelectrons by inverting equation (2.16). The function $A(E_{nr})$ would then equal 1 if $S1(E_{nr})$ lies within the search window, $S1_{min} \leq S1 \leq S1_{max}$, and 0 otherwise. However, in section 3.3, we have seen that the acceptance of the detector is smaller than 1 even inside the search window because of the cuts that we apply to ensure data quality and reject background (a_{cut} from figure 3.5). Consequently, $A(E_{nr}) = a_{cut}(S1(E_{nr}))$ if $S1(E_{nr})$ lies within the search window and 0 otherwise (see the green line in figure 3.8).

Because of fluctuations, as discussed in section 3.1, we cannot express $S1$ as a function of the nuclear recoil energy. Consequently, we must use the probability distribution from equation (3.3) to calculate $A(E_{nr})$:

$$A(E_{nr}) = \sum_{n_1=S1_{min}}^{S1_{max}} p_1(n_1, \mu_{S1}(E_{nr})) \cdot a_{cut}(n_1) \,. \tag{3.9}$$

As a result, there will be a smearing of the total acceptance function: Recoil energies that would be rejected in the absence of fluctuations have a non-zero chance to produce a sufficient number of photoelectrons. At the same time, events inside the acceptance window will — with a certain chance — produce too few or too many photoelectrons to give a detectable signal. The result of this smearing is indicated by the blue line in figure 3.8. As expected, the inclusion of fluctuations leads to a dramatic increase of the acceptance for events with a low recoil energy. For recoil energies just slightly below the threshold, acceptance is indeed larger than 30% and even at a recoil energy of 5 keV, the acceptance is still about 1%.

Considering that we will multiply the total acceptance function $A(E_{nr})$ with an exponentially decreasing dark matter spectrum, the precise form of the acceptance function at very low energies will be extremely important. One could be worried, that here our approximation of Poisson statistics will break down. It is therefore advisable to calculate $A(E_{nr})$ for both, a Poisson distribution and a Binomial distribution of

Figure 3.8: The total acceptance function $A(E_{\mathrm{nr}})$. The green (dashed) line corresponds to the total acceptance function neglecting fluctuations. The red (solid) line and the blue (dotted) line correspond to fluctuations described by Binomial and Poisson statistics respectively.

$S1$ signals, to see whether the two agree and our approximation is actually valid.

In order to calculate $A(E_{\mathrm{nr}})$, we will use Monte Carlo simulations.[1] For a given recoil energy, we calculate $\mu(E_{\mathrm{nr}})$ using the conservative choice of $\mathcal{L}_{\mathrm{eff}}$ shown in figure 2.5, and calculate $N_{\mathrm{ph}} = \mu(E_{\mathrm{nr}})/(QE \cdot LCE)$ with $LCE = QE = 0.25$. Now we use Binomial statistics (with probability LCE) to randomly determine the number of photons that hit a PMT and again Binomial statistics (with probability QE) to determine the number of photoelectrons produced. Repeating this process for a very large number of events will give the probability distribution for the number of photoelectrons produced by a nuclear recoil with energy E_{nr}. We can then substitute this distribution for p_1 into equation (3.9) to calculate $A(E_{\mathrm{nr}})$.

The result of this calculation is shown as the red line in figure 3.8. A comparison between the results obtained from assuming Poisson statistics and the Monte Carlo simulation based on Binomial statistics reveal that indeed Poisson statistics approximate the Binomial distribution very well.

To conclude this chapter, we will turn to a discussion of additional contributions to $S1$ fluctuations that may further reduce the resolution of the detector and thus improve the detector sensitivity. However, it will turn out that we have already captured the main contribution to fluctuations and all additional effects will give only minor, in fact negligible, corrections. In this context, the framework of an acceptance function will be very convenient, because $A(E_{\mathrm{nr}})$ can be understood much more intuitively than an exclusion plot. Moreover, the large disadvantage of exclusion plots is, that they depend on various parameters from particle physics and

---

[1]The calculations presented here could be done analytically as well. However, when we want to include the light collection efficiency, Monte Carlo simulations will be necessary.

astrophysics and consequently are much harder to reproduce and compare.

A possible contribution to $S1$ fluctuations could come from the production mechanism of scintillation photons. So far, we have assumed that N_{ph} is fixed for a given recoil energy, but of course the emission of scintillation light is also a statistical process, so we should expect a varying number of photons even for fixed recoil energy. Again, Poisson statistics are appropriate to describe the production process.[1] From the discussion above, we know that $N_{\mathrm{ph}} \approx 16n$, so

$$\frac{\Delta N_{\mathrm{ph}}}{N_{\mathrm{ph}}} = \frac{1}{\sqrt{N_{\mathrm{ph}}}} \approx \frac{1}{4\sqrt{n}} = \frac{1}{4}\frac{\Delta n}{n} \ . \tag{3.10}$$

The fluctuations that occur in the production process are a factor of 4 smaller than the fluctuations in the detection process. We therefore expect that only the detection process is relevant for the detector resolution. We can easily confirm this expectation by extending the Monte Carlo simulations from above to include fluctuations of the initial number of photons in an additional step (see figure 3.9a).

Another possible contribution to fluctuations is more difficult to treat. So far we have considered the detector to be homogeneous so that we could neglect the position of the primary event. However, in a more realistic description, the light collection efficiency (LCE) will depend on the position of the primary event: Events close to the PMT arrays will have a larger LCE than those in the center of the detector (see chapter 5.2 and figure 5.3). This inhomogeneity effects a variation of the number of produced photoelectrons even in the absence of other statistical processes.

Again, Monte Carlo simulations allow to quickly estimate the magnitude of this effect. This time the position of each event is set randomly within the $40\,\mathrm{kg}$ fiducial volume from figure 2.3. The actual light collection efficiency for each position is then taken from calibration data of the detector [32]. We can see in figure 3.9b that at low energies, the total acceptance function is still completely dominated by the Poisson fluctuations of the detection process and including LCE variations gives almost no improvement. Nevertheless, the sensitivity above the upper threshold improves significantly by including LCE variations.

This result is intuitively clear, because $\Delta LCE/LCE$ is a detector property and independent of the recoil energy, so the variation of the light collection efficiency will only be important if $\Delta n/n$ is sufficiently small. However, since only few events are expected at high recoil energies, exclusion limits will not change significantly by including the variation of light collection efficiency. At best, including LCE variations may slightly improve the sensitivity for heavy dark matter.

---

[1]In principle the width of the distribution could be modified by a Fano factor. If this factor is much smaller than one, we can certainly neglect fluctuations of N_{ph}. Consequently, we assume here that the Fano factor is approximately equal to one.

(a) Varying photon number

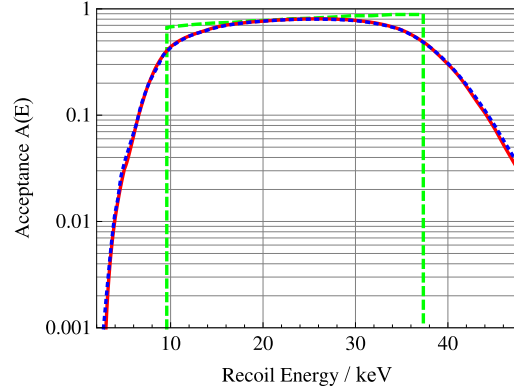(b) Varying light collection efficiency
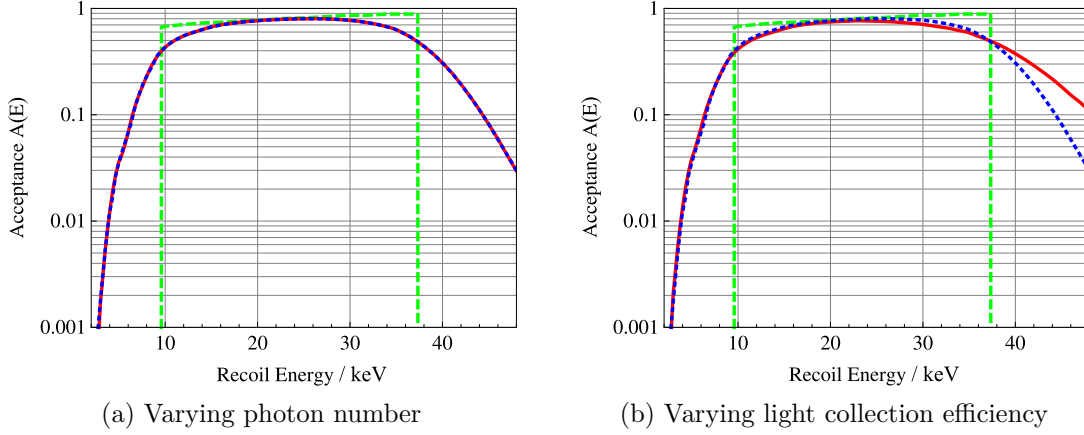
Figure 3.9: The total acceptance function $A(E_{\mathrm{nr}})$. Again, the green (dashed) line corresponds to the total acceptance function neglecting fluctuations and the blue (dotted) line corresponds to fluctuations described by Poisson statistics. The red (solid) line includes different subdominant contributions to the fluctuations of the $S1$ signal. As expected, no significant improvement of the total acceptance function is obtained in the low energy region.

3.5 Summary of results

In this chapter, we have provided good arguments that Poisson statistics are appropriate to describe $S1$ fluctuations, while an additional amplification factor r must be included to describe the fluctuations of the $S2$ signal. A more detailed description of the various processes involved in the production and detection of scintillation light do not change this conclusion significantly. We have checked our model using Monte Carlo simulations, which do not only confirm our assumptions, but also allow to determine the acceptance of the detector for low energy recoils. We obtain that the acceptance of the data quality cuts is greater than 60% for $S1 \geq 4\,\mathrm{phe}$, in agreement with previously published results.

In conclusion, liquid xenon detectors possess a significant sensitivity even in the energy region that is naively below the lower threshold of the detector. Of course, all our calculations in this chapter rely on the assumption that indeed a sufficient amount of scintillation light is produced even at very low recoil energies. The critical review of this assumption will be the topic of the following chapter. Once we have obtained a prediction for the effective scintillation yield at low recoil energies, we can use the results from this chapter to calculate the expected sensitivity for the XENON100 experiment (see chapter 4.5).

The effective scintillation yield of liquid xenon

In this chapter we will discuss the effective scintillation yield for liquid xenon, a quantity that is both essential for calculating exclusion limits and highly controversial. At least, we know that scintillation light is strongly suppressed for nuclear recoils compared to electron recoils. The reason is that a recoiling nucleus can effectively loose its energy through elastic collisions with other nuclei in the detector. Most of the initial recoil energy is thus transferred, eventually, to heat. Recoiling electrons, in contrast, cannot transfer any significant amount of their energy to nuclei because of the huge difference in mass. They will transfer all their energy into electronic excitations, and thus produce a larger amount of scintillation light.

Conventionally, the effective scintillation yield of nuclear recoils is described by the dimensionless quantity $\mathcal{L}_{\mathrm{eff}}$, called relative scintillation efficiency. It relates the $S1$ scintillation signal to the physical recoil energy of the nucleus E_{nr} as

$$E_{\mathrm{nr}} = \frac{S1}{L_{\mathrm{y}} \cdot \mathcal{L}_{\mathrm{eff}}} \cdot \frac{S_{\mathrm{ee}}}{S_{\mathrm{nr}}} \ . \tag{4.1}$$

L_{y} is the light yield for $122\,\mathrm{keV}$ electron recoils in the presence of an electric field and $S_{\mathrm{ee,nr}}$ are the electric field quenching factors for electronic and nuclear recoils (see chapter 2.4). Thus, $\mathcal{L}_{\mathrm{eff}}$ quantifies the suppression of scintillation for nuclear recoils compared to $122\,\mathrm{keV}$ electron recoils at zero electric field.

It is generally agreed that the relative scintillation efficiency will depend on the nuclear recoil energy. How this dependence should look like is presently unclear from both experimental and theoretical point of view. Many measurements of the relative scintillation efficiency have been carried out, giving a wide range of (partly contradictory) results (see [33, 35–41] as well as figure 2.5). However, most measurements imply at least a slight decrease of the relative scintillation efficiency with decreasing energy.

On the theoretical side the problem is to understand the production of scintillation light for a slow moving xenon atom. This problem can be roughly divided into three parts. First we need to know the ionization and excitation probabilities for individual collisions of xenon atoms. Then we must simulate the propagation of

recoiling atoms to determine the total amount of electronic excitations, and finally we must understand the recombination rate for the produced free electrons and ions. At the end, a theoretical treatment of the problem should produce predictions for *both* the scintillation and the ionization signals produced in the detector.

In section 4.1 we review the process of generation of scintillation light and ionization in liquid xenon. We introduce the notion of the nuclear and electronic stopping powers in section 4.2 in order to perform an analysis of individual xenon scattering events. From the results we calculate the total energy in the electronic excitations. In section 4.3, we then analyze the recombination process. In section 4.4 all the results are collected and translated into the ionization and scintillation yields and compared with the experimental data.

4.1 Production of scintillation light in liquid xenon

A large variety of effects must be taken into account to describe all physical processes that lead from the initial recoil to the production of scintillation light in liquid xenon. Specifically, we expect the following steps [42]:

- In an interaction with a dark matter particle, an energy of 1–100 keV is transferred to the nucleus. As the corresponding recoil velocity is well below the Fermi velocity of the most loosely bound electrons, we expect the atom to remain neutral in the scattering process.

- The recoiling atom will scatter off neighboring nuclei. While most scattering events are expected to be elastic, there will occasionally be inelastic collisions leading to excitation or ionization of either (or both) of the atoms.

- After each scattering process, both atoms will continue their propagation with a fraction of the initial recoil energy. Consequently, both can again scatter elastically or inelastically off other atoms.

- During the process of thermalization, the recoiling xenon atoms will leave behind a large number of ionized or excited xenon atoms — distributed along many branches of the initial track.

- The free electrons will now either recombine with surrounding ions to form excited xenon atoms or escape from recombination. The fraction of escaping electrons will depend on the strength of the applied electric drift field, but some electrons will escape even in the absence of a field.

- Excited xenon atoms are free initially, but will soon be self-trapped and form *excimers*. These excimers emit vuv scintillation light on the transition to the

ground state. In a simplified picture, the process is

$$\mathrm{Xe}^* + \mathrm{Xe} \rightarrow \mathrm{Xe}_2^* \tag{4.2}$$

$$\mathrm{Xe}_2^* \rightarrow 2\mathrm{Xe} + h\nu \tag{4.3}$$

- In some cases, especially at high excitation density, two exited xenon atoms will combine to produce only one scintillation photon. This process, known as *biexcitonic quenching*, will effectively reduce the scintillation yield.

At first sight, the large number of steps makes it very hard to disentangle possible ambiguities. A decrease of scintillation efficiency at low recoil energies could be equally attributed to a decreasing cross section for inelastic scattering (for example due to threshold effects), a different track structure, an increasing fraction of escaping electrons or a stronger quenching mechanism. This ambiguity can be lifted at least partially by considering not only the relative scintillation efficiency of nuclear recoils, but also the ionization yield. This quantity is much better determined experimentally (because free electrons can be extracted with high efficiency and the signal can be strongly amplified in the gas phase), but has been — to the best of our knowledge — ignored in all previous attempts to give a theoretical model for the scattering processes in liquid xenon.

The sum of ionization and scintillation, which we will refer to as the *total electronic excitation*, should correspond to the total energy lost in inelastic collisions. Consequently, it should only depend on the scattering cross sections and not on the processes occurring later, such as recombination, which will only lead to a redistribution between ionization and scintillation. Thus, if both signals showed a similar energy dependence, this would suggest a general suppression of inelastic scattering at low energies — which is what one might naively expect. However, what is actually observed experimentally, is a strong increase of the ionization yield at low energies. This observation indicates that the suppression of the scintillation signal at low energies does not result from the actual inelastic scattering processes, but from the large number of escaping electrons.

4.2 Stopping powers of liquid xenon

In this section we will describe the interactions of neutral xenon atoms and discuss possible scattering processes at energies of a few keV. The quantities we are interested in are the rate at which energy is transferred to recoiling nuclei by elastic collisions and the rate at which electrons are excited by inelastic collisions. These quantities are often called *nuclear stopping power* and *electronic stopping power*.

4.2.1 Electronic stopping power

The electronic stopping power is defined as the average energy which an atom loses to electronic excitations per distance traveled through the detector:

$$S_e = \frac{\mathrm{d}E}{\mathrm{d}x} \ . \tag{4.4}$$

In a "semiclassical" approach, an electron is excited when it collides with a nucleus.[1] The stopping power should therefore be proportional to the electron mass density n_0, their velocity v_F, the momentum transfer cross section $\sigma_{tr}(v_F)$, and the velocity of the incoming particle v. In fact, electronic stopping is often described by [43–47]

$$S_e = n_0 v v_F \sigma_{tr}(v_F) \ . \tag{4.5}$$

We should take a moment to discuss the validity of such a semiclassical approach. Equation (4.5) is in fact based on several assumptions:

- Instead of describing the atomic system by a many-particle wavefunction, we claim that only the electron density is relevant to the problem, and we ignore the modification of the electron density during the atomic collision.

- Collisions between electrons and nuclei are treated like classical point like interactions.

- Electrons are assumed to be free. Consequently, no minimal energy transfer is required for an excitation.

For a uniform electron gas the electronic stopping power is proportional to the velocity of the incoming particle, a result that has been derived by Lindhard et al. [48]. The authors obtain

$$S_e = \sqrt{8}\pi e^2 a_0 \zeta_0 Z N \cdot \frac{v}{v_0} \ , \tag{4.6}$$

where a_0 and v_0 are Bohr radius and Bohr velocity respectively and ζ_0 is an empirical parameter, often[2] set to $\zeta_0 = Z^{1/6}$. Finally, $N = 13.76\,\mathrm{nm}^{-3}$ is the number density of xenon atoms.

This formula is in principle even applicable for the case of small nuclear recoil velocities, meaning $v_{nr} < v_0$ (or $E_{nr} < 1\,\mathrm{MeV}$). However, it is not clear that we can assume a velocity proportional stopping power all the way down to $v_{nr} = 0$. In fact, at very low velocities, departures from velocity-proportionality have been

---

[1]Note that, for the energies we are concerned with, electrons are much faster than the recoiling nucleus.

[2]In an independent derivation, Firsov obtained the same formula with $\zeta_0 \approx 1.63$ [49].

observed [44]. Also, there are several arguments in favor of a more rapid drop of $S_{\rm e}$ for $v < v_0$. The two most important ones are *threshold effects* and *Coulomb effects*.

The argument for threshold effects essentially goes as follows: In an elastic collision between a nucleus and a free electron, only a fraction m_e/m_N of the nucleus energy can be transferred to the electron. For nuclei with energies in the keV range, the resulting electron energy is at most a few eV – so we can no longer ignore gap energies or the work function of xenon. There has been a long and intense discussion on whether such threshold effects are present or not (see for example [50]). However, many experiments and theoretical considerations report electronic excitations far below the naive threshold [51, 52].

An effect from Coulomb repulsion is expected, because at low relative velocities colliding nuclei will not penetrate the electron clouds of each other strongly. Consequently, with decreasing energy the recoiling nucleus will probe only regions of lower electron density [53]. We discuss a possible way to include this correction in appendix C, but come to the conclusion that it contradicts experimental data.

Both of these arguments fail, because they continue to exploit the point-like interaction of the nucleus with the electron. However, for low nuclear velocity the electron cloud itself rearranges during the collision (or, in a more semiclassical language, the electron makes several rotations in the combined electric field of the two colliding atoms). This effect leads to a much more complicated non-perturbative mechanism of the energy transfer to the electron. An analysis of such collisions was performed fully for the case of simple atoms [52]. The authors observe that ionization occurs even at energies far below the naive threshold. Lacking a similar calculation for xenon atoms, we will continue to use equation (4.6) even for low energies.

To conclude this section, we provide dimensionless quantities instead of $S_{\rm e}$, which are usually preferred in the literature. Therefore, we define

$$\epsilon = \frac{a}{2e^2Z^2}E \ , \tag{4.7}$$

$$\rho = N\pi a^2 x \ , \tag{4.8}$$

$$s_{\rm e} = \frac{{\rm d}\epsilon}{{\rm d}\rho} = \frac{S_{\rm e}}{2\pi e^2 a Z^2 N} = \frac{a_0\zeta_0}{a}\sqrt{\frac{8\epsilon}{e^2 a m_N}} \ , \tag{4.9}$$

where $a = 0.626a_0Z^{-1/3}$ is the Thomas-Fermi screening length. For liquid xenon, the reduced energy ϵ, which we will use throughout the rest of the chapter, can be expressed as $\epsilon = 1.05 \cdot 10^{-3}E_{\rm nr}/\,{\rm keV}$.

4.2.2 Nuclear stopping power

The second quantity needed to calculate the amount of energy lost to electronic excitations is the nuclear stopping power, corresponding to the probability for elastic scattering of two xenon atoms. To calculate the cross section, we approximate the

(a) Screening function

(b) Nuclear stopping power
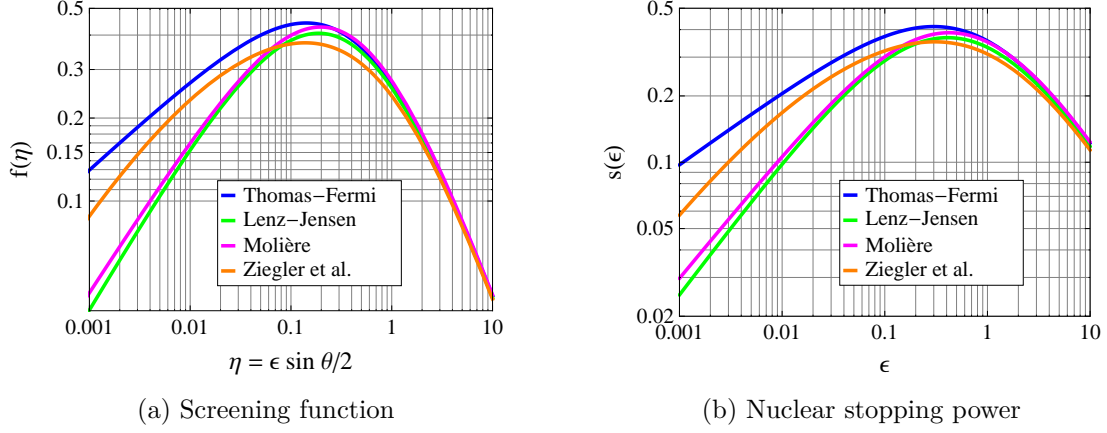
Figure 4.1: Comparison of different choices for the screening function and the corresponding nuclear stopping powers.

electron wave functions by the electron density, and ignore modifications of the electron clouds during the collision. The energy transfer in such a collision depends in general on the energy E_{nr} of the projectile and the scattering angle θ. However, it turns out that due to scaling properties all relevant functions depend only on the combined variable [54]

$$\eta = \epsilon \sin \frac{\theta}{2} \, , \tag{4.10}$$

where ϵ again denotes the reduced energy.

The differential cross section for elastic scattering can then be written as

$$\frac{\mathrm{d}\sigma}{\mathrm{d}\eta} = \pi a^2 \frac{f(\eta)}{\eta^2} \, , \tag{4.11}$$

where a is again the screening radius. The function $f(\eta)$ depends on the screening function that we adopt to describe the charge density. For a large number of screening functions, $f(\eta)$ can approximately be written as [55]

$$f(\eta) \approx \frac{\lambda \eta^{1-2m}}{\left(1 + [2\lambda \eta^{2(1-m)}]^q\right)^{1/q}} \, . \tag{4.12}$$

From $f(\eta)$ we can obtain the dimensionless nuclear stopping power $s_{\mathrm{n}}(\epsilon)$:

$$s_{\mathrm{n}}(\epsilon) = \frac{1}{\epsilon} \int_0^\epsilon \mathrm{d}\eta f(\eta) \, . \tag{4.13}$$

Both quantities, $f(\eta)$ and $s_{\mathrm{n}}(\epsilon)$ have been calculated by various authors with differing results. The large uncertainties, especially for the low energy region, are due to different approximations for the screening function. Lindhard et al. favor the Thomas-Fermi screening function corresponding to ($m = 0.333$, $q = 0.667$, $\lambda = 1.309$). However, today it is generally agreed that the Thomas-Fermi screening function overestimates the potential at large distances and therefore gives too large stopping powers at low energies [54]. One therefore often prefers the Molière or the Lenz-Jensen screening functions that show better agreement with experimental data. They correspond to the parameter choices ($m = 0.216$, $q = 0.570$, $\lambda = 2.37$) and ($m = 0.191$, $q = 0.512$, $\lambda = 2.92$), respectively. For a comparison of the different screening functions, see figure 4.1.

Ziegler et al. [56] have confronted the different screening functions with experimental data and numerical results from Hartree-Fock methods. They find yet another (so-called universal) screening function given by the following expression:[1]

$$s_{\mathrm{n}}(\epsilon_{\mathrm{Z}}) = \frac{\ln(1 + 1.1383\epsilon_{\mathrm{Z}})}{2\left[\epsilon_{\mathrm{Z}} + 0.01321\epsilon_{\mathrm{Z}}^{0.21226} + 0.19593\epsilon_{\mathrm{Z}}^{0.5}\right]} \ . \tag{4.14}$$

From this, $f(\eta)$ can be calculated using $f(x) = \frac{\mathrm{d}}{\mathrm{d}x}\left[x s_{\mathrm{n}}(x)\right]$.

While the universal screening function from Ziegler et al. appears to be the most reliable, the advantage of the simpler screening functions is that $f(\eta)$ can be approximated by a power law for very small values of η (i.e. $\eta < 10^{-4}$):

$$f(\eta) \simeq \lambda\eta^{1-2m} \ . \tag{4.15}$$

In the following we will use the universal screening function unless stated otherwise.

4.2.3 Total electronic excitation

In this section we will combine the nuclear stopping power $s_{\mathrm{n}}(\epsilon)$ from equation (4.14) and the electronic stopping power $s_{\mathrm{e}}(\epsilon)$ from equation (4.5) in order to predict what amount of the initial recoil energy is transferred to electronic excitations. We will denote the total energy in electronic excitations by $\kappa(\epsilon)$ and also define the quotient

$$\xi(\epsilon) = \frac{s_{\mathrm{e}}(\epsilon)}{s_{\mathrm{n}}(\epsilon)} \ . \tag{4.16}$$

First of all, we should discuss the general tendencies which we expect for $\kappa(\epsilon)$ and $\xi(\epsilon)$. At energies above 1 MeV, inelastic collisions will dominate because the electronic stopping power grows proportional to $\sqrt{E}$, while the nuclear stopping power decreases

---

[1]It is important to notice that Ziegler et al. use a slightly different definition for the reduced energy, because they assume a different screening length. For xenon, the conversion factor is $\epsilon_{\mathrm{Z}} = 1.068\epsilon$.
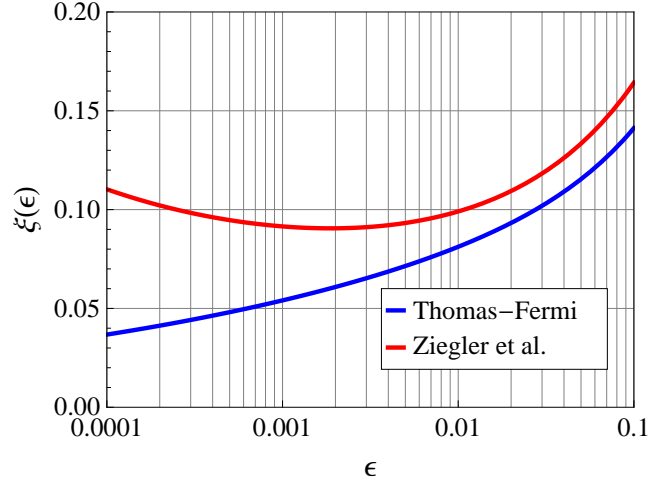
Figure 4.2: The function $\xi(\epsilon)$ for different choices of the nuclear stopping power.

after reaching its maximum around $100\,\text{keV}$ (see figure 4.1). Consequently, $\kappa(\epsilon) \approx \epsilon$ in this energy region. At energies of $10\,\text{keV}$ and below, on the other hand, the nuclear stopping power is much larger than the electronic stopping power. Consequently, we expect $\kappa(\epsilon) \ll \epsilon$ and $\xi(\epsilon) \ll 1$.

In the low energy region, a first estimate for $\kappa(\epsilon)$ is given by

$$\kappa(\epsilon) = \frac{\epsilon \cdot s_{\text{e}}(\epsilon)}{s_{\text{n}}(\epsilon) + s_{\text{e}}(\epsilon)} \approx \epsilon \cdot \xi(\epsilon) \;. \tag{4.17}$$

Making this estimate, we have included only electronic excitations produced by the primary recoiling nucleus. We expect, however, that at least some recoiling nuclei from secondary elastic collisions still have enough energy to inelastically excite other atoms. Thus, part of the energy lost in elastic collisions can still be transferred to electronic excitations.

To take this effect into account, one could try to perform numerical simulations. In [57], however, Lindhard et al. have derived an integral equation to determine $\kappa(\epsilon)$. Under the approximation that most electronic excitations occur at large impact parameter and have only small energy transfer, the authors show that for $\xi(\epsilon) \ll 1$, $\kappa(\epsilon) \propto \epsilon \cdot \xi(\epsilon)$. The constant of proportionality can be calculated analytically, if $\xi(\epsilon)$ can be described by a power law. Here, we do not want to restrict ourselves to this case, so we will keep the constant of proportionality as a free parameter, writing

$$\kappa(\epsilon) = \alpha \epsilon \xi(\epsilon) \;. \tag{4.18}$$

For $\alpha = 1$ we recover the simple estimate in equation (4.17) which is supposed to underestimate κ, so we expect $\alpha > 1$, but still of order 1, for consistency.

For Thomas-Fermi screening, we obtain from equation (4.15) that $\xi(\epsilon) \propto \epsilon^{0.17}$ and therefore $\kappa(\epsilon) \propto \epsilon^{1.17}$. In other words, Lindhard's theory predicts an increasing fraction of electronic excitations as the nuclear recoil energy increases from $1\,\mathrm{keV}$ to $100\,\mathrm{keV}$. This result has often been quoted as a possible explanation for the energy dependence of the scintillation yield in liquid xenon. However, we understand now that this result strongly depends on the choice for the screening function. As argued in section 4.2.2, choosing a Thomas-Fermi screening function will tend to overestimate the nuclear stopping power at low energies. Consequently, we must expect to underestimate $\xi(\epsilon)$. It appears much more reasonable to choose a nuclear stopping power that agrees better with experimental data. In fact, choosing the universal stopping power from Ziegler et al. which is still closest to Thomas-Fermi, already changes the behavior of $\xi(\epsilon)$ considerably (see figure 4.2). Now, $\xi(\epsilon)$ is no longer increasing monotonically, but develops a minimum around a few keV, remaining almost constant in most of the region we are interested in.

As we have seen, the uncertainties concerning the fraction of energy deposited in electronic excitations remains quite large. Although Lindhard's theory has been quoted frequently in the context of the effective scintillation yield, it appears difficult to obtain even a general tendency from this theory. We believe that some conclusions drawn from it, especially concerning the energy dependence, depend on quite weak assumptions. Moreover, we will show below, that a much more reasonable agreement with experimental data is achieved for an almost constant $\xi(\epsilon)$.

4.3 Recombination

Now that we have an estimate of the total energy in electronic excitations, we need to determine how this energy is distributed between ionization and scintillation. This distribution depends not only on the number of excited and ionized atoms produced initially, but especially on the *recombination rate*. Recombination will occur, whenever an electron and an ion produced in a nuclear recoil process approach sufficiently close. The recombination rate should be proportional to the ionization density, which in turn is roughly proportional to the electronic stopping power $s_{\mathrm{e}}(\epsilon)$. Thus, we expect a higher ionization density and a higher recombination rate, at higher recoil energies. In this section, we follow closely the Ph.D. thesis of Dahl [58].

As discussed in section 4.1, after all recoiling atoms have thermalized, we are left with a certain number of excitons, called N_{ex}, and a certain number of ionized atoms, N_{i}. We expect that a fraction r of the ionized atoms will recombine with free electrons, forming excitons that will eventually emit scintillation photons. The number of photons produced should consequently be given by

$$N_{\mathrm{ph}} = N_{\mathrm{ex}} + r \cdot N_{\mathrm{i}} = N_{\mathrm{i}}\left(r + \frac{N_{\mathrm{ex}}}{N_{\mathrm{i}}}\right)\ . \tag{4.19}$$

We assume that the fraction $N_{\mathrm{ex}}/N_{\mathrm{i}}$ is energy independent (see [59] for a discussion), although it may depend on the nature of the recoiling particle.[1] The simulations from [58] are in agreement with this assumption. For a discussion on ways to determine $N_{\mathrm{ex}}/N_{\mathrm{i}}$ experimentally, we refer to [63]. Consequently, an energy dependence can only be introduced by the recombination fraction r. For later uses, we also define the number of electrons produced,

$$N_{\mathrm{q}} = (1 - r) \cdot N_{\mathrm{i}} \ . \tag{4.20}$$

N_{ex} and N_{i} are presently unknown. However, they should both be proportional to $\kappa(\epsilon)$, which in turn was determined to be proportional to $\epsilon\xi(\epsilon)$. As we kept the constant of proportionality undetermined, we can do the same thing for $N_{\mathrm{ex}} + N_{\mathrm{i}}$, writing simply

$$N_{\mathrm{i}} + N_{\mathrm{ex}} = N_{\mathrm{i}}\left(1 + \frac{N_{\mathrm{ex}}}{N_{\mathrm{i}}}\right) = \beta\epsilon\xi(\epsilon) \ . \tag{4.21}$$

Thus, we can calculate N_{ex} and N_{i} from $\kappa(\epsilon)$ once we have determined $N_{\mathrm{ex}}/N_{\mathrm{i}}$ and β. If we also know the recombination fraction $r(\epsilon)$, we can then infer N_{ph}.

The present task is therefore to determine $N_{\mathrm{ex}}/N_{\mathrm{i}}$ and $r(\epsilon)$. Of course, it would be desirable to derive these quantities from an analytical model. In fact, various theories describing recombination exist (for a review, see [64]). The basic idea is to introduce a critical radius, called Onsager radius, which is defined by

$$\frac{e^2}{r_{\mathrm{c}}} = kT \ . \tag{4.22}$$

If the distance between electron and ion is larger than r_{c}, thermal fluctuations will prevent recombination, while for smaller distances, recombination will occur. In order to calculate the recombination rate, one needs to describe diffusion processes for electrons and ions. A calculation by Thomas and Imel [65] gives

$$\frac{N_{\mathrm{q}}}{N_{\mathrm{i}}} = 1 - r = \frac{4}{\chi N_{\mathrm{i}}} \ln\left(1 + \frac{\chi N_{\mathrm{i}}}{4}\right) \ , \tag{4.23}$$

where χ is a free parameter of the theory.[2]

In order to determine χ, Dahl has performed Monte Carlo simulations [58] of nuclear recoils at different recoil energies. For each recoil energy, the simulation

---

[1]For example, we expect $N_{\mathrm{ex}}/N_{\mathrm{i}}$ to be larger for the collision of two xenon atoms than for electron recoils, because the xenon atoms can temporarily form molecular orbitals that enhance the probability for excitations [60–62].

[2]In fact, χ can be expressed in terms of the mobility of the charge carries, μ, the drift velocity, v, and the typical size of the track, a: $\chi = 4\pi\mu/a^2 v$. However, as these parameters are unknown, we may just as well take χ as the parameter of the theory.
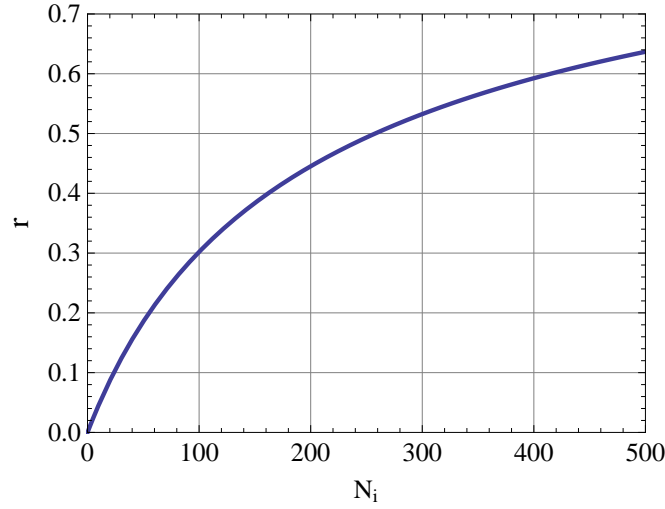
Figure 4.3: Recombination fraction r as a function of the number of ionized atoms.

provides N_q, the number of free electrons remaining after recombination. Now χ can be determined by fitting the theory to the data. Note that N_q depends not only on r but also on the total number of ionized atoms produced, so the fit will also determine the previously unknown parameter N_{ex}/N_i.

Monte Carlo simulations have been performed for different values of the electric field and show, as expected, a decrease of recombination with increasing field strength. As N_{ex}/N_i should not depend on the electric field, only χ is allowed to vary. Since we are interested in the limit of zero electric field, we take the value of χ for the lowest drift field available, which is $60\,\mathrm{V/cm}$, being much smaller than electric fields usually applied in experiments. The results are

$$\frac{N_{ex}}{N_i} \approx 0.9 \;, \tag{4.24}$$

$$\chi \approx 0.039 \;. \tag{4.25}$$

The recombination fraction r is shown in figure 4.3. As expected, it increases with the total number of produced ions corresponding to higher recoil energies.

4.4 Calculation of the relative scintillation efficiency

Having calculated the total energy in electronic excitations and the recombination fraction, we are now able to predict both the ionization and the scintillation yield. However, one free parameter still remains in our theory: the proportionality factor β, which we introduced in equation (4.21). Combining this equation with equation (4.23),

we can write

$$N_{\mathrm{q}}(\epsilon) = N_{\mathrm{i}}(\epsilon)\frac{4}{\chi N_{\mathrm{i}}(\epsilon)}\ln\left(1 + \frac{\chi N_{\mathrm{i}}(\epsilon)}{4}\right) , \qquad (4.26)$$

$$N_{\mathrm{i}}(\epsilon) = \frac{\beta\xi(\epsilon)}{1 + N_{\mathrm{ex}}/N_{\mathrm{i}}} . \qquad (4.27)$$

$N_{\mathrm{q}}(\epsilon)$ has been measured experimentally (most recently in [33]), so we can determine β from fitting equation (4.26) to the available data. Instead of $N_{\mathrm{q}}(\epsilon)$, one conventionally plots the *ionization yield*, which is defined as $Q_{\mathrm{y}}(E_{\mathrm{nr}}) = N_{\mathrm{q}}(E_{\mathrm{nr}})/E_{\mathrm{nr}}$ and measured in $\mathrm{e^-/keVnr}$. Of course, it is not possible experimentally to measure the ionization yield at zero electric field, so we must change the value for χ accordingly. We will use the experimental data taken at $E = 1\,\mathrm{kV/cm}$ and take the value $\chi = 0.03$ determined by Dahl [58] for $E = 0.88 \pm 0.04\,\mathrm{kV/cm}$. Although there is only one free parameter, a reasonable fit can be obtained setting $\beta = (1.2 \pm 0.1) \cdot 10^5$ (see the red line in figure 4.4a), which indicate that our description is sufficient.[1]

We are now in the position to predict the relative scintillation efficiency. The value of N_{ph} can be obtained directly from N_{q} because $N_{\mathrm{q}} + N_{\mathrm{ph}} = N_{\mathrm{ex}} + N_{\mathrm{i}} = \beta\epsilon\xi(\epsilon)$ and this sum is known once we have determined β. In order to obtain $\mathcal{L}_{\mathrm{eff}}$, we need to divide N_{ph} by the number of photons produced by the reference electron recoil at $122\,\mathrm{keV}$. This value can be determined from the W_{ph} value for xenon, which is the energy that an electron recoil must on average deposit in the detector to produce a scintillation photon. From [29], we take $W_{\mathrm{ph}} = 21.6\,\mathrm{eV}$ and infer that $N_{\mathrm{ph}}^{\mathrm{ref}} = 46\,\mathrm{phe/keVee}$.

Before giving our result for $\mathcal{L}_{\mathrm{eff}}$ we need to include one more process, that has been neglected so far. As mentioned in section 4.1, the number of excitons can be reduced by biexcitonic quenching (see [42, 66, 67]). The idea is that in collisions of two excited atoms, only one scintillation photon is produced. Several authors have suggested a parameterization of this process in terms of Birk's saturation law [67–69]. They introduce an energy dependent quenching factor q_{el} given by

$$q_{\mathrm{el}} = \frac{1}{1 + k \cdot s_{\mathrm{e}}(\epsilon)} , \qquad (4.28)$$

where k is called Birk's constant and has been determined by [68] to be $k = 2.015 \cdot 10^{-3}\,\mathrm{g/MeV\,cm^2} = 21.4$ in reduced units. The value suggested in [69] is smaller by about $15\,\%$. One can see from equation (4.28) that at very low recoil energies, when only few excited atoms are produced, biexcitonic collisions are rare and cease to reduce the photon yield.

---

[1]The reason why β is so large is that $\kappa(\epsilon)$ is a reduced energy.
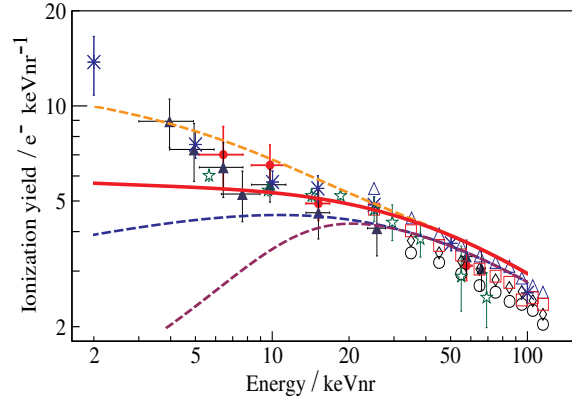
(a) The ionization yield
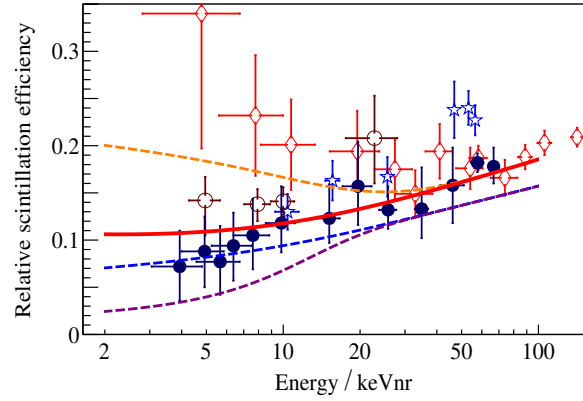
(b) The relative scintillation efficiency

Figure 4.4: Predictions for the ionization yield Q_y and the relative scintillation efficiency $\mathcal{L}_{\text{eff}}$ compared to the experimental data presented in [33] (and further references therein). The lines with different colors correspond to different choices of the function $\xi(\epsilon)$: The blue line corresponds to the original function $\xi(\epsilon)$ obtained from Lindhard's theory (nuclear stopping power based on Thomas-Fermi screening). The red line, which we consider as the best description, corresponds to our proposal to modify Lindhard's theory by using the universal nuclear stopping power from Ziegler et al. (see also figure 4.2). The purple line has been obtained by assuming a threshold effect at $5\,\text{keV}$ that reduces the electronic excitations and consequently acts like a smooth cut-off for $\xi(\epsilon)$. The ionization yield becomes clearly inconsistent with data, thus limiting the scintillation efficiency from below. For the orange line, finally, we have included an enhancement of the electronic stopping power at low energies to obtain better agreement with the ionization yield. For all plots we have used $\beta = 1.2 \cdot 10^5$. For our prediction of Q_y we assume an electric field of $E = 0.88 \pm 0.04\,\text{kV/cm}$.

Now we can write down our final result for $\mathcal{L}_{\mathrm{eff}}$:

$$\mathcal{L}_{\mathrm{eff}} = \frac{N_{\mathrm{ph}}(E_{\mathrm{nr}})}{E_{\mathrm{nr}} \cdot N_{\mathrm{ph}}^{\mathrm{ref}}} \cdot q_{\mathrm{el}}(E_{\mathrm{nr}}) \ . \tag{4.29}$$

All parameters appearing in this equation have either been measured or were fixed previously. Consequently, we can now plot $\mathcal{L}_{\mathrm{eff}}$ and compare it to available data (see the red curve in figure 4.4b). Our model predicts a flat $\mathcal{L}_{\mathrm{eff}}$ at low recoil energies, giving roughly $\mathcal{L}_{\mathrm{eff}} = 0.11$ at $E_{\mathrm{nr}} = 2\,\mathrm{keV}$. This prediction agrees well with the values measured by Aprile et al. Also, good agreement in both Q_{y} and $\mathcal{L}_{\mathrm{eff}}$ is found between our results and the results that Sorensen obtained from Monte Carlo simulations of the nuclear recoil band [34].

We would like to emphasize that the Lindhard factor, meaning $\xi(\epsilon)$, is still the dominating uncertainty of our model. In fact, we are under the impression, that this uncertainty has been often underestimated previously, as not even the general tendency (suppression or enhancement) of electronic excitations at low recoil energies is quite clear. However, the point we wish to make is that making different assumptions for the nuclear and electronic stopping powers will necessarily affect the predictions for both, ionization yield and relative scintillation efficiency.

We show different curves corresponding to different assumptions on $\xi(\epsilon)$ in figure 4.4. All choices of $\xi(\epsilon)$ give predictions for $\mathcal{L}_{\mathrm{eff}}$ that are compatible with experimental data. However, if $\xi(\epsilon)$ decreases with decreasing recoil energy (as one would expect in the presence of threshold effects or Coulomb effects), one cannot account for the increasing ionization yield that we observe experimentally.

Our central observation is therefore that any model attempting to explain the scintillation yield of liquid xenon, must at the same time explain the ionization yield. Consequently, a general suppression of electronic excitations at low recoil energies is clearly incompatible with experiments. In contrast, an energy dependent recombination fraction can clearly accommodate (and even predict) the opposing trends seen in scintillation and ionization yield. The red line in figure 4.4b is not only well motivated theoretically but also provides a good description of both ionization yield and relative scintillation efficiency.

Our results rely on the assumption that the ratio $N_{\mathrm{ex}}/N_{\mathrm{i}}$ does not vary strongly with energy. If we allow for an arbitrary energy dependence of this quantity and simultaneously vary $\xi(\epsilon)$, we could obviously fit any measurement for the ionization yield and the relative scintillation efficiency. However, from all available data, such an energy dependence is not expected. Moreover, to suppress scintillation and enhance ionization at low energies, $N_{\mathrm{ex}}/N_{\mathrm{i}}$ would have to decrease, implying that excitation becomes less likely compared to ionization. Such a behavior would most likely contradict the fact that less energy is required to excite a xenon atom than to ionize it.

(a) The total acceptance function for the XENON100 detector (not including the nuclear recoil cut).

(b) Expected exclusion limit for XENON100 and the preferred regions from DAMA and CoGeNT at 95% confidence level.
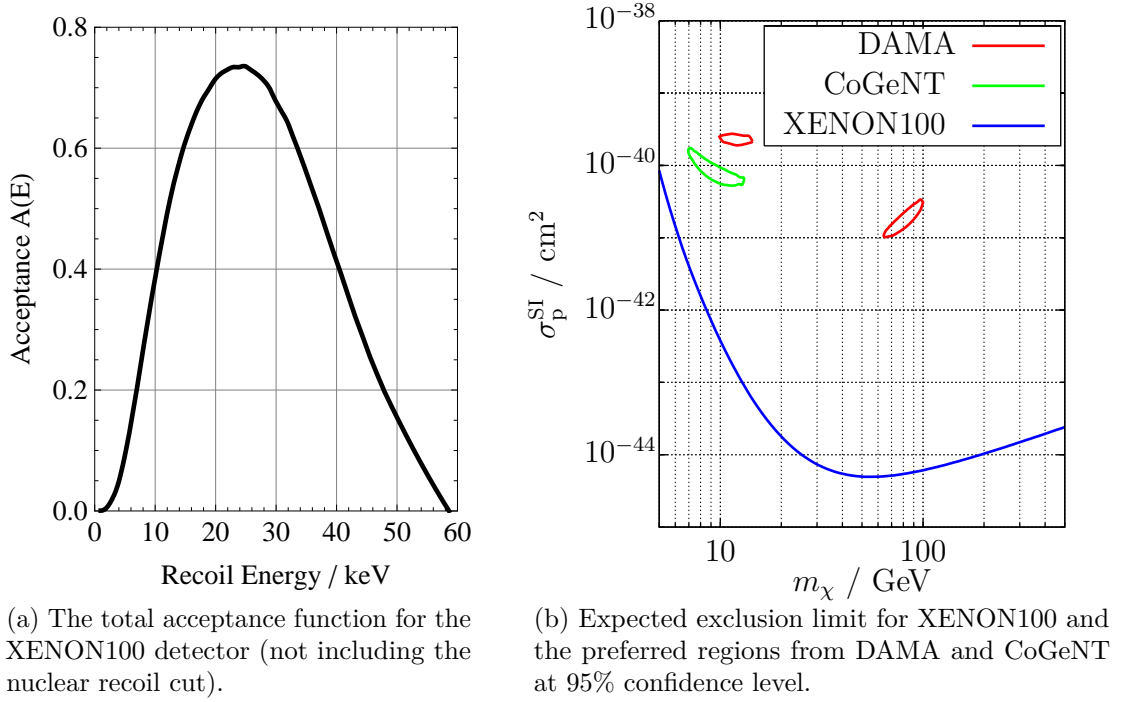
Figure 4.5: Expected performance of the XENON100 experiment. For the exclusion limits, we have assumed a runtime of 100 days. See text for further assumptions.

4.5 Summary of results

Combining our prediction for the relative scintillation efficiency (the red line in figure 4.4b) with our results from chapter 3, we can calculate the total acceptance function for XENON100. We assume $S1$ fluctuations to be described by Poisson statistics, as in equation (3.3), and include in addition the effect from variations of the light collection efficiency as discussed in chapter 3.4. We take the published values for the cut acceptance a_{cut} (see figure 3.5) and calculate the total acceptance function using equation (3.9). We assume that the acceptance of the single scatter cut is close to 100% and the nuclear recoil cut is defined in such a way that its acceptance is nearly constant in $S1$. Consequently, we include this cut by simply multiplying the total acceptance function with 0.5.

From the total acceptance function shown in figure 4.5a, we can calculate the expected exclusion limit for XENON100 for a runtime of 100 days. Our result is shown in figure 4.5b. Clearly, the upcoming data from XENON100 should be able to settle the discussion about the dark matter observations by CoGeNT and DAMA by either observing a similar signal or ruling out the preferred parameter regions.

Predicted sensitivity of future liquid xenon experiments

Having discussed in detail the sensitivity of the XENON100 detector, we will now turn to future experiments based on liquid xenon. It is clear that larger detectors will be needed in the future, either to increase the sensitivity if nothing is found at XENON100, or to confirm a possible signal with larger statistics so that one can reconstruct the spectrum and determine the dark matter mass. The possibility of upscaling is one of the greatest virtues of the dual-phase liquid xenon technology. In fact, the XENON Collaboration has already made the first step from XENON10 to XENON100 with great success and the next generation detector XENON1T is currently being planned [70]. Even larger liquid xenon detectors have been suggested [71], with a fiducial mass of up to 10 tons.

Certainly, no liquid xenon detector with 10 tons fiducial mass or more will be built within the next ten years. Nevertheless, it is worthwhile to discuss in general the advantages and difficulties connected to such an increase of the fiducial volume for two reasons. First, understanding the most challenging problems of future dark matter detectors is a valuable guideline for present research and development. And second, we can look for alternative detector designs that offer better sensitivity or suffer from less problems.

In this chapter we will denote the detector diameter and height by d and h, respectively. Unless explicitly stated otherwise, we will assume that $d = h$ to optimize the ratio of volume to surface. The position of an event is specified by the coordinates (x, y, z), where $\sqrt{x^2 + y^2} = r \leq d/2$ and $-h \leq z \leq 0$, so that $z = 0$ corresponds to the liquid surface. Unless explicitly stated otherwise, we shall assume a fiducial volume cut of $10\,\text{cm}$ as proposed for XENON1T, meaning that the fiducial volume is given by $r < d/2 - 10\,\text{cm}$ and $-h + 10\,\text{cm} \leq z \leq -10\,\text{cm}$.

In section 5.1 we will discuss why liquid xenon detectors are especially well suited for upscaling and what difficulties we must expect. The low energy threshold, which turns out to be the greatest challenge, will be the topic of section 5.2. Alternative detector designs with an especially low threshold are the topic of section 5.3. Section 5.4 is dedicated to a discussion of the background from radioactivity. Most of the results presented in this chapter are based on Monte Carlo simulations with Geant4.

Appendix D provides more information on the detector design and the materials used in the simulation and the general structure of the code.

5.1 Large liquid xenon detectors

In principle, it is not obvious that an increase of fiducial mass will improve the sensitivity of a detector. In fact, almost all current direct detection experiments observe a number of background events, and this number will rise if the size of the detector is increased. At the end of the day, the background still limits the sensitivity of the detector — so little is gained from increasing the fiducial mass. It is the great virtue of liquid xenon detectors that they observe only very little background, so the sensitivity can indeed be improved substantially by increasing the detector volume.

Increasing the size of a liquid xenon detector will bring even further advantages. First, the strong self-shielding of liquid xenon will lead to a region with extremely low background in the center of the detector. Second, the ratio of volume to surface will improve, so the fiducial volume cut will remove a much smaller fraction of the liquid xenon. Also, major sources of radioactivity (such as the photo-sensors) scale proportional to the surface, so they will contribute less to the background rate. And finally, as the size of the detector increases, neutron background will also be suppressed, because the chance decreases that a neutron scatters only once inside the active volume, so the background rejection is more efficient.

Nevertheless, there are difficulties related to increasing the detector dimensions. These difficulties are mostly connected to the magnitude and quality of the $S1$ and $S2$ signals. As we pointed out in chapter 3.1.1, the $S1$ signal limits the detector sensitivity in the low energy region. If the light yield of the detector decreases, meaning fewer photoelectrons are produced per keV energy deposition, the low energy threshold increases and the detector sensitivity is reduced. For this reason, it is unclear from the beginning whether an increase of fiducial volume will at all improve the sensitivity in the low energy region. We will address this question in section 5.2.

The $S2$ signal comes with additional problems. First of all, the electron drift length increases with the detector height. Thus, in order to keep the loss of charge under control, we must increase the electron lifetime in liquid xenon, while keeping the drift velocity constant. The first demand requires electronegative impurities to be strongly reduced, while the second demand implies that the electric field has to remain constant. Thus, the high voltage (HV) applied to the grids in the TPC must increase with the detector size.[1] This problem is a great challenges for upscaling and may in fact require a significant change of the detector design (see section 5.3). However, we assume for now that another factor of five in the HV is achievable and

---

[1]The term *grids* is used frequently in the context of liquid xenon detectors to refer to the stainless steel meshes that provide the electric field.

the known technology remains viable for larger detectors.

Still, even for constant drift velocity of the electrons there will be a longer drift time, leading to larger diffusion of the charge cloud. Consequently, we expect the position resolution of the detector to deteriorate, reducing the efficiency of the single scatter cut because two events that occur close to each other can no longer be discriminated. This problem may significantly increase the background rate, so we discuss it in detail in section 5.4. Finally, note that a longer drift time also increases the risk that two events interfere with each other, because a second event may happen before the electrons of the first event have reached the cathode.

5.2 Estimated energy thresholds

As we emphasized in chapter 3, it is extremely important for every dark matter detector to achieve a high sensitivity in the low energy region. If we assume that future liquid xenon detectors will also require $S1 \geq 4\,\mathrm{phe}$, the energy threshold is determined by the light yield L_y of the detector according to

$$E_\mathrm{nr}^\mathrm{min} = \frac{4}{L_\mathrm{y} \cdot \mathcal{L}_\mathrm{eff}} \cdot \frac{S_\mathrm{ee}}{S_\mathrm{nr}} \; . \tag{5.1}$$

The light yield is the product of the number of photons produced per keV in an electron recoil, the light collection efficiency (LCE) and the quantum efficiency (QE) of the photo-sensors. For constant drift field, the only quantity that depends on the detector geometry is LCE. Consequently, we can write

$$E_\mathrm{nr}^\mathrm{min} \propto LCE^{-1} \; , \tag{5.2}$$

where the constant of proportionality can be estimated from the XENON100 detector to be roughly $2.5\,\mathrm{keV}$.

Clearly, with increasing detector dimensions, photons will have to travel larger distances, so they are more likely to be absorbed before they hit a photo-sensor. Consequently, the light collection efficiency decreases, leading to a rise of the detector threshold and a loss of sensitivity in the low energy region. In this section we will carefully analyze the process of light collection in order to understand whether we can still gain sensitivity from increasing the fiducial volume.

5.2.1 Light collection maps

To determine the light collection efficiency for a given detector layout, Monte Carlo simulations are almost unavoidable. Simple geometrical considerations fail, because the large number of scattering and reflection processes lead to complicated photon tracks. We have performed such Monte Carlo simulations for different detector
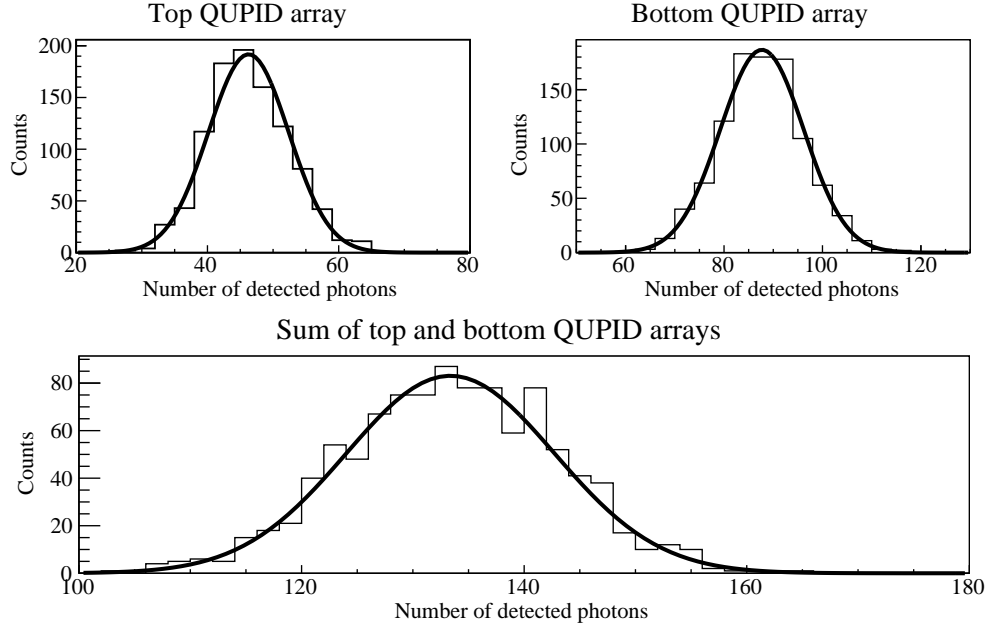
Figure 5.1: A typical result from the Monte Carlo simulation of scintillation photons. For this plot, we used a detector with $d = h = 2.0\,\mathrm{m}$. In each event, 500 scintillation photons were generated at the center of the detector.

sizes and designs (see appendix D). Ultimately we are interested in the change of light collection efficiency with increasing detector size, but first of all we need to understand the light collection properties for a given detector. Clearly, it is not trivial to quantify the light collection efficiency by a single number only, because it varies with the position of the primary event. A nuclear recoil close to the bottom QUPID[1] array will appear brighter than a recoil near the detector wall or in the center of the active volume.

For primary events[2] with a fixed position, the number of scintillation photons that reach the QUPIDs follows a Gaussian distribution (see Figure 5.1). This observation is also true for the top and the bottom QUPID array separately. Note that fluctuations of the total number of detected photons is smaller than expected from simply adding the top and bottom signal. The reason is that the two signals are anticorrelated, because the more photons reach the top QUPID array, the less photons are observed at the bottom. We define the light collection efficiency of a given position as the average number of detected photons divided by the total number of scintillation photons produced initially. With this definition, we can now study how the light collection efficiency varies over the volume of the detector.

---

[1]In all our simulations, we employ QUPIDs (see appendix D.2.1) as photo-sensors.

[2]A primary event means in this case a keV γ-ray that instantly produces a large number of
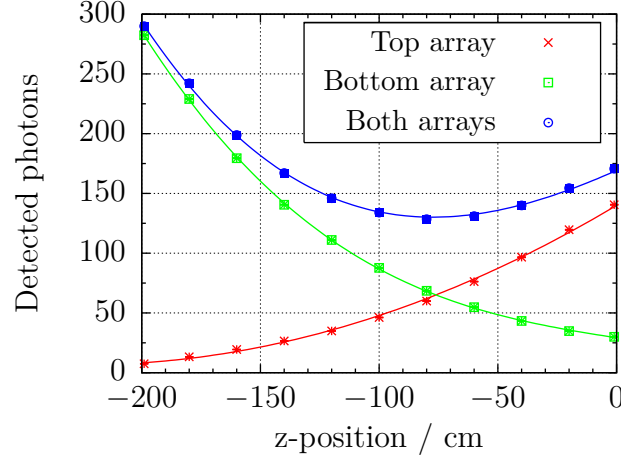
Figure 5.2: Dependence of the number of detected photons on the position of the primary event. For this plot a detector with $d = h = 2.0\,\mathrm{m}$ was used. Only the z-position was varied, keeping $x = y = 0\,\mathrm{cm}$. In each event, 500 primary scintillation photons were generated.

Let us first look at the top and bottom QUPID array separately (see figure 5.2). As expected, moving the position of the primary event towards the top of the detector will increase the light collection efficiency for the top QUPID array and reduce it for the bottom QUPID array. On average less photons reach the top QUPID array than the bottom one, because of total internal reflection on the liquid surface. As a consequence, the position with lowest total light collection efficiency lies slightly above the center of the detector. The results of extensive Monte Carlo simulations of scintillation light for varying position of the primary event in a detector with $d = h = 2.0\,\mathrm{m}$ are summarized in figure 5.3. As expected, the light collection efficiency of the detector is best near the symmetry axis $r = 0$ and close to the bottom, and worst at the outer radius slightly above the center.

5.2.2 Light collection efficiency

Certainly, a plot like the one in figure 5.3 would be the best way to describe the light collection efficiency of a given detector. However, in order to compare detectors of different sizes, we must find a simpler description. In fact, we do not need to know where the region of highest LCE lies, but only how large it is. What we therefore need is a function $m(LCE)$ giving the size (or the mass) of the detector region with a given LCE. From the light collection map in 5.3 we can guess how such a function would look: There is a large region with more or less constant and rather low light collection efficiency and small regions at the bottom and top where
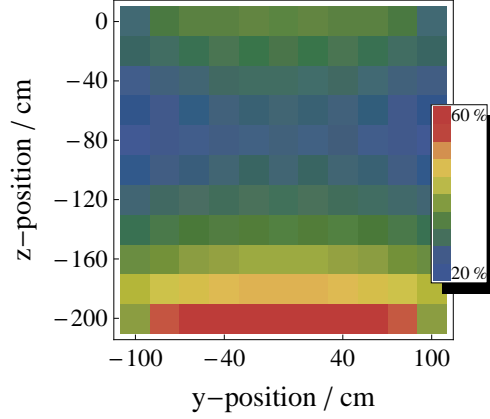
---

scintillation photons.

Figure 5.3: The light collection map of a detector with $d = h = 2.0\,\mathrm{m}$. We have set $x = 0\,\mathrm{cm}$ everywhere, but of course, the plot would look the same for $y = 0\,\mathrm{cm}$ and varying x.

the light collection efficiency reaches large values. Thus, $m(LCE)$ should have a peak at small values and a long tail towards higher values.

Indeed Monte Carlo simulations confirm our expectation (see figure 5.4). The light collection efficiency can roughly be described by the function

$$m(LCE) = N \cdot \exp\left(-\frac{a(LCE - b) + e^{-a(LCE-b)}}{2}\right) \,, \tag{5.3}$$

where a and b are parameters that we determine by a fit to the simulated data and N is an appropriate normalization factor. In the end, we are interested in the average light collection efficiency $\overline{LCE}$ and its standard deviation ΔLCE, which we can calculate from a and b.

We have determined the parameters a and b for different detector sizes and calculated the corresponding light collection efficiencies. For each detector, we include only events inside the fiducial volume. Our results are summarized in figure 5.5. We observe an exponential decrease of the mean light collection efficiency and its variation with growing detector size.[1] We obtain

$$\overline{LCE} = (0.53 \pm 0.01) \cdot \exp\left[-(0.29 \pm 0.01)\,\mathrm{m^{-1}} \cdot x\right] \,,$$
$$\Delta LCE = (0.28 \pm 0.01) \cdot \exp\left[-(0.55 \pm 0.02)\,\mathrm{m^{-1}} \cdot x\right] \,. \tag{5.4}$$

---

[1]From the data points shown in figure 5.5 one could also assume a linear decrease. However, simulating the mean light collection efficiency for much larger values of d and h we could confirm that an exponential gives the correct extrapolation.
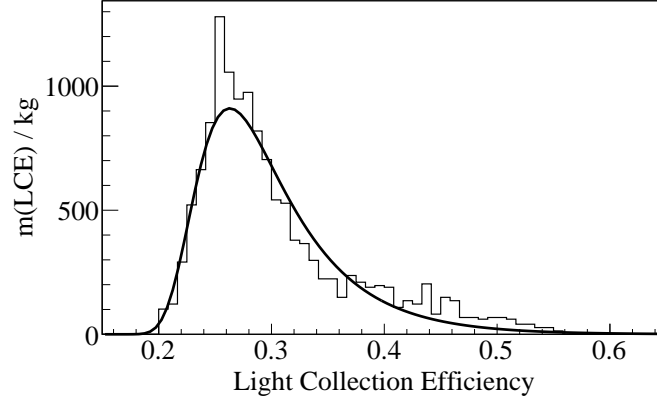
Figure 5.4: The function $m(LCE)$ for a detector with $d = h = 2.0\,\mathrm{m}$. One can clearly see that the largest contribution comes from the region with $LCE \approx 25\%$. The corresponding fit parameters are $a = 38.8 \pm 0.4$ and $b = 0.2628 \pm 0.0004$, giving $\overline{LCE} = 0.295 \pm 0.001$ and $\Delta LCE = 0.091 \pm 0.001$.

Note that $\Delta LCE/\overline{LCE}$ decreases with increasing detector size. Thus, the variation of light collection efficiency, which we already deemed irrelevant at low energies for XENON100 (see chapter 3.4), will be even less important for larger detectors.

Before we can turn to discussing the implications of our results, we should address one more issue: the absorption length of liquid xenon. Liquid xenon itself does not absorb its own scintillation light, but many impurities such as H_2O do. For the simulations above, we have used an absorption length of $\alpha = 10\,\mathrm{m}$ (which is also the value assumed in [70]). Naively, we would expect $LCE \propto \exp(-d/\alpha)$, so our results should not depend on α as long as $\alpha \gg d$. However, the actual distance traveled

Figure 5.5: Dependence of the average light collection efficiency, $\overline{LCE}$, and its standard deviation, ΔLCE, on the size of the detector. Only statistical errors are shown.

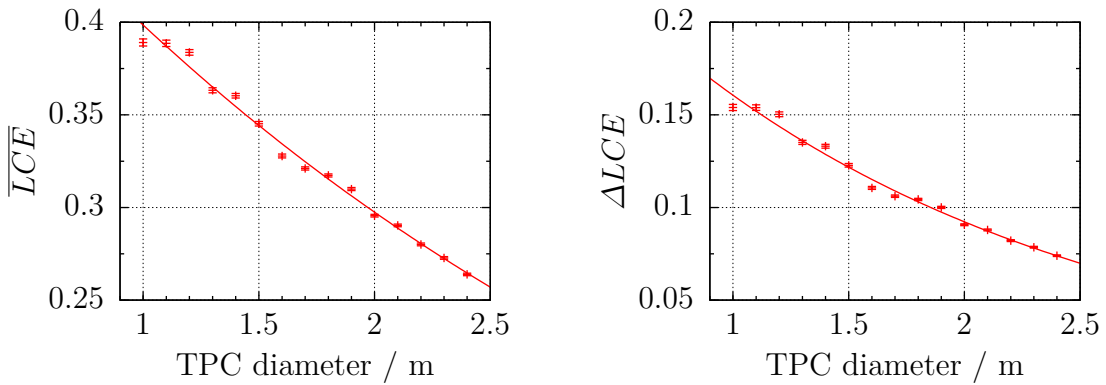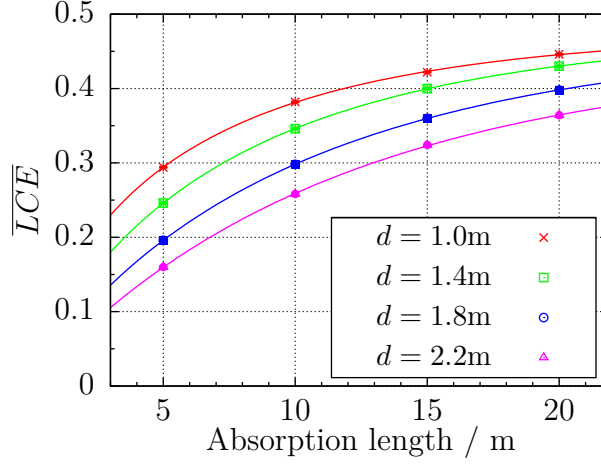Figure 5.6: Dependence of the mean light collection efficiency $\overline{LCE}$ on the absorption length for various values of the detector diameter.

by a photon can be many times larger than the detector diameter due to multiple reflection and Rayleigh scattering. As a consequence, a strong dependence of the LCE on the absorption length is observed even for $\alpha \gg d$ (see figure 5.6).

Clearly, a large absorption length is highly desirable in order to maximize the light collection efficiency. Consequently, increasing the liquid xenon purity will be another central challenges for the upscaling of the liquid xenon technology. Currently, absorption lengths of 5 m have been achieved, so assuming $\alpha > 10$ m may seem overly optimistic. In the following we will always assume $\alpha = 10$ m.[1]

5.2.3 Predicted exclusion limits

We can now calculate the low energy threshold using equation (5.4) and equation (5.1) to obtain the expected exclusion limits for future detectors of various sizes. Of course, we do not know the total acceptance function for future experiments, but we expect it to be similar to the one from XENON100. We therefore assume Poisson statistics for the $S1$ signal and take the function shown in figure 3.5 for the cut acceptance $a_{\text{cut}}(S1)$. Moreover, we assume a flat 50% nuclear recoil cut acceptance and the conservative choice of $\mathcal{L}_{\text{eff}}$. The resulting curves are shown in figure 5.7.

One can see that the sensitivity for heavy dark matter particles increases strongly with increasing detector size. In contrast, the sensitivity in the low mass region shows only very slight improvements. This result is not surprising, because as the fiducial mass is increased only the regions with low light collection efficiency grow — and these regions are essentially blind for low mass dark matter. One way to increase

---

[1]This choice is also the reason why the light collection efficiency we obtain from our simulations is much better than the light collection efficiency observed in XENON100.
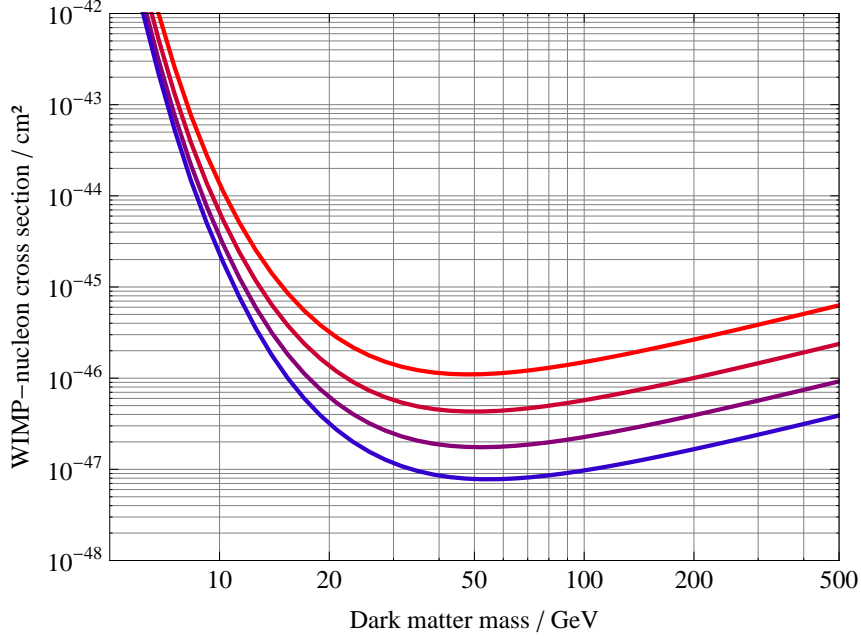
Figure 5.7: 90% exclusion limits for multi-ton liquid xenon experiments. The four curves correspond to $d =$1.0, 1.3, 1.7 and 2.2 m from red to blue. The duration of the experiment is 100 days in each case. We have used standard assumptions, meaning the conservative choice of $\mathcal{L}_{\text{eff}}$ and flat 50% acceptance for the nuclear recoil cut.

the sensitivity for low mass dark matter would be to strive for a larger absorption length of liquid xenon. Alternatively, we can think about possible design changes.

5.3 Proposed design changes

As we have seen in the previous section, an increase of the detector size does not significantly improve the sensitivity in the low energy region. Consequently, very large liquid xenon detectors are of little help in searching for low mass dark matter. For this purpose, different detector designs should be considered. Such novel designs usually rely on a larger number of photo-sensors in order to increase the light collection efficiency. In this section, we will propose and discuss two possible concepts for future liquid xenon detectors: Oblate detectors and detectors with 4π QUPID coverage.

5.3.1 Oblate detectors

Oblate detectors are detectors with $d > h$ (see figure D.1 in appendix D). Traditionally, they are disfavored because their volume to surface ratio is worse than for detectors with $d = h$ and consequently they offer a smaller fiducial mass for the same total

(a) Average light collection efficiency.

(b) Exclusion limits.

Figure 5.8: Sensitivity of multi-ton liquid xenon experiments with oblate detectors. Note that the detector height varies with the detector diameter, so that the total liquid xenon mass remains constant at 2.35 t. The 90% exclusion limits have been calculated with the same assumptions as in figure 5.7.
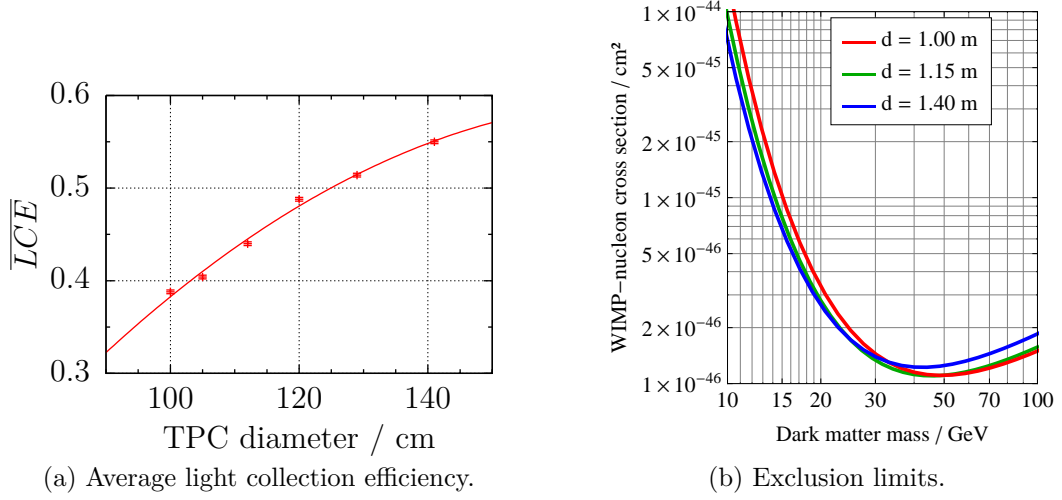
liquid xenon mass. However, in this section our aim is not to maximize the fiducial volume but instead to improve the light yield, so we dare to deviate from this tradition. We shall take a detector with $d = h = 1.0$ m (corresponding to 2.35 t total and 1.2 t fiducial mass) as the starting point and then determine how the sensitivity of the detector changes as we increase d and reduce h in such a way that the *total* liquid xenon mass remains constant.

First, we notice that the resulting loss in fiducial mass is not as bad as one might expect. In fact, even for $h = 0.5$ m and $d = 1.41$ m we get a fiducial mass of 1.04 t, a reduction of only about 15% compared to the case where $d = h$. At the same time, the number of QUPIDs grows from 242 to 508 — an increase of 110%. We can therefore reasonably hope that sensitivity is gained rather than lost as we increase d.

Using Monte Carlo simulations, we have determined the light collection efficiency of different detectors with a total liquid xenon mass of 2.35 t but a diameter varying between 1.0 m and 1.41 m (corresponding to h varying between 1.0 m and 0.5 m). Our results are presented in figure 5.8a. The light collection efficiency indeed rises significantly as the detector diameter increases and its height decreases. Figure 5.8b shows the corresponding exclusion limits. Although we have reduced the fiducial volume, the sensitivity increases in the low mass region while remaining almost constant for larger dark matter mass.

In summary, oblate detectors are an attractive option for future experiments based on liquid xenon with an emphasis on observing light dark matter. In fact a detector
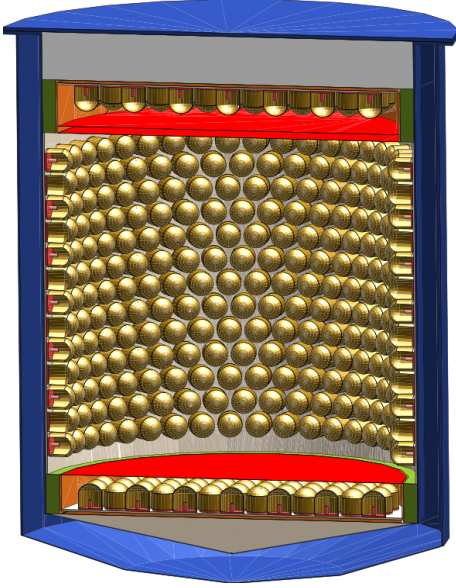
Figure 5.10: The expected 90% exclusion limit for a 4π detector and $d = h = 1.0\,\mathrm{m}$ (blue line) compared to a conventional detector of the same size (red line). We use the same assumptions as in figure 5.7, except that we take $4 \leq S1 \leq 50$ for the 4π detector.[1]

Figure 5.9: An example for a liquid xenon detector with 4π QUPID coverage.

with $d > h$ has even further advantages. The comparably small height alleviates many of the problems associated with the electron drift length (see section 5.1). Most notably, the position resolution improves and the high voltage can be reduced. On the other hand, QUPIDs are among the most expensive components of the detector, so increasing their number will significantly raise the total cost of the experiment.

5.3.2 4π QUPID coverage

A more radical (and certainly more expensive) approach would be to place QUPIDs on all detector walls. A typical design of such a detector is shown in figure 5.9. Of course, besides the enormous cost of such a detector, such a severe design change is likely to cause major technical difficulties. For example, it is presently unclear how a strong homogeneous drift field in the active volume can be maintained without affecting the performance of the QUPIDs. Another problem is data acquisition, which will be much more complicated for such a large number of channels.

Nevertheless, the light collection efficiency will indeed increase strongly. Monte Carlo simulations of detectors with 4π QUPID coverage demonstrate that a light

---

[1]If we kept the requirement $S1 \leq 20$ for the detector with 4π QUPID coverage, we would only be sensitive to recoil energies up to about $9\,\mathrm{keV}$, because of the very high light collection efficiency. Consequently, a large number of events would fall above the search region, which would artificially reduce the sensitivity of the detector for heavy dark matter particles.

collection efficiency of $\overline{LCE} = 80\%$ can be achieved for a detector with $d = h = 1.0\,\mathrm{m}$, leading to an energy threshold as low as $3\,\mathrm{keV}$. Moreover, the light collection efficiency decreases only slowly with increasing detector diameter, remaining above 70% even for $d = h = 2.4\,\mathrm{m}$. Consequently, exclusion limits in the low mass region will improve significantly, as we show in figure 5.10.

However, there is another major problem related an increasing number of QUPIDs, that we have not discussed yet. QUPIDs contribute significantly to the background level, which may limit the sensitivity of both oblate detectors and detectors with 4π QUPID coverage. To find out whether the design changes proposed in this section are feasible at all, we thus need to perform Monte Carlo simulations of the estimated background from radioactivity.

5.4 Estimated background rates

In the previous two sections, we have discussed the expected sensitivities for different future liquid xenon detectors, giving exclusion limits for various detector designs (see figures 5.7, 5.8b and 5.10). However, our results rely on the assumption that the radioactive contamination of the detector materials is low enough that we will not observe any background events. The presence of background events will inevitably reduce the sensitivity of a detector [72]. Consequently, we will explore in this section whether it is possible to maintain the great virtue of liquid xenon detectors, the extremely low background level, even for future detectors.

A distinction is made between *electron recoil background*, which results mostly from beta- and gamma-decays, and *nuclear recoil background*, which originates from neutrons produced by spontaneous fission, (α, n) reactions and muon spallation. One further distinguishes *internal background*, which comes from the detector components, *intrinsic background*, which originates from the liquid xenon and its impurities, and *external background*, which comes from environmental radioactivity and cosmic rays.

Here we will limit ourselves to the electron recoil background, because the simulation of neutrons in the low energy region is very involved and computationally extensive. This limitation implies another simplification: We do not have to worry about external background, because γ-rays from rock and concrete radioactivity can be absorbed effectively with a water shield and contribute negligibly to the background level.

In this section we will address the following questions: How does the internal electron recoil background change with the size of the detector if the radiopurity of the materials remains constant? How do the fiducial volume cut and the single scatter cut affect the background rates? What internal background rates must we expect from the alternative detector designs proposed in section 5.3? And finally, what intrinsic contributions are there to the electron recoil background and how will they ultimately limit our sensitivity?
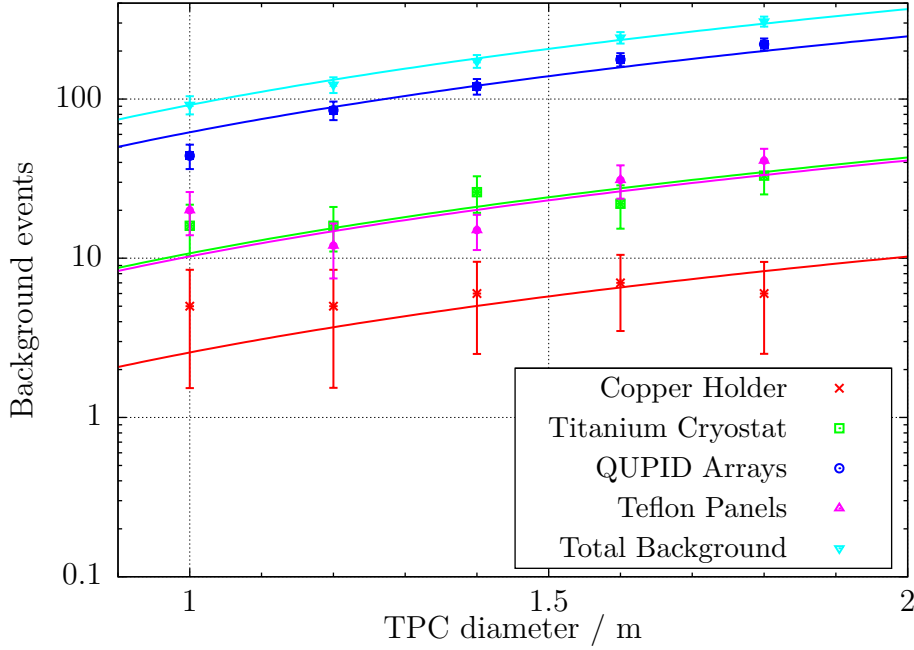
Figure 5.11: Contribution to the total background from the various detector components as a function of the detector diameter. The number of events correspond to a runtime of one year. We have applied a fiducial volume cut of $10\,\mathrm{cm}$, a single scatter cut with a position resolution $3\,\mathrm{mm}$ and considered only events in the relevant energy window $4 \leq S1 \leq 20$. The solid lines correspond to parabolas $f(d) = a \cdot d^2$.

5.4.1 Internal electron recoil background

We can use a similar Geant4 code as in sections 5.2 and 5.3 to simulate background from radioactivity. In the following, we consider only the four most relevant radioactive contaminants, namely ^{238}U, ^{232}Th, ^{40}K and ^{60}Co as well as the daughter isotopes from the decay chains of ^{238}U and ^{232}Th. For details on the assumed radioactivity of the materials and the simulation procedure, we refer to appendix D. We shall refer to the total number of events in a given period of time as the *background level* (or the total background), while using the term *background rate* for the normalized quantity in events per ton per year.

The simulation allows us to determine the number of background events that we expect inside the fiducial volume over a runtime of one year for each detector component and each contaminant separately. We present the results of our simulations in figure 5.11 for the case of a conventional detector with $d = h$. The greatest contribution to the total background comes from the QUPID arrays. The PTFE panels and the titanium cryostat contribute much less, while the contribution from the copper holders is nearly negligible. We can describe the total background level

Diameter in meters	Fiducial mass in tons	Background events	Background rate in events (ton year)$^{-1}$
1.0	1.2	92 ± 12	0.381 ± 0.012
1.2	2.4	123 ± 14	0.261 ± 0.014
1.4	4.1	173 ± 16	0.212 ± 0.013
1.6	6.5	243 ± 20	0.188 ± 0.014
1.8	9.7	307 ± 22	0.159 ± 0.018

Table 5.1: The total number of background events (see figure 5.11) and the resulting background level from Monte Carlo simulations of the internal electron recoil background in detectors of various sizes.

by a function $B(d) = (91.7 \pm 1.9 \, \text{m}^{-2}) \cdot d^2$, in agreement with our expectation that the number of background events should be proportional to the surface area of the detector.

To obtain the background rate in events (ton year)$^{-1}$ we must divide the total number of events by the exposure. Moreover, we must consider, that only a very small fraction of electron recoils will pass the nuclear recoil cut (see chapter 2.4). We assume a rejection efficiency of 99.5%, meaning that only 0.5% of the electron recoils will have a sufficiently small $S2$ signal to imitate dark matter signals. Our results are summarized in table 5.1. For comparison, note that a dark matter particle with $m_\chi = 100 \, \text{GeV}$ and $\sigma_\text{p}^\text{SI} = 10^{-47} \, \text{cm}^2$ would lead to an event rate of about 0.44 events (ton year)$^{-1}$.

First of all, we note that the background rate decreases with increasing detector dimensions. The reason is that the number of background events grows proportional to d^2, while the fiducial volume grows even more quickly than d^3, because we loose a smaller fraction of the total liquid xenon mass to the fiducial volume cut as the volume increases. Nevertheless, we would hope to gain a factor of about 8 in sensitivity as we increase the detector diameter from 1.0 m to 1.8 m, while the background rate drops only by a factor of 2.4. Thus, we must worry about the influence of the background on the detector performance. We shall return to this question in section 5.5.

5.4.2 Cut efficiencies and position resolution

The nuclear recoil cut allows to suppress background from γ-rays with high efficiency. However, we want to demonstrate in this section that we also need the single scatter cut and the fiducial volume cut to achieve an acceptable background level. In fact, we have already applied these cuts in the simulations above to obtain realistic predictions. Moreover, we have assumed that the position resolution of the detector remains constant at 3 mm for all detector sizes. In reality, it will inevitably deteriorate,
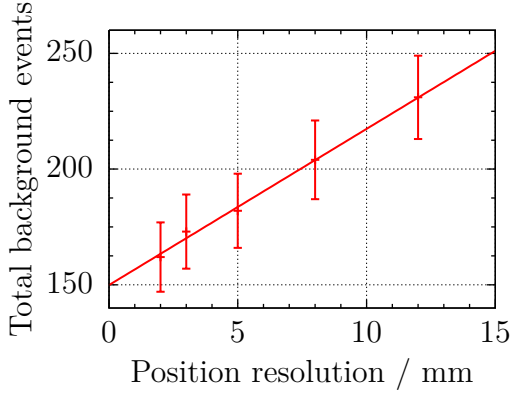
Figure 5.12: Dependence of the background level on the position resolution for a detector with $d = h = 1.4\,\text{m}$. All other cuts are the same as in figure 5.11. The solid line corresponds to a linear fit.
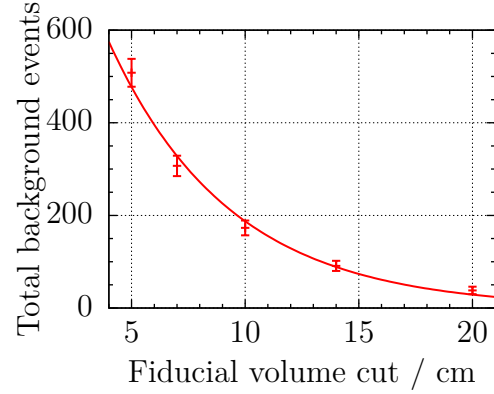
Figure 5.13: Dependence of the background level on the fiducial volume cut for a detector with $d = h = 1.4\,\text{m}$. All other cuts are the same as in figure 5.11. The solid line shows an exponential fit.

because a longer electron drift length leads to a larger diffusion of the charge cloud. A worse position resolution reduces the efficiency of the single scatter cut, because we cannot resolve all scattering events. In this section we will estimate, how the background level changes if the position resolution deteriorates and how a stronger fiducial volume cut may compensate for this change.

We observe in figure 5.12, that the background level indeed rises significantly as the position resolution deteriorates. First of all, this observation confirms that the single scatter cut is indeed very useful to suppress background from γ-rays. On the other hand, we conclude that we should not ignore the change in position resolution when simulating the background rate. For example, if we assume that the position resolution changes from $3\,\text{mm}$ for $d = 1.0\,\text{m}$ to $5\,\text{mm}$ for $d = 1.8\,\text{m}$, we must expect the background level to rise by about 8% compared to the value in table 5.1 for $d = 1.8\,\text{m}$.

The dependence of the background level on the fiducial volume cut is very strong (see figure 5.13). The reason is the strong self-shielding of liquid xenon, which ensures that all background events from γ-rays occur close to the surface of the fiducial volume (see figure 5.14). We observe that the background decreases by a factor of two for every $4\,\text{cm}$ of liquid xenon self-shielding. This observation is good news, because it implies that we can drastically reduce the background from γ-rays by applying a slightly stronger fiducial volume cut.

To compensate the increase of background with worse position resolution, we can slightly increase the fiducial volume cut. In the example from above, it would suffice to go from $10\,\text{cm}$ to $10.5\,\text{cm}$ as d increases from $1.0\,\text{m}$ to $1.8\,\text{m}$. Thus, we do not expect that a worse position resolution is a significant threat for future liquid xenon
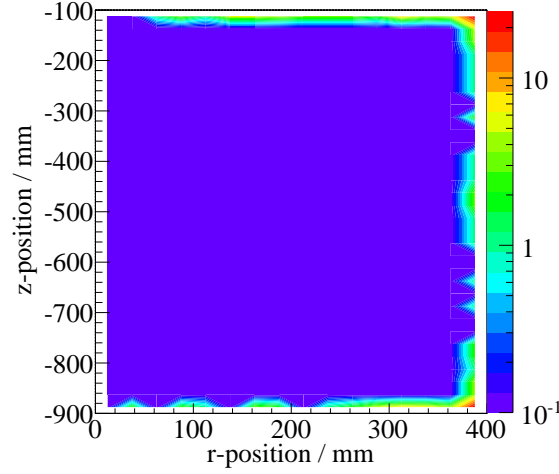
Figure 5.14: Position distribution of γ-ray background events for a detectors with $d = h = 1.0\,\mathrm{m}$. We have applied the same cuts as in figure 5.11. Because of the strong self-shielding of liquid xenon, all events occur close to the surface of the fiducial volume.

detectors. Of course, this conclusion is true only as far as electron recoil background is concerned. The single scatter cut is much more important for neutron background, which cannot be removed effectively by the fiducial volume cut. Consequently, a high position resolution is still very desirable for future liquid xenon detectors.

5.4.3 Background rates for alternative detector designs

We can make further use of Monte Carlo simulations to estimate the background level for the alternative detector designs presented in section 5.3. As we have seen in figure 5.11, QUPIDs give the dominant contribution to the background rate, so we expect that the background level should be roughly proportional to their number. Consequently, any attempts to improve the light collection efficiency of a detector by increasing the number of QUPIDs will also raise the background rate, potentially limiting the sensitivity.

A dedicated Monte Carlo simulation of an oblate detector with $d = 1.41\,\mathrm{m}$ and $h = 0.5\,\mathrm{m}$ yields a background rate of $0.88 \pm 0.08\,\mathrm{events\,(ton\,year)^{-1}}$, which is more than two times larger than the background rate for a detector with $d = h = 1.0\,\mathrm{m}$. Similarly, we obtain for a detector with $d = h = 1.0\,\mathrm{m}$ and 4π QUPID coverage a background rate of $1.04 \pm 0.10\,\mathrm{events\,(ton\,year)^{-1}}$. Clearly, we have to expect background events from electron recoils in both of these detectors, which will reduce the sensitivity. We conclude that increasing the QUPID number demands additional concessions, such as a modified fiducial volume cut.

5.4.4 Intrinsic background

Having discussed the internal background that results from the radioactive contaminants of the detector components, we now turn to the intrinsic background. Intrinsic background events are almost uniformly distributed inside the liquid xenon. Consequently, their number grows proportional to the volume rather than the surface, so the intrinsic background rate is independent of the detector dimensions. Even a stronger fiducial volume cut cannot reduce this rate. We therefore expect that the intrinsic background will become more and more important as the detector dimensions grow, and that it will ultimately limit the sensitivity of future liquid xenon detectors. In this section we will consider three possible sources of intrinsic background:[1] Beta-decay of ^{85}Kr, electron scattering of solar pp-neutrinos, and double-beta-decay of ^{136}Xe.

Krypton contamination is always present in liquid xenon and hard to remove completely. The XMASS Collaboration has achieved a purity of 1 ppt Kr/Xe [73], which is also what we assume. Krypton in turn contains the beta-decaying isotope ^{85}Kr at the level of $1.5 \cdot 10^{-11}$ [74]. In spite of these tiny quantities, the continuous beta-spectrum with end point 687 keV poses a serious intrinsic background, because ^{85}Kr has a relatively short half-life of only 10.76 years. Consequently, even a contamination of 1 ppt Kr/Xe will give an activity of 0.14 mBq per ton liquid xenon.

Solar pp-neutrinos are produced in the reaction $p + p \rightarrow d + \nu_e + e^+$ with a continuous energy spectrum that ends at $E_\nu^{\max} = 423$ keV [75]. The cross section for electron scattering of neutrinos is given by [76]

$$\frac{\mathrm{d}\sigma}{\mathrm{d}y} = \frac{G_\mathrm{F}^2 m_e E_\nu}{2\pi} \left[(2\sin^2\theta_w + 1)^2 + 4\sin^4\theta_w (1-y)^2 \right] , \qquad (5.5)$$

where $G_\mathrm{F} = 1.166 \cdot 10^{-5}\,\mathrm{GeV}^{-2}$ is Fermi's constant, $\sin^2(\theta_\mathrm{w}) = 0.231$ is the Weinberg angle [10], E_ν is the neutrino energy and $y = \frac{E_\nu - E_\nu'}{E_\nu}$ is the relative energy transfer.

If we denote the differential neutrino flux by $F(E_\nu)$, the differential event rate in the detector is given by

$$\frac{\mathrm{d}R}{\mathrm{d}E} = \rho_e \int\limits_{E_\nu^{\min}}^{E_\nu^{\max}} \frac{\mathrm{d}\sigma}{\mathrm{d}E} F(E_\nu)\, \mathrm{d}E_\nu . \qquad (5.6)$$

where $\rho_e = 3.67 \cdot 10^{25}\,\mathrm{kg}^{-1}$ is the density of quasi-free electrons in xenon and

$$E_\nu^{\min} = \frac{1}{2} \left[E + \sqrt{E(E + 2m_e)} \right] . \qquad (5.7)$$

---

[1]In principle, there will also be intrinsic background from ^{39}Ar and ^{222}Rn. However, argon can be removed effectively from liquid xenon and ^{222}Rn has a rather short half-life, so we assume that future liquid xenon experiments will not be limited by these backgrounds [70].
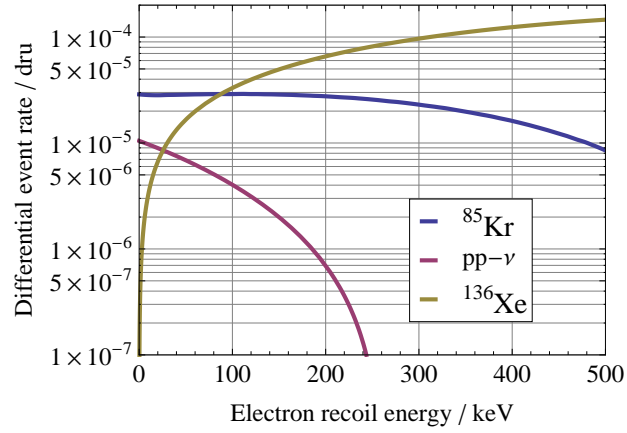
Figure 5.15: Contributions to the intrinsic background in liquid xenon detectors. We have assumed a krypton contamination of $1\,\mathrm{ppt}$ and a $^{136}\mathrm{Xe}$ half-life of $10^{22}\mathrm{yr}$.

Finally, natural xenon contains 8.9% of $^{136}\mathrm{Xe}$ which can undergo double-beta-decay. Although the half-life has not yet been measured, it is expected to be close to its current experimental limit of $\tau_{1/2} = 10^{22}\mathrm{yr}$. We show the spectra of all three contributions in figure 5.15.

In the dark matter search region $4 \leq S1 \leq 20$, corresponding to roughly $2\,\mathrm{keVee} \leq E \leq 11\,\mathrm{keVee}$, the energy spectra of $^{85}\mathrm{Kr}$ and solar pp-neutrinos are almost constant, while the contribution from $^{136}\mathrm{Xe}$ can be neglected. At these energies, we expect a differential event rate of 10^{-5} events $(\mathrm{kg\,day})^{-1}$ from solar pp-neutrinos and $3 \cdot 10^{-5}$ events $(\mathrm{kg\,day})^{-1}$ from $^{85}\mathrm{Kr}$. These values translate to a background rate of 0.018 events $(\mathrm{ton\,year})^{-1}$ for solar pp-neutrinos and 0.055 events $(\mathrm{ton\,year})^{-1}$ for $^{85}\mathrm{Kr}$, where we have again assumed a discrimination power of 99.5%.

From these observations we conclude that the intrinsic background is not negligible. In fact, it becomes more and more important as we increase the detector dimensions and is of the same magnitude as the internal background from γ-rays for $d \geq 1.8\,\mathrm{m}$. What is worse, it is essentially irreducible. Even if we imagine that krypton can be removed to the level of $0.2\,\mathrm{ppt}$, the solar neutrino background will remain. Unless a better discrimination power between electron recoils and nuclear recoils can be achieved, this background will ultimately limit the sensitivity that liquid xenon detectors can achieve.[1]

---

[1]Note that nuclear recoils of solar neutrinos as discussed in [77] do not limit the sensitivity of future liquid xenon detectors, because the maximum recoil energy is well below the threshold.

5.5 Summary of results

To conclude this chapter, we can use the background rates that we obtained in section 5.4 (see table 5.1) to re-examine the exclusion limits from section 5.2 (see figure 5.7). We obtained that a detector with $d = 1\,\mathrm{m}$ (approximately 1 t fiducial mass) can achieve a sensitivity of $\sigma_\mathrm{p}^\mathrm{SI} \approx 3 \cdot 10^{-47}\,\mathrm{cm}^2$ for $m_\chi = 50\,\mathrm{GeV}$ in a runtime of one year. From the Monte Carlo simulations of radioactive contaminations we conclude that we expect less than 0.5 events from internal electron recoil background in such an experiment, if a rejection efficiency of the nuclear recoil cut of 99.5% can be achieved.[1] The background from intrinsic sources is even smaller, namely below 0.1 events, if ^{85}Kr can be removed to the 1 ppt level. Consequently, electron recoil background should not limit the sensitivity of a ton-sized experiment like XENON1T.

For a detector with $d = 1.8\,\mathrm{m}$ (fiducial mass of about 10 t), we would expect a maximum sensitivity of $\sigma_\mathrm{p}^\mathrm{SI} \approx 3 \cdot 10^{-48}\,\mathrm{cm}^2$. However, such an experiment would observe more than 1.5 events from internal electron recoil background, unless the fiducial volume cut is increased. In addition, more than 0.5 events are expected from intrinsic background, which cannot be removed by the fiducial volume cut.[2] Therefore, the detector will most likely observe a number of background events.[3] Clearly, unless the radiopurity of the detector components can be improved significantly, the background will eventually limit the sensitivity of future liquid xenon detectors.

In summary, we believe that oblate detectors offer an attractive option to increase the detector sensitivity in the low energy region while avoiding many of the problems that come with upscaling. A detector with $d = 1.41\,\mathrm{m}$ and $h = 0.5\,\mathrm{m}$ (1.04 t fiducial mass) offers a similar sensitivity for dark matter particles with $m_\chi < 10\,\mathrm{GeV}$ as a conventional detector with 10 t fiducial mass, while having an acceptable background level of less than 0.9 events per year from electron recoils. Detectors with 4π QUPID coverage, on the other hand, pose great technical challenges and increase the cost of the experiment significantly but certainly offer the best sensitivity for the entire parameter region — if the background rate is under control. Another option would be to aim for a significant increase of the liquid xenon absorption length, which could have similar benefits for the light collection efficiency while avoiding many of the problems that come with a large number of QUPIDs.

---

[1]Note that presently achieved rejection efficiencies are about 99%, so this assumption is in fact rather optimistic.

[2]Moreover, in contrast to γ-rays, electrons from beta-decay always give only one $S2$ signal, so the single scatter cut does not reduce the intrinsic background either.

[3]We still have neglected the background from neutron scattering which is expected to become dominant for large liquid xenon detectors [70].

Analysis of matrix elements for fermionic dark matter

So far, we have calculated all exclusion limits using the standard cross section for spin-independent interaction between dark matter and nucleons from equation (2.9). In this chapter, we will discuss more complicated interactions. In general, the cross sections can depend on the spin of the dark matter particle, $\boldsymbol{s}_\chi$, the spin of the nucleus, $\boldsymbol{s}_N$, and the initial and final momentum of the nucleus, $\boldsymbol{p}$ and $\boldsymbol{p}'$.[1] Instead of $\boldsymbol{p}$ and $\boldsymbol{p}'$, it is convenient to use the momentum transfer $\boldsymbol{q} = \boldsymbol{p}' - \boldsymbol{p}$ and the momentum sum $\boldsymbol{P} = \boldsymbol{p} + \boldsymbol{p}' = 2\boldsymbol{p} + \boldsymbol{q}$.

In principle, the cross section can be an arbitrary scalar function of $\boldsymbol{P}$ and $\boldsymbol{q}$. However, the central point of this chapter is that for dimensional reasons only $|\boldsymbol{q}|/m$ and $|\boldsymbol{P}|/m$ can appear in the cross section, where m is a mass scale. The only available mass scales are m_χ and m_N, which are both much larger than $1\,\mathrm{GeV}$. The momenta $|\boldsymbol{q}|$ and $|\boldsymbol{P}|$, on the other hand, are at most about $100\,\mathrm{MeV}$. Consequently, scattering with momentum dependent cross sections will be suppressed. To understand this momentum dependence, we can expand the cross sections in powers of $|\boldsymbol{q}|/m$ and $|\boldsymbol{P}|/m$ and consider only zeroth and first order.[2]

In this chapter, we would like to look systematically at possible interactions between dark matter and nuclei. For the present discussion, we limit ourselves to the case of fermionic dark matter with spin $1/2$, but many of our results can be generalized to other models. Also, we assume for simplicity that the nucleus is also a spin-$1/2$ fermion. Other cases can be obtained in complete analogy by replacing the Pauli matrices with the correct representation of the spin algebra.

To illustrate the central concepts of this chapter, we begin with the derivation of familiar cross sections, namely for standard spin-independent (SI) interaction in section 6.1, and for standard spin-dependent (SD) interaction in section 6.2. We show that the calculation of cross sections can essentially be split into two parts: The matching of quark operators to nucleus operators and the calculation of the

---

[1]In the laboratory frame, we would have $\boldsymbol{p} = 0$, but we prefer to work in the center-of-mass frame, where the initial momentum of the nucleus, $\boldsymbol{p}$, and the initial momentum of the dark matter particle, $\tilde{\boldsymbol{p}}$, are related by $\boldsymbol{p} = -\tilde{\boldsymbol{p}} = -\mu\boldsymbol{v}$ with the reduced mass μ.

[2]There are a few examples where inverse powers of $|\boldsymbol{q}|/m$ can appear, but we will only discuss them marginally.

non-relativistic limit for the nucleus operators. We will discuss the latter problem in sections 6.3 and 6.4, giving a generalization of the previous calculations. In section 6.5, we turn to the problem of matching and form factors. In the end, we will have all the ingredients needed to calculate cross sections for a large number of possible models.

6.1 Spin-independent interactions

The simplest model that leads to spin-independent interaction is the exchange of a heavy scalar boson ϕ, for example the Higgs boson, between quarks and dark matter. The couplings of quarks and dark matter to this heavy scalar are given by Yukawa terms:

$$\mathcal{L} \supset \alpha\phi\overline{\chi}\chi + \beta_q\phi\overline{q}q + \text{h.c.} , \tag{6.1}$$

where the sum over all quarks is implied. In general, the second term should be $\beta_{ij}\overline{q}_i q_j$, but we assume that β is flavor diagonal. If the mass of the scalar is large compared to the momentum transfer, meaning $m_\phi \gg 100\,\text{MeV}$, we can integrate out the exchange particle.[1] We then obtain the *effective four-fermion interaction*

$$\mathcal{L} \supset g_q\overline{\chi}\chi\overline{q}q , \tag{6.2}$$

where g_q is proportional to $\alpha\beta_q/m_\phi^2$.

The interaction between dark matter particles and quarks induces an interaction between dark matter particles and nuclei that we expect to be of a similar form, namely

$$\mathcal{M} \propto \overline{\chi}\chi\overline{N}N , \tag{6.3}$$

where N is the nucleus field. However, the matching of quark operators to nucleus operators turns out to be rather complicated, so we must be careful to take only one step at a time. In the end, we will in fact obtain a somewhat more difficult expression for the dark matter-nucleus interaction.

The first step is to go from quarks to nucleons and calculate the interaction between dark matter and individual protons and neutrons. For this purpose, we need to know the contribution of the different quarks to the nucleon. Consequently, we must evaluate $\langle p|\overline{q}q|p\rangle$ and $\langle n|\overline{q}q|n\rangle$, where p and n denote proton and neutron, respectively. We define the coupling constants

$$f_{T_q}^{(p)} = \frac{\langle p|m_q\overline{q}q|p\rangle}{m_p}, \qquad\qquad f_{T_q}^{(n)} = \frac{\langle n|m_q\overline{q}q|n\rangle}{m_n} . \tag{6.4}$$

---

[1]We refer to [78] for a discussion of potential difficulties that can arise during this step.

Note that $f^{(p)}$ and $f^{(n)}$ are related by isospin symmetry, for example $f_{T_u}^{(p)} = f_{T_d}^{(n)}$. The operator $\bar{q}q$ is directly connected to the nucleon mass and the so-called pion-nucleon sigma term. Therefore, one can determine the parameters $f^{(p)}$ and $f^{(n)}$ with good accuracy from both measurement and calculation. The coupling constant for dark matter to protons is then given by [12]

$$f_p = \sum_{q=u,d,s} \frac{m_p}{m_q} g_q f_{T_q}^{(p)} + \frac{2}{27} \left(1 - \sum_{q=u,d,s} f_{T_q}^{(p)} \right) \sum_{q=c,b,t} g_q \frac{m_p}{m_q} \,, \tag{6.5}$$

and similarly for f_n. Using these coefficients, we can write the matrix element as

$$\mathcal{M} = f_p \bar{\chi}\chi\bar{p}p + f_n \bar{\chi}\chi\bar{n}n \,. \tag{6.6}$$

In principle, there should moreover be form factors for proton and neutron that depend on the momentum transfer $\boldsymbol{q}$. However, for a momentum transfer $|\boldsymbol{q}| < 100\,\mathrm{MeV}$, it is a good approximation to set the nucleon form factors equal to unity.

The next step is to obtain a nucleus operator from the nucleon operators. In our case, this step is very simple, because the operators $\bar{p}p$ and $\bar{n}n$ simply count protons and neutrons, respectively. We therefore get for the nucleus field N

$$\mathcal{M} = (Zf_p + (A - Z)f_n)\,\bar{\chi}\chi\overline{N}NF(\boldsymbol{q}^2) \,. \tag{6.7}$$

The form factor for the entire nucleus cannot be neglected. In the present case, it essentially corresponds to the Fourier transformation of its mass density. An explicit parameterization of $F(\boldsymbol{q}^2)$ is given in equation (2.10).

Moreover, one might be worried that equation (6.7) is not complete and that additional operators like $\overline{N}\gamma^\mu N q_\mu$ appear in the matching process. However, we will show in section 6.5 that the operator in equation (6.7) is indeed the only one that can occur.

We have now reached the final step of the calculation, which is to take the non-relativistic limit of the expression in equation (6.7). To do so, we write the fermion fields N and χ in terms of two-component spinors N_h and χ_h (see appendix A):[1]

$$N(p) = \frac{1}{\sqrt{2m_N}} \begin{pmatrix} \sqrt{p \cdot \sigma}N_h \\ \sqrt{p \cdot \overline{\sigma}}N_h \end{pmatrix}; \qquad \chi(\tilde{p}) = \frac{1}{\sqrt{2m_\chi}} \begin{pmatrix} \sqrt{\tilde{p} \cdot \sigma}\chi_h \\ \sqrt{\tilde{p} \cdot \overline{\sigma}}\chi_h \end{pmatrix} \,. \tag{6.8}$$

In the non-relativistic limit, we can approximate $E \approx m_N$ and $\tilde{E} \approx m_\chi$ and use the expansion [79]

$$\sqrt{p \cdot \sigma} \approx \sqrt{m_N - \boldsymbol{p} \cdot \boldsymbol{\sigma}} \approx \sqrt{m_N} \left(1 - \frac{\boldsymbol{p} \cdot \boldsymbol{\sigma}}{2m_N} \right) \,. \tag{6.9}$$

---

[1]The label h stands for *heavy field*.

We then get

$$
\overline{N}(p')N(p) = N^\dagger(p')\gamma^0 N(p)
$$

$$
= \frac{1}{2m_N} \left(N_h^\dagger \sqrt{p' \cdot \sigma}, \quad N_h^\dagger \sqrt{p' \cdot \overline{\sigma}} \right) \begin{pmatrix} 0 & \mathbb{1} \\ \mathbb{1} & 0 \end{pmatrix} \begin{pmatrix} \sqrt{p \cdot \sigma} N_h \\ \sqrt{p \cdot \overline{\sigma}} N_h \end{pmatrix}
$$

$$
= \frac{1}{2m_N} N_h^\dagger \left(\sqrt{p' \cdot \sigma} \sqrt{p \cdot \overline{\sigma}} + \sqrt{p' \cdot \overline{\sigma}} \sqrt{p \cdot \sigma} \right) N_h \ . \tag{6.10}
$$

Using the expansion from equation (6.9), we get $\left(\sqrt{p' \cdot \sigma} \sqrt{p \cdot \overline{\sigma}} + \sqrt{p' \cdot \overline{\sigma}} \sqrt{p \cdot \sigma} \right) = 2m_N + \mathcal{O}(p^2/m_N^2)$ and consequently $\overline{N}N = N_h^\dagger N_h$, as expected. Using $N_h^\dagger N_h = 1$, we get the non-relativistic limit,

$$
\frac{\mathrm{d}\sigma}{\mathrm{d}\boldsymbol{q}^2} \propto (Z f_p + (A - Z) f_n)^2 \, F^2(\boldsymbol{q}^2) \ . \tag{6.11}
$$

The implications of this result for dark matter direct detection have already been discussed in chapter 2.1. Note that the cross section has a very simple form because the momentum transfer $\boldsymbol{q}$ appears only in the form factor.

To illustrate some of the problems that we want to discuss in this chapter, let us consider a slight modification of the model above. Assume a mediator boson with mass $m_\phi \approx |\boldsymbol{q}|$ or even lighter. In this case, we can no longer integrate out the mediator, so we would have to multiply our result in equation (6.11) with an overall factor of $m_\phi^4/(m_\phi^2 + \boldsymbol{q}^2)^2$. This modification would introduce an additional non-trivial momentum dependence and consequently change the differential event rates. Experimentally, we would observe an enhancement of nuclear recoils with small momentum transfer and a suppression of nuclear recoils with larger momentum transfer. Consequently, much larger dark matter masses would suddenly be compatible with DAMA and CoGeNT, but at the same time, the entire allowed parameter region is excluded by XENON and CDMS (see figure 6.1a).

6.2 Spin-dependent interactions

For the model above, the cross section does not depend on the spin of the particles. The reason is that the spin-operator $\boldsymbol{\sigma}$ only appears dotted into $\boldsymbol{p}/m$, which is suppressed in the non-relativistic limit compared to the spin-independent contribution. However, other models exist where such a suppression is not present. For example, consider an interaction mediated by a vector boson that couples only to the axial currents

$$
\mathcal{L} \supset \alpha V^\mu \overline{\chi} \gamma_\mu \gamma^5 \chi + \beta_q V^\mu \overline{q} \gamma_\mu \gamma^5 q + \mathrm{h.c.} \tag{6.12}
$$

(a) Very light mediator boson leading to $\mathcal{M} \propto \boldsymbol{q}_{\mathrm{ref}}^4/\boldsymbol{q}^4$ with $|\boldsymbol{q}_{\mathrm{ref}}| = 100\,\mathrm{MeV}$.

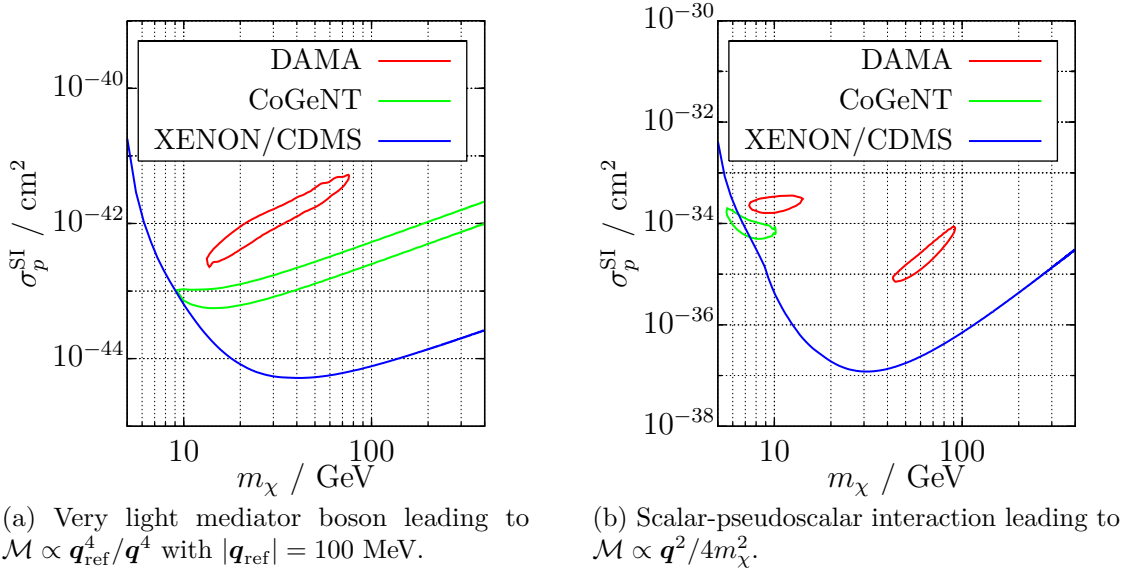(b) Scalar-pseudoscalar interaction leading to $\mathcal{M} \propto \boldsymbol{q}^2/4m_\chi^2$.

Figure 6.1: Allowed regions and exclusion limits for different models that lead to a q-dependence of the scattering cross section (compare to figure 2.2). All regions correspond to 3σ confidence level.

Again, if $m_V \gg 100\,\mathrm{MeV}$, we can integrate out the mediator to obtain an effective interaction

$$\mathcal{L} \supset g_q \overline{\chi}\gamma^\mu\gamma^5\chi\overline{q}\gamma_\mu\gamma^5 q \ . \tag{6.13}$$

In the following, we will show that this model leads to spin-dependent interactions. Again, the first step is to replace the quark fields with nucleon fields. However, in the present case there arises an additional problem, because the matrix element diverges for $q^2 = m_\pi^2$, where m_π is the pion mass [80].[1] Implementing the hypothesis of Partially Conserved Axial Currents (PCAC), we can write

$$\langle p|\overline{q}\gamma_\mu\gamma^5 q|p\rangle = \Delta_q^{(p)}\overline{p}\left(\gamma_\mu\gamma^5 + \frac{2m_p}{m_\pi^2 - q^2}q_\mu\gamma^5\right)p \ , \tag{6.14}$$

where $\Delta_q^{(p)}$ represents the fraction of the nucleon spin that is carried by quarks of type q:

$$\langle p|\overline{q}\gamma_\mu\gamma^5 q|p\rangle = 2s_\mu^{(p)}\Delta_q^{(p)} \ . \tag{6.15}$$

---

[1]Note, however, that for all collisions that we consider, $q^2 \approx -\boldsymbol{q}^2 < 0$, so we need not be worried about this divergence.

Again, the expression for neutrons is analogous. Here we see for the first time, that matching fundamental fields to those of composite particles can introduce additional operators with more complicated q-dependence.

The step from nucleons to nuclei can be performed without additional contributions at leading order [81].[1] Of course, form factors, which describe the distribution of nucleon spins inside the nucleus, will be introduced, but we will neglect them for the moment and only include them later on. To match nucleon operators to nucleus operators, we define

$$a_p = \sum_{q=u,d,s} \frac{g_q}{\sqrt{2}G_{\mathrm{F}}} \Delta_q^{(p)} \, , \qquad\qquad a_n = \sum_{q=u,d,s} \frac{g_q}{\sqrt{2}G_{\mathrm{F}}} \Delta_q^{(n)} \, , \qquad (6.16)$$

and introduce $\Lambda = \left(a_p \langle s_p \rangle + a_n \langle s_n \rangle\right)/J$, where J is the total angular momentum of the nucleus and $\langle s_{p,n} \rangle$ denote the expectation value of the spin content of proton and neutron in the nucleus, respectively. We can then write

$$\mathcal{M} \propto \Lambda \overline{\chi} \gamma^\mu \gamma^5 \chi \overline{N} \left(\gamma_\mu \gamma^5 + \frac{2m_p}{m_\pi^2 - q^2} q_\mu \gamma^5 \right) N \, . \qquad (6.17)$$

Now, we need to take the non-relativistic limit of the expressions $\overline{N}\gamma^5 N$ and $\overline{N}\gamma_\mu \gamma^5 N$. For the first one, we get

$$\overline{N}(p')\gamma^5 N(p) = N^\dagger(p')\gamma^0 \gamma^5 N(p)$$

$$= \frac{1}{2m_N} \left(N_h^\dagger \sqrt{p'\cdot\sigma}, \;\; N_h^\dagger \sqrt{p'\cdot\overline{\sigma}} \right) \begin{pmatrix} 0 & \mathbb{1} \\ \mathbb{1} & 0 \end{pmatrix} \begin{pmatrix} -\mathbb{1} & 0 \\ 0 & \mathbb{1} \end{pmatrix} \begin{pmatrix} \sqrt{p\cdot\sigma}\,N_h \\ \sqrt{p\cdot\overline{\sigma}}\,N_h \end{pmatrix}$$

$$= \frac{1}{2m_N} N_h^\dagger \left(\sqrt{p'\cdot\sigma}\sqrt{p\cdot\overline{\sigma}} - \sqrt{p'\cdot\overline{\sigma}}\sqrt{p\cdot\sigma} \right) N_h \, . \qquad (6.18)$$

Here, the leading-order term cancels and we get $\left(\sqrt{p'\cdot\sigma}\sqrt{p\cdot\overline{\sigma}} - \sqrt{p'\cdot\overline{\sigma}}\sqrt{p\cdot\sigma} \right) = (\boldsymbol{p} - \boldsymbol{p}') \cdot \boldsymbol{\sigma} = -\boldsymbol{q}\cdot\boldsymbol{\sigma}$, so that

$$\overline{N}(p')\gamma^5 N(p) = -\frac{\boldsymbol{q}}{2m_N} \cdot N_h^\dagger \boldsymbol{\sigma} N_h \, . \qquad (6.19)$$

For the expression $\overline{N}\gamma_\mu \gamma^5 N$ we get after a similar calculation

$$\overline{N}(p')\gamma_\mu \gamma^5 N(p) = \begin{cases} \frac{\boldsymbol{P}}{2m_N} \cdot N_h^\dagger \boldsymbol{\sigma} N_h & \text{for } \mu = 0 \\ N_h^\dagger \sigma_i N_h & \text{for } \mu = i \end{cases} \, , \qquad (6.20)$$

where $\boldsymbol{P} = \boldsymbol{p} + \boldsymbol{p}'$. The operator $N_h^\dagger \boldsymbol{\sigma} N_h$, which we obtain in both cases, measures

---

[1]However, there will be a suppressed operator that corresponds to the electric dipole moment of the nucleus (see section 6.5).

the spin of the nucleus: $N_h^\dagger \boldsymbol{\sigma} N_h \propto \boldsymbol{s}_N$.

Finally, we need to contract the non-relativistic expression for the nucleus fields with the corresponding one for the dark matter particle, which of course has the same form as equation (6.20), but with $\tilde{p}$ instead of p.[1] Note that the time components of all operators are suppressed by powers of p/m.[2] Consequently, we only need to multiply the spatial components and obtain

$$\overline{\chi}\gamma^\mu\gamma^5\chi\overline{N}\left(\gamma_\mu\gamma^5 + \frac{2m_p}{m_\pi^2 - q^2}q_\mu\gamma^5\right)N \propto -\boldsymbol{s}_\chi\cdot\boldsymbol{s}_N - \frac{m_p}{m_\pi^2 - q^2}\frac{(\boldsymbol{s}_\chi\cdot\boldsymbol{q})(\boldsymbol{s}_N\cdot\boldsymbol{q})}{m_N} \ . \quad (6.21)$$

To get the differential cross section, we must take the spin average of $|\mathcal{M}|^2$. Doing so gives us a factor of $\boldsymbol{q}^2$ from both $(\boldsymbol{s}_\chi\cdot\boldsymbol{q})$ and $(\boldsymbol{s}_N\cdot\boldsymbol{q})$. For example, using $\frac{1}{2}\sum_{\text{spins}}\chi_h\chi_h^\dagger = \mathbb{1}$ we get

$$\frac{1}{2}\sum_{\text{spins}}|\chi_h^\dagger\sigma_i\chi_h q^i|^2 = \frac{1}{2}\sum_{\text{spins}}(\chi_h^\dagger\sigma_i\chi_h q^i)(\chi_h^\dagger\sigma_j\chi_h q^j) \qquad (6.22)$$

$$= \frac{1}{2}\sum_{\text{spins}}\text{tr}(\chi_h\chi_h^\dagger\sigma_i\chi_h\chi_h^\dagger\sigma_j)q^i q^j \qquad (6.23)$$

$$= \frac{1}{2}\text{tr}(\sigma_i\sigma_j)q^i q^j = \delta_{ij}q^i q^j = \boldsymbol{q}^2 \ . \qquad (6.24)$$

We obtain

$$\frac{1}{4}\sum_{\text{spins}}|\mathcal{M}|^2 \propto \Lambda^2\left[3 + 2\frac{m_p}{m_\pi^2 - q^2}\frac{\boldsymbol{q}^2}{m_N} + \left(\frac{m_p}{m_\pi^2 - q^2}\frac{\boldsymbol{q}^2}{m_N}\right)^2\right] \equiv \Lambda^2 S(|\boldsymbol{q}|) \ . \quad (6.25)$$

In the impulse approximation, we then get [82]

$$\frac{\mathrm{d}\sigma}{\mathrm{d}\boldsymbol{q}^2} = \frac{G_\text{F}^2}{\pi(2J+1)v^2}\sum_{\text{spins}}|\mathcal{M}|^2 = \frac{8G_\text{F}^2}{\pi v^2}\Lambda^2 J(J+1)\frac{S(|\boldsymbol{q}|)}{S(0)} \ , \qquad (6.26)$$

The function $S(|\boldsymbol{q}|)$ encodes the momentum dependence of the cross section and is conventionally parameterized by

$$S(|\boldsymbol{q}|) = a_0^2 S_{00}(|\boldsymbol{q}|) + a_0 a_1 S_{01}(|\boldsymbol{q}|) + a_1^2 S_{11}(|\boldsymbol{q}|) \ , \qquad (6.27)$$

where $a_0 = a_p + a_n$ and $a_1 = a_p - a_n$ are isoscalar and isovector coupling, respectively. $S(|\boldsymbol{q}|)$ can be extended to include not only the explicit q-dependence from equation (6.25) but also the nuclear form factor, which is less important in this case.

---

[1]Of course, in the center-of-mass frame, we simply have $\tilde{\boldsymbol{p}} = -\boldsymbol{p}$.

[2]Note that while the time-component of P^μ is of order m_N, the time-component of q_μ is strongly suppressed, because $q_0 = E' - E \approx 1/2m_N(v'^2 - v^2) = \mathcal{O}(p^2/m)$.
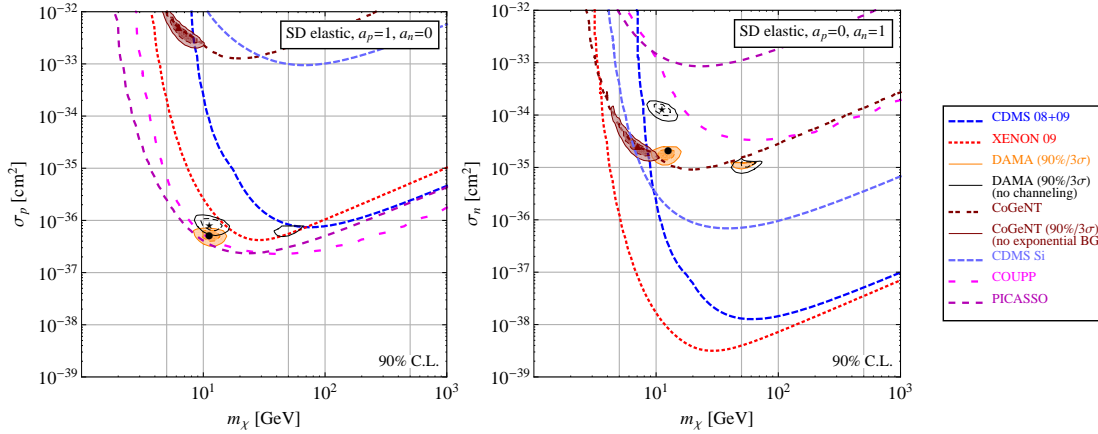
Figure 6.2: Exclusion limits from various dark matter direct detection experiments compared with the favored regions from DAMA and CoGeNT for spin-dependent interaction. For dark matter that couples only to the neutron spin, meaning $a_n = 1$, $a_p = 0$, the results from DAMA and CoGeNT are clearly excluded by XENON10. For $a_p = 1$, $a_n = 0$, XENON10 is not very sensitive, but the experiments COUPP and PICASSO give strong constraints. Figure taken from [14].

The parameters S_{ij} can either be measured experimentally or calculated from nuclear shell models (see for example [83]).

Clearly, exclusion limits for spin-dependent interactions are very different from the spin-independent ones. First of all, there is no factor of A^2, so the cross section will no longer be enhanced for heavy nuclei. What really matters, is the spin of the nucleus, contained in the parameter Λ. As a consequence, experiments based on germanium are rather insensitive to spin-dependent interactions, while strong exclusion limits are obtained from experiments that use fluorine as the target, for example COUPP [21] and PICASSO [22]. We present typical exclusion limits in figure 6.2.

6.3 Momentum and velocity dependence in matrix elements

We have shown above how spin-independent and spin-dependent interactions may arise. The two interaction terms that we considered, equation (6.2) and equation (6.13), are in fact the dominant ones if the dark matter particle is a neutralino. However, in general models it is possible that these terms are absent and other terms, that would normally give only sub-leading contributions, become important.

To give a simple example, let us consider the modification of equation (6.1). We replace the scalar mediator boson by a pseudoscalar, which has slightly different

couplings [78]

$$\mathcal{L} \supset i\alpha\phi\overline{\chi}\gamma^5\chi + \beta_q\phi\overline{q}q + \text{h.c.} \tag{6.28}$$

Since nothing changes in the quark sector, the matching to nucleus fields can be performed as above, giving

$$\mathcal{M} = (Zf_p + (A - Z)f_n)\,\overline{\chi}\gamma^5\chi\overline{N}NF(\boldsymbol{q}^2)\,. \tag{6.29}$$

However, as we take the non-relativistic limit, new structures appear. Using the result from equation (6.19), we get

$$\mathcal{M} = (Zf_p + (A - Z)f_n)\,\frac{\boldsymbol{q}}{2m_\chi}\cdot\chi_h^\dagger\boldsymbol{\sigma}\chi_h N_h^\dagger N_h F(\boldsymbol{q}^2) \propto \frac{\boldsymbol{q}\cdot\boldsymbol{s}_\chi}{m_\chi}\,. \tag{6.30}$$

Consequently, after taking the spin average of $|\mathcal{M}|^2$, the resulting cross section will be proportional to $\boldsymbol{q}^2/m_\chi^2$. Consequently, scattering with small momentum transfer will be suppressed, while scattering of light dark matter particles will be enhanced. As a result, the differential event rate will no longer be exponentially falling, but will rise at low recoil energies and then reach a maximum around $10\,\text{keV}$ (see [78]). Figure 6.1b shows how this change affects exclusion limits.

This simple example demonstrates that we can expect new experimental signatures in the absence of unsuppressed interaction terms. Our aim for this chapter is to calculate systematically all possible terms that can arise at next-to-leading order and understand the resulting cross sections. Although there are quite many operators that we can write down in the fundamental theory, the matrix elements in the non-relativistic limit are rather simple, because they can only depend on scalar products of the four available vectors $\boldsymbol{q}$, $\boldsymbol{P}$, $\boldsymbol{s}_N$ and $\boldsymbol{s}_\chi$, where each power of $|\boldsymbol{q}|$ or $|\boldsymbol{P}|$ must be divided by either m_N or m_χ.

We will perform the calculation in three separate steps. In this section, we complete the list of fermion bilinears and calculate the non-relativistic limit for each. In the following section, we will discuss Lorentz invariant products of two fermion bilinears and give the non-relativistic limit of all possible four-fermion interactions. In this context, we will also consider the contraction of a fermion bilinear with P_μ or q_μ. Finally, in the last section of this chapter, we will return to the matching of quark operators to nucleus operators and state all terms that can appear in the process.

We have already determined the non-relativistic limits of the scalar operator $\overline{N}N$ in equation (6.11), the pseudoscalar operator $\overline{N}\gamma^5N$ in equation (6.19), and the axial vector operator $\overline{N}\gamma^\mu\gamma^5N$ in equation (6.20). To complete the list of fermion bilinears, we now calculate the non-relativistic limits of the vector operator $\overline{N}\gamma^\mu N$, the tensor operator $\overline{N}\sigma^{\mu\nu}N$, and the pseudotensor operator $\overline{N}\sigma^{\mu\nu}\gamma^5N$, where $\sigma^{\mu\nu} = \frac{i}{2}\left[\gamma^\mu, \gamma^\nu\right]$.

$$\overline{N}(p')\gamma^\mu N(p) = N^\dagger(p')\gamma^0\gamma^\mu N(p)$$

$$
= \frac{1}{2m_N} \left(N_h^\dagger \sqrt{p' \cdot \sigma}, \ N_h^\dagger \sqrt{p' \cdot \overline{\sigma}} \right) \begin{pmatrix} 0 & \mathbb{1} \\ \mathbb{1} & 0 \end{pmatrix} \begin{pmatrix} 0 & \sigma^\mu \\ \overline{\sigma}^\mu & 0 \end{pmatrix} \begin{pmatrix} \sqrt{p \cdot \sigma} N_h \\ \sqrt{p \cdot \overline{\sigma}} N_h \end{pmatrix}
$$

$$
= \frac{1}{2m_N} N_h^\dagger \left(\sqrt{p' \cdot \overline{\sigma}} \sigma^\mu \sqrt{p \cdot \overline{\sigma}} + \sqrt{p' \cdot \sigma} \overline{\sigma}^\mu \sqrt{p \cdot \sigma} \right) N_h
$$

$$
= \begin{cases} N_h^\dagger N_h & \text{for } \mu = 0 \\ \frac{P^i}{2m_N} N_h^\dagger N_h - \frac{iq_j}{2m_N} \epsilon^{ijk} N_h^\dagger \sigma_k N_h & \text{for } \mu = i \end{cases} , \tag{6.31}
$$

where we have used equation (A.6). In contrast to the axial vector bilinear, here the time component is unsuppressed, while the spatial components are of higher order.

Similar, but more cumbersome, calculations give for the tensor operators

$$
\overline{N}(p') \sigma^{\mu\nu} N(p) = \begin{cases} \frac{iq^i}{2m_N} N_h^\dagger N_h + \frac{P_j}{2m_N} \epsilon^{ijk} N_h^\dagger \sigma_k N_h & \text{for } \mu = i, \nu = 0 \\ \epsilon^{ijk} N_h^\dagger \sigma_k N_h & \text{for } \mu = i, \nu = j \end{cases} , \tag{6.32}
$$

$$
\overline{N}(p') \sigma^{\mu\nu} \gamma^5 N(p) = \begin{cases} -i N_h^\dagger \sigma^i N_h & \mu = i, \nu = 0 \\ \frac{i}{2m_N} N_h^\dagger P^{[i} \sigma^{j]} N_h - \frac{q_k}{2m_N} \epsilon^{ijk} N_h^\dagger N_h & \mu = i, \nu = j \end{cases} , \tag{6.33}
$$

where $P^{[i} \sigma^{j]} = P^i \sigma^j - P^j \sigma^i$. Note that both operators are anti-symmetric in μ and ν because $\sigma^{\mu\nu} = -\sigma^{\nu\mu}$. The corresponding expressions for the dark matter bilinears can be obtained in complete analogy by replacing m_N with m_χ and $\boldsymbol{q}, \boldsymbol{P}$ with $-\boldsymbol{q}, -\boldsymbol{P}$.

6.4 General analysis of four-fermion interactions

With the results from the previous sections, we can now calculate the non-relativistic limit of any four-fermion interaction. In general, a four-fermion interaction is obtained by combining two fermion bilinears with matching Lorentz structure. If the Lorentz structure does not match, we can still combine the two bilinears by contracting all remaining Lorentz indices with powers of q^μ or P^μ. Doing so essentially corresponds to allowing higher dimensional operators with additional derivatives that result from a more complete high energy theory. For dimensional reasons, the additional powers of $|\boldsymbol{q}|$ and $|\boldsymbol{P}|$ must be divided by a mass scale Λ, which can be understood as the scale of new physics. However, Λ can be at or even below the TeV-scale, so there is no large hierarchy between Λ and $m_{\chi,N}$.[1] Therefore, we assume that $|\boldsymbol{q}|/\Lambda$ and $|\boldsymbol{P}|/\Lambda$ are of the same order as $|\boldsymbol{q}|/m$ and $|\boldsymbol{P}|/m$ rather than of order q^2/m^2 and P^2/m^2 and include them in our calculations.

First of all we observe that certain combinations lead to unsuppressed matrix elements and cross sections that remain non-zero as $|\boldsymbol{q}|, |\boldsymbol{P}| \to 0$. We have already seen in section 6.1 that the product (scalar)×(scalar) leads to unsuppressed spin-independent interactions and in section 6.2 that (axial)×(axial) leads to un-

---

[1]In fact, in section 6.5, we will even encounter cases where $\Lambda = m_N$.

suppressed spin-dependent interactions.[1]   Similarly, (vector)×(vector) leads to unsuppressed spin-independent interactions, while both, (tensor)×(tensor) and (pseudotensor)×(pseudotensor), give unsuppressed spin-dependent interactions.[2]

Note, however, that the cross sections obtained in each case are not necessarily equal. The reason is, that operators with different Lorentz structure couple to different charges. For example, the operator $\bar{q}q$ is sensitive to all quarks in the nucleon (including sea quarks), so the resulting coupling to the nucleus will be proportional to the nucleus mass. The operator $\bar{q}\gamma^\mu q$, on the other hand, is a conserved current and consequently is only sensitive to valence quarks. The resulting cross section will therefore depend on the nuclear charge.[3] Also form factors will in general be different (although in this case they are coincidentally the same, because we observe experimentally that the distribution of mass inside a nucleus matches the distribution of charge). We will come back to this discussion in section 6.5.

The unsuppressed operators have been discussed extensively in the literature (see for example [14]). Only recently, various authors have begun to study suppressed operators as well [78, 84, 85]. Physical motivation for such operators comes for example from the idea that the dark matter particle may be composite and interact with nuclei only through its electromagnetic dipole moment [86–89]. So far, however, only some special models have been considered. Here, we want to discuss suppressed operators in full generality and will therefore derive a complete list of matrix elements that can arise at next-to-leading order from four-fermion interactions.

6.4.1 Scalar interactions

We begin with the simplest case, where the dark matter and nucleus bilinear are both either Lorentz scalars or pseudoscalars, so that there are no free Lorentz indices. We have already discussed the case (scalar)×(scalar), which leads to unsuppressed spin-independent interaction, and the case (pseudoscalar)×(scalar), which depends on the spin of the dark matter particle and the momentum transfer but not on the nuclear spin, consequently giving suppressed spin-independent interactions. Similarly, the case (scalar)×(pseudoscalar) has a factor of $|\boldsymbol{q}|/m_N$ instead of $|\boldsymbol{q}|/m_\chi$ and depends on the nuclear spin instead of the dark matter spin, therefore giving suppressed spin-dependent interactions. The product (pseudoscalar)×(pseudoscalar) is suppressed by two powers of $|\boldsymbol{q}|/m$, so we neglect it completely.

Next, we can form additional Lorentz scalars and pseudoscalars by contracting

---

[1]The notation (axial)×(axial) stands for the contraction of axial dark matter bilinear and axial nucleus bilinear.

[2]In fact, since $\sigma^{\mu\nu}\gamma^5 = \frac{i}{2}\epsilon^{\mu\nu\kappa\lambda}\sigma_{\kappa\lambda}$, the product (tensor)×(tensor) is equivalent to the product (pseudotensor)×(pseudotensor).

[3]Charge in this context means charge under the relevant gauge group. If the charge assignments for up- and down-quark coincide with their electromagnetic charge, then nuclear charge indeed means Z.

Operator	Interaction	Non-relativistic matrix element
$\overline{\chi}\chi\overline{N}N$	Unsuppressed SI	1
$\overline{\chi}\gamma^5\chi\overline{N}N$	Suppressed SI	$\boldsymbol{s}_\chi \cdot \boldsymbol{q}/2m_\chi$
$\overline{\chi}\chi\overline{N}\gamma^5 N$	Suppressed SD	$-\boldsymbol{s}_N \cdot \boldsymbol{q}/2m_N$
$\overline{\chi}\gamma^5\chi\overline{N}\gamma^5 N$	Strongly suppressed	0
$\overline{\chi}\chi\overline{N}\gamma^\mu N P_\mu/\Lambda$	Suppressed SI	$2m_N/\Lambda$
$\overline{\chi}\chi\overline{N}\gamma^\mu\gamma^5 N q_\mu/\Lambda$	Suppressed SD	$-\boldsymbol{s}_N \cdot \boldsymbol{q}/\Lambda$
$\overline{\chi}\chi\overline{N}\gamma^\mu N q_\mu/\Lambda$	Vanishes	0
$\overline{\chi}\chi\overline{N}\gamma^\mu\gamma^5 N P_\mu/\Lambda$	Vanishes	0
$\overline{\chi}\gamma^5\chi\overline{N}\gamma^\mu N P_\mu/\Lambda$	Suppressed SI	$2m_N\boldsymbol{s}_\chi \cdot \boldsymbol{q}/m_\chi\Lambda$
$\overline{\chi}\gamma^5\chi\overline{N}\gamma^\mu\gamma^5 N q_\mu/\Lambda$	Strongly suppressed	0
$\overline{\chi}\gamma^5\chi\overline{N}\gamma^\mu N q_\mu/\Lambda$	Vanishes	0
$\overline{\chi}\gamma^5\chi\overline{N}\gamma^\mu\gamma^5 N P_\mu/\Lambda$	Vanishes	0

Table 6.1: Scalar products of fermion bilinears to first order in $|\boldsymbol{p}|/m$. The cases where the dark matter bilinear is a (pseudo)vector are analogous to the cases where the nucleus bilinear is a (pseudo)vector.

vectorial bilinears with q^μ/Λ or P^μ/Λ, meaning that we include derivative interactions. We get up to first order:

$$\overline{N}(p')\gamma^\mu N(p)\frac{q_\mu}{\Lambda} = 0 \, , \tag{6.34}$$

$$\overline{N}(p')\gamma^\mu N(p)\frac{P_\mu}{\Lambda} = \frac{2m_N}{\Lambda}N_h^\dagger N_h = \frac{2m_N}{\Lambda} \times (\text{scalar}) \, , \tag{6.35}$$

$$\overline{N}(p')\gamma^\mu\gamma^5 N(p)\frac{q_\mu}{\Lambda} = -\frac{q_i}{\Lambda}N_h^\dagger\sigma^i N_h = \frac{2m_N}{\Lambda} \times (\text{pseudoscalar}) \, , \tag{6.36}$$

$$\overline{N}(p')\gamma^\mu\gamma^5 N(p)\frac{P_\mu}{\Lambda} = 0 \, , \tag{6.37}$$

so that nothing new is obtained from these operators. Equations (6.34)–(6.37) are indeed correct not only to first order in $|\boldsymbol{p}|/m$, but to all orders. The reason is that $\gamma^\mu p_\mu N(p) = m_N N(p)$ and $\overline{N}(p')\gamma^\mu p'_\mu = m_N\overline{N}(p')$ as in equation (A.15). Consequently, we get for example

$$\overline{N}(p')\gamma^\mu N(p)q_\mu = \overline{N}(p')\gamma^\mu(p'_\mu - p_\mu)N(p) = \overline{N}(p')(m_N - m_N)N(p) = 0 \, . \tag{6.38}$$

The complete list of possible products is given in table 6.1.

6.4.2 Vector interactions

For the vectorial operators, something interesting happens. While the products (vector)×(vector) and (axial)×(axial) both give unsuppressed interactions, the product (vector)×(axial) is suppressed. The reason is that the vector current has an unsuppressed time component and suppressed spatial components, while it is the other way around for the axial current. In detail, we get

$$
\begin{aligned}
\overline{\chi}\gamma^\mu\gamma^5\chi\overline{N}\gamma_\mu N &= -\frac{\boldsymbol{P}}{2m_\chi}\cdot\chi_h^\dagger\boldsymbol{\sigma}\chi_h N_h^\dagger N_h \\
&\quad - \chi_h^\dagger\sigma_i\chi_h\left(\frac{P^i}{2m_N}N_h^\dagger N_h - \frac{iq_j}{2m_N}\epsilon^{ijk}N_h^\dagger\sigma_k N_h\right) \\
&= -\left(\frac{1}{2m_N}+\frac{1}{2m_\chi}\right)\boldsymbol{P}\cdot\chi_h^\dagger\boldsymbol{\sigma}\chi_h N_h^\dagger N_h + \frac{iq_j}{2m_N}\epsilon^{ijk}\chi_h^\dagger\sigma_i\chi_h N_h^\dagger\sigma_k N_h \\
&\propto -\frac{\boldsymbol{P}\cdot\boldsymbol{s}_\chi}{2\mu} + \frac{i\boldsymbol{q}\cdot(\boldsymbol{s}_N\times\boldsymbol{s}_\chi)}{2m_N} \ .
\end{aligned}
\tag{6.39}
$$

Taking the spin average, gives

$$
\frac{1}{4}\sum_{\text{spins}}|\mathcal{M}|^2 = \frac{\boldsymbol{P}^2}{4\mu^2} + \frac{2\boldsymbol{q}^2}{4m_N^2} \ ,
\tag{6.40}
$$

where the additional factor of 2 arises because of $\epsilon^{ijk}\epsilon_{ilk}=2\delta_l^j$.

For the first time, we obtain a cross section, that actually depends on $\boldsymbol{P}$. To understand the implications of this result, remember that $\boldsymbol{P}^2=(\boldsymbol{p}+\boldsymbol{p}')^2=(2\boldsymbol{p}+\boldsymbol{q})^2=4\boldsymbol{p}^2+4\boldsymbol{p}\boldsymbol{q}+\boldsymbol{q}^2$. At the same time, we have in the center-of-mass frame $\boldsymbol{p}^2=\boldsymbol{p}'^2=(\boldsymbol{p}+\boldsymbol{q})^2=\boldsymbol{p}^2+2\boldsymbol{p}\boldsymbol{q}+\boldsymbol{q}^2$, and consequently, $\boldsymbol{P}^2=4\boldsymbol{p}^2-\boldsymbol{q}^2=4\mu^2v^2-\boldsymbol{q}^2$. Therefore,

$$
\frac{1}{4}\sum_{\text{spins}}|\mathcal{M}|^2 = v^2 - \frac{\boldsymbol{q}^2}{4\mu^2} + \frac{\boldsymbol{q}^2}{2m_N^2} \ .
\tag{6.41}
$$

The resulting cross section depends not only on the momentum transfer, but also on the velocity of the dark matter particle. At equal momentum transfer, fast dark matter particles contribute more to the differential event rate than slow ones.

As above, we can also consider the products of vectorial bilinears with other bilinears, where free Lorentz indices are contracted with either P^μ or q^μ. The combinations of vectorial and scalar bilinears have already been discussed in section 6.4.1, so we limit ourselves to the combination of vectorial and tensor operators here:

$$
\overline{N}(p')\sigma^{\mu\nu}N(p)\frac{q_\mu}{\Lambda} = \begin{cases} 0 & \text{for } \nu=0 \\ \frac{q_j}{\Lambda}\epsilon^{ijk}N_h^\dagger\sigma_k N_h & \text{for } \nu=i \end{cases} \ ,
\tag{6.42}
$$

Operator	Interaction	Non-relativistic matrix element
$\overline{\chi}\gamma^\mu\chi\overline{N}\gamma_\mu N$	Unsuppressed SI	1
$\overline{\chi}\gamma^\mu\gamma^5\chi\overline{N}\gamma_\mu\gamma^5 N$	Unsuppressed SD	$\boldsymbol{s}_N \cdot \boldsymbol{s}_\chi$
$\overline{\chi}\gamma^\mu\gamma^5\chi\overline{N}\gamma_\mu N$	Suppressed SI and SD	$-\frac{\boldsymbol{P}\cdot\boldsymbol{s}_\chi}{2\mu} + \frac{i\boldsymbol{q}\cdot(\boldsymbol{s}_N\times\boldsymbol{s}_\chi)}{2m_N}$
$\overline{\chi}\gamma^\mu\chi\overline{N}\gamma^\mu\gamma^5 N$	Suppressed SD	$\frac{\boldsymbol{P}\cdot\boldsymbol{s}_N}{2\mu} - \frac{i\boldsymbol{q}\cdot(\boldsymbol{s}_\chi\times\boldsymbol{s}_N)}{2m_\chi}$
$\overline{\chi}\gamma^\nu\chi\overline{N}\sigma_{\mu\nu}\gamma^5 N P^\mu/\Lambda$	Suppressed SD	$\frac{im_N}{\Lambda}\left[\frac{\boldsymbol{P}\cdot\boldsymbol{s}_N}{\mu} - \frac{i\boldsymbol{q}\cdot(\boldsymbol{s}_\chi\times\boldsymbol{s}_N)}{m_\chi}\right]$
$\overline{\chi}\gamma^\nu\chi\overline{N}\sigma_{\mu\nu}\gamma^5 N q^\mu/\Lambda$	Suppressed SD	$i\boldsymbol{q}\cdot\boldsymbol{s}_N/\Lambda$
$\overline{\chi}\gamma^\nu\chi\overline{N}\sigma_{\mu\nu} N P^\mu/\Lambda$	Strongly suppressed	0
$\overline{\chi}\gamma^\nu\chi\overline{N}\sigma_{\mu\nu} N q^\mu/\Lambda$	Strongly suppressed	0
$\overline{\chi}\gamma^\nu\gamma^5\chi\overline{N}\sigma_{\mu\nu} N P^\mu/\Lambda$	Suppressed SI	$i\boldsymbol{s}_\chi\cdot\boldsymbol{q}/\Lambda$
$\overline{\chi}\gamma^\nu\gamma^5\chi\overline{N}\sigma_{\mu\nu} N q^\mu/\Lambda$	Suppressed SD	$\boldsymbol{q}\cdot(\boldsymbol{s}_\chi\times\boldsymbol{s}_N)/\Lambda$
$\overline{\chi}\gamma^\nu\gamma^5\chi\overline{N}\sigma_{\mu\nu}\gamma^5 N P^\mu/\Lambda$	Suppressed SD	$2im_N\boldsymbol{s}_\chi\cdot\boldsymbol{s}_N/\Lambda$
$\overline{\chi}\gamma^\nu\gamma^5\chi\overline{N}\sigma_{\mu\nu}\gamma^5 N q^\mu/\Lambda$	Strongly suppressed	0

Table 6.2: Vector products of fermion bilinears to first order in $|\boldsymbol{p}|/m$. The cases where the dark matter operator is a (pseudo)tensor are analogous to the cases where the nucleus operator is a (pseudo)tensor.

$$\overline{N}(p')\sigma^{\mu\nu}N(p)\frac{P_\mu}{\Lambda} = \begin{cases} 0 & \text{for } \nu = 0 \\ -\frac{iq^i}{\Lambda}N_h^\dagger N_h & \text{for } \nu = i \end{cases} = -\frac{iq^\nu}{\Lambda} \times (\text{scalar}) , \quad (6.43)$$

$$\overline{N}(p')\sigma^{\mu\nu}\gamma^5 N(p)\frac{q_\mu}{\Lambda} = \begin{cases} \frac{iq^i}{\Lambda}N_h^\dagger\sigma_i N_h & \text{for } \nu = 0 \\ 0 & \text{for } \nu = j \end{cases} , \quad (6.44)$$

$$\overline{N}(p')\sigma^{\mu\nu}\gamma^5 N(p)\frac{P_\mu}{\Lambda} = \begin{cases} \frac{i\boldsymbol{P}}{\Lambda}\cdot N_h^\dagger\boldsymbol{\sigma} N_h & \nu = 0 \\ \frac{2im_N}{\Lambda}N_h^\dagger\sigma^i N_h & \nu = i \end{cases} \approx \frac{2im_N}{\Lambda} \times (\text{axial}) . \quad (6.45)$$

Equation (6.43) and equation (6.45) also follow directly from equation (A.15) and the observation that

$$\begin{aligned} P_\mu\sigma^{\mu\nu} &= \frac{i}{2}\left(\gamma^\mu\gamma^\nu - \gamma^\nu\gamma^\mu\right)(p'_\mu + p_\mu) \\ &= \frac{i}{2}\left(\gamma^\mu(2p'_\mu - q_\mu)\gamma^\nu - \gamma^\nu\gamma^\mu(2p_\mu + q_\mu)\right) \\ &= i\left(\gamma^\mu p'_\mu\gamma^\nu - \gamma^\nu\gamma^\mu p_\mu\right) - \frac{i}{2}\left(\gamma^\mu\gamma^\nu + \gamma^\nu\gamma^\mu\right)q_\mu \\ &= i\left(\gamma^\mu p'_\mu\gamma^\nu - \gamma^\nu\gamma^\mu p_\mu - q^\nu\right) = i(\not{p}'\gamma^\nu - \gamma^\nu\not{p} - q^\nu) . \end{aligned} \quad (6.46)$$

We present all possible products in table 6.2.

Operator	Interaction	Non-relativistic matrix element
$\overline{\chi}\sigma^{\mu\nu}\chi\overline{N}\sigma_{\mu\nu}N$	Unsuppressed SD	$2\boldsymbol{s}_N \cdot \boldsymbol{s}_\chi$
$\overline{\chi}\sigma^{\mu\nu}\gamma^5\chi\overline{N}\sigma_{\mu\nu}\gamma^5 N$	Unsuppressed SD	$2\boldsymbol{s}_N \cdot \boldsymbol{s}_\chi$
$\overline{\chi}\sigma^{\mu\nu}\gamma^5\chi\overline{N}\sigma_{\mu\nu}N$	Suppressed SD and SI	$\frac{i\boldsymbol{P}\cdot(\boldsymbol{s}_\chi\times\boldsymbol{s}_N)(m_N-m_\chi)}{m_\chi m_N} - \frac{\boldsymbol{q}\cdot\boldsymbol{s}_\chi}{m_N} - \frac{\boldsymbol{q}\cdot\boldsymbol{s}_N}{m_\chi}$
$\overline{\chi}\sigma^{\mu\nu}\chi\overline{N}\sigma_{\mu\nu}\gamma^5 N$	Suppressed SD and SI	$\frac{i\boldsymbol{P}\cdot(\boldsymbol{s}_\chi\times\boldsymbol{s}_N)(m_N-m_\chi)}{m_\chi m_N} - \frac{\boldsymbol{q}\cdot\boldsymbol{s}_\chi}{m_N} - \frac{\boldsymbol{q}\cdot\boldsymbol{s}_N}{m_\chi}$

Table 6.3: Tensor products of fermion bilinears to first order in $|\boldsymbol{p}|/m$.

6.4.3 Tensor interactions

By now there is only one combination that we have not discussed yet: the product of tensor and pseudotensor. We get

$$\overline{\chi}\sigma^{\mu\nu}\gamma^5\chi\overline{N}\sigma_{\mu\nu}N = -\frac{q^i}{m_N}N_h^\dagger N_h\chi_h^\dagger\sigma_i\chi_h - \frac{q^i}{m_\chi}N_h^\dagger\sigma_i N_h\chi_h^\dagger\chi_h \tag{6.47}$$

$$+ iP_i\left(\frac{1}{m_\chi} - \frac{1}{m_N}\right)\epsilon^{ijk}\chi_h^\dagger\sigma_j\chi_h N_h^\dagger\sigma_k N_h \tag{6.48}$$

$$\propto i\boldsymbol{P}\cdot(\boldsymbol{s}_\chi\times\boldsymbol{s}_N)\left(\frac{1}{m_\chi} - \frac{1}{m_N}\right) - \frac{\boldsymbol{q}\cdot\boldsymbol{s}_\chi}{m_N} - \frac{\boldsymbol{q}\cdot\boldsymbol{s}_N}{m_\chi} , \tag{6.49}$$

which, as expected from the symmetry between tensor and pseudotensor, is invariant under the exchange $\chi \leftrightarrow N$. We summarize the tensor operators in table 6.3.

6.5 Matching and form factors

With the results from the previous section, we can calculate cross sections once we know the effective interaction between dark matter and nucleus. What remains is the question how to determine the effective nucleus operator from the fundamental Lagrangian. In the limit of zero momentum transfer, the answer is easy. If the quark operator has the form $\beta_q\overline{q}\mathcal{O}q$, where $\mathcal{O}$ is an arbitrary product of γ-matrices, the corresponding nucleus operator must also be of the form $g\overline{N}\mathcal{O}N$, because both operators must have the same Lorentz structure and parity. The only problem that remains in this case is how to obtain the coupling constant g from the fundamental coupling constants β_q. This problem, however, is well understood for almost all operators — see [90] for a good review. The only exception is the operator $\overline{q}\gamma^5 q$, because it is not present in the Standard Model, so there is no way to determine experimentally the coupling constants and form factors that would arise in the process of matching this operator to the corresponding one for nuclei. Of course, it should be possible to calculate these quantities from QCD, but to the best of our knowledge such a calculation has not been done.

For non-zero momentum transfer, matching becomes more difficult, because now the resulting nucleus operator can depend on the Lorentz vectors q^μ and P^μ as well as the Lorentz scalar q^2 (or equivalently $\boldsymbol{q}^2 = -q^2$). The first consequence is the occurrence of form factors, so $\beta_q \overline{q} \mathcal{O} q$ will match to $g\overline{N}\mathcal{O}NF(\boldsymbol{q}^2)$ with $F(0) = 1$. These form factors will, in general, be different for different operators.[1] The second consequence is that additional operators may appear in the matching process. We have seen one example already in section 6.2 for the matching of the axial vector bilinear. Fortunately, any new operator must have the same Lorentz structure and parity as the original one. Let us consider all possible quark operators in turn and determine in each case the most general nucleus operator that can be induced in the matching process.

For the scalar operator $\overline{q}q$, we get

$$
\begin{aligned}
\overline{q}q \to{}& \overline{N}N F_1^{(\mathrm{s})}(\boldsymbol{q}^2) + \overline{N}\gamma^\mu N q_\mu F_2^{(\mathrm{s})}(\boldsymbol{q}^2) \\
&+ \overline{N}\gamma^\mu N P_\mu F_3^{(\mathrm{s})}(\boldsymbol{q}^2) + \overline{N}\sigma^{\mu\nu} N P_\mu q_\nu F_4^{(\mathrm{s})}(\boldsymbol{q}^2) \,.
\end{aligned}
\tag{6.50}
$$

However, we have seen already in section 6.4.1 that the second term vanishes and the third term is again proportional to $\overline{N}N$. A similar calculation shows that the fourth term is proportional to $\boldsymbol{q}^2 \overline{N}N$, so that in fact, the only remaining operator is

$$
\overline{q}q \to \overline{N}N \tilde{F}_1^{(\mathrm{s})}(\boldsymbol{q}^2) \,.
\tag{6.51}
$$

This result justifies the assumption made in section 6.1 that no additional operators appear in the matching process for the scalar operator.

Analogously, we can write

$$
\begin{aligned}
\overline{q}\gamma^5 q \to{}& \overline{N}\gamma^5 N F_1^{(\mathrm{p})}(\boldsymbol{q}^2) + \overline{N}\gamma^\mu \gamma^5 N q_\mu F_2^{(\mathrm{p})}(\boldsymbol{q}^2) \\
&+ \overline{N}\gamma^\mu \gamma^5 N P_\mu F_3^{(\mathrm{p})}(\boldsymbol{q}^2) + \overline{N}\sigma^{\mu\nu} \gamma^5 N P_\mu q_\nu F_4^{(\mathrm{p})}(\boldsymbol{q}^2) \,.
\end{aligned}
\tag{6.52}
$$

In this case, the third term vanishes, the second one is proportional to $\overline{N}\gamma^5 N$ and the last one can be decomposed into a term proportional to $\overline{N}\gamma^5 N$ and a term proportional to $\boldsymbol{q}^2 \overline{N}\gamma^5 N$. Consequently, we can write

$$
\overline{q}\gamma^5 q \to \overline{N}\gamma^5 N \tilde{F}_1^{(\mathrm{p})}(\boldsymbol{q}^2) \,.
\tag{6.53}
$$

For the vector operator, things are more complicated. In general, five operators

---

[1]It is often argued that we only need two different form factors, one for spin-dependent and one for spin-independent scattering. The argument is that we can take the non-relativistic limit already for the nucleon fields. The non-relativistic matrix elements will then be independent of the detailed Lorentz structure of the operators. Consequently, the form factors describing the structure of the nucleus must be the same for all matrix elements that have the same dependence on the nucleon spins. However, it is not quite clear whether we can indeed treat nucleons as non-relativistic, so this solution is at best an approximation (see [78] for a discussion).

could appear in the matching process:

$$\bar{q}\gamma^\mu q \rightarrow \overline{N}\gamma^\mu N F_1^{(\mathrm{v})}(\boldsymbol{q}^2) + \overline{N}N q^\mu F_2^{(\mathrm{v})}(\boldsymbol{q}^2) + \overline{N}N P^\mu F_3^{(\mathrm{v})}(\boldsymbol{q}^2)$$
$$+ \overline{N}\sigma^{\mu\nu} N q_\nu F_4^{(\mathrm{v})}(\boldsymbol{q}^2) + \overline{N}\sigma^{\mu\nu} N P_\nu F_5^{(\mathrm{v})}(\boldsymbol{q}^2) . \tag{6.54}$$

However, we know from equation (6.46), that the last term is proportional to $\overline{N}N q^\mu$. Moreover, we can use the Gordon identity, which states that

$$\overline{N}N P^\mu = 2m\overline{N}\gamma^\mu N - i\overline{N}\sigma^{\mu\nu} q_\nu N . \tag{6.55}$$

Consequently, only three of the four remaining terms are independent, and we can write

$$\bar{q}\gamma^\mu q \rightarrow \overline{N}\gamma^\mu N \tilde{F}_1^{(\mathrm{v})}(\boldsymbol{q}^2) + \overline{N}N q^\mu \tilde{F}_2^{(\mathrm{v})}(\boldsymbol{q}^2) + \overline{N}\sigma^{\mu\nu} N q_\nu \tilde{F}_4^{(\mathrm{v})}(\boldsymbol{q}^2) . \tag{6.56}$$

Finally, we use the fact that $\bar{q}\gamma^\mu q$ is a conserved current, so any induced nucleus operator Γ^μ must satisfy the Ward identity $q_\mu \Gamma^\mu = 0$. While the first and last term in equation (6.56) automatically vanish when contracted with q_μ, the second one does not, so we must require $\tilde{F}_2^{(\mathrm{v})}(\boldsymbol{q}^2) = 0$. Consequently, the most general form for the nucleus operator induced from $\bar{q}\gamma^\mu q$ is (adapting the notation from [79])

$$\bar{q}\gamma^\mu q \rightarrow \overline{N}\left(F_1(\boldsymbol{q}^2)\gamma^\mu + \frac{iF_2(\boldsymbol{q}^2)}{2m_N}\sigma^{\mu\nu} q_\nu \right) N . \tag{6.57}$$

The second term can be interpreted as the contribution of the magnetic dipole moment of the nucleus.

Normally, the first term gives the leading order contribution to the scattering cross sections for dark matter, so the second term can be safely neglected. However, from equation (6.31) and equation (6.42) we know that the spatial components of both operators, $\overline{N}\gamma_\mu N$ and $\overline{N}\sigma_{\mu\nu} N q^\nu/m_N$, are of the order $|\boldsymbol{q}|/m_N$. Consequently, if we combine these operators with a dark matter bilinear with suppressed time component (for example $\overline{\chi}\gamma^\mu\gamma^5\chi$), the contribution of the vector operator will be suppressed and both terms in equation (6.57) contribute at the same (namely next-to-leading) order.

For the axial operator, we can proceed in analogy. In general, we would have

$$\bar{q}\gamma^\mu\gamma^5 q \rightarrow \overline{N}\gamma^\mu\gamma^5 N F_1^{(\mathrm{a})}(\boldsymbol{q}^2) + \overline{N}\gamma^5 N q^\mu F_2^{(\mathrm{a})}(\boldsymbol{q}^2) + \overline{N}\gamma^5 N P^\mu F_3^{(\mathrm{a})}(\boldsymbol{q}^2)$$
$$+ \overline{N}\sigma^{\mu\nu}\gamma^5 N q_\nu F_4^{(\mathrm{a})}(\boldsymbol{q}^2) + \overline{N}\sigma^{\mu\nu}\gamma^5 N P_\nu F_5^{(\mathrm{a})}(\boldsymbol{q}^2) . \tag{6.58}$$

Again, only three terms are independent, so we can write

$$\bar{q}\gamma^\mu q \rightarrow \overline{N}\gamma^\mu\gamma^5 N \tilde{F}_1^{(\mathrm{a})}(\boldsymbol{q}^2) + \overline{N}\gamma^5 N q^\mu \tilde{F}_2^{(\mathrm{a})}(\boldsymbol{q}^2) + \overline{N}\sigma^{\mu\nu}\gamma^5 N q_\nu \tilde{F}_4^{(\mathrm{a})}(\boldsymbol{q}^2) . \tag{6.59}$$

This time, however, there is no conserved current which allows us to eliminate the

second term. In fact, we have seen already in section 6.2, that this term must be present to account for the divergence at $q^2 = m_\pi^2$. The third term, on the other hand, corresponds to the electric dipole moment of the nucleus.

For the tensor operator (and the pseudotensor operator), we can again use the Gordon identity to replace $\overline{N}(P^\mu q^\nu - P^\nu q^\mu)N$ by $2m\overline{N}(\gamma^\mu q^\nu - \gamma^\nu q^\mu)N$, neglecting terms that are quadratic in q. Consequently, the tensor operator will match to

$$\overline{q}\sigma^{\mu\nu}q \rightarrow \overline{N}\sigma^{\mu\nu}N F_1^{(\mathrm{t})}(\boldsymbol{q}^2) + \overline{N}(\gamma^\mu q^\nu - \gamma^\nu q^\mu)N F_2^{(\mathrm{t})}(\boldsymbol{q}^2)$$
$$+ \overline{N}(\gamma^\mu P^\nu - \gamma^\nu P^\mu)N F_3^{(\mathrm{t})}(\boldsymbol{q}^2) . \tag{6.60}$$

6.6 Summary of results

We have now presented all the pieces needed to calculate cross sections for the scattering of dark matter particles on nuclei from any fundamental interaction involving fermionic dark matter. What one has to do is

1. Obtain the effective four-fermion interaction on the quark level.

2. Match the quark bilinear to the corresponding nucleus bilinear using the formulas in this section.

3. Calculate (or measure) the effective coupling constants and the resulting form factors.

4. Take the non-relativistic limit of the resulting matrix element using the formulas given in section 6.4.

5. Calculate the spin average of $|\mathcal{M}|^2$.

Clearly, step 3 is the most difficult part and the results are known only for few simple cases.

To conclude, we observe that while the scattering of dark matter is rather simple at leading order, it gets more involved once leading order terms are absent. At next-to-leading order we must worry about the interplay between various form factors and coupling constants. The resulting cross sections can depend on the momentum transfer, the spin of the nucleus and even the velocity of the dark matter particle. As we have seen in chapters 3 and 4, the final results of XENON100 may exclude the possibility that the signals from DAMA and CoGeNT are due to unsuppressed SI interactions. In this case, it will be the next step to analyze the matrix elements that arise at next-to-leading order to see if any of these allow for a reconciliation of the different experiments. We leave such an analysis to future work.

Summary and conclusions

The fact that we have compelling evidence for the existence of dark matter from astrophysical and cosmological observations, but know only little about the particles that constitute most of it, is one of the greatest puzzles of modern physics. Not only do we want to understand the large abundance of dark matter in the universe, but we also hope to obtain first clues about physics beyond the Standard Model from the properties of the dark matter particle. Direct detection experiments, especially liquid xenon detectors, appear to be a very promising way to observe dark matter and finally solve this puzzle. Nevertheless, present experimental results are still far from providing a clear picture.

The claimed observations of a dark matter signal in the direct detection experiments DAMA and CoGeNT have led to a strong interest in dark matter particles with low mass ($m_\chi < 10\,\text{GeV}$). Liquid xenon detectors have difficulties to probe this parameter region because of their relatively high energy threshold. In this thesis, we have looked thoroughly at the sensitivity of liquid xenon detectors for low energy nuclear recoils. It depends essentially on four factors: the detector resolution, the cut acceptance, the relative scintillation efficiency of liquid xenon and the light collection efficiency of the detector. As the central result of our work, we obtain that none of these factors precludes the observation of low mass dark matter.

In chapter 1, we have reviewed the standard model of cosmology and the experimental evidence which leads to the conclusion that there must be 4 to 5 times more dark than visible matter in the universe. From the little we know about dark matter, it should be cold, collisionless, stable and non-baryonic. We have argued that Weakly Interacting Massive Particles are a good candidate for the dark matter particle because they possess all these properties and moreover are produced with the correct abundance in the early universe due to the WIMP-miracle.

In chapter 2, we have given an overview of experimental strategies to detect dark matter. We have derived and discussed the differential event rate in direct detection experiments and the characteristic signatures of a dark matter signal. The enhancement of the event rate for heavy nuclei is the first reason for using liquid xenon detectors. Additional advantages are the strong self-shielding and the high

scintillation and ionization yields. We have presented the principle of operation of the XENON100 detector and introduced the terminology relevant for the analysis of the primary and secondary scintillation signals, $S1$ and $S2$. Also, we have pointed out the tension between the signals observed by DAMA and CoGeNT and the null results from XENON and CDMS.

In chapter 3, we have discussed the reason for the large fluctuations of the $S1$ and the $S2$ signal in liquid xenon detectors at low energies. For the $S1$ signal, the detection process limits the detector resolution, leading in good approximation to a Poisson smearing of the low energy threshold. The statistical nature of the production process for photons is not important to describe $S1$ fluctuations, but we must take into account the production process for electrons to give a correct statistical description of the $S2$ signal. Consequently, the variance of the $S2$ signal is larger than expected from Poisson statistics. We have confirmed our model of fluctuations by performing Monte Carlo simulations of the nuclear recoil band, which agree well with experimental data. In conclusion, the resolution of liquid xenon detectors is rather poor at low energies. Nevertheless, the resulting smearing of the threshold improves the sensitivity of liquid xenon detectors significantly.

The cut acceptance can also be determined from Monte Carlo simulations of the nuclear recoil band. We find good agreement between the results of our simulations and the published values. However, this acceptance function includes neither the single scatter cut nor the nuclear recoil cut. We expect the single scatter cut to have a high acceptance, but emphasize the importance of a large rejection efficiency for multiple scatters. Otherwise, there will be the risk that a large number of multiple scatters in calibration data distorts the nuclear recoil band. The acceptance of the nuclear recoil cut, on the other hand, is difficult to determine, because the acceptance probability is not independent of the other cuts which we apply. Therefore, the flat 50% acceptance, which has been assumed previously, can be only an approximation. In fact, from a more careful treatment one obtains a higher acceptance at low recoil energies, so assuming a flat acceptance gives a conservative estimate.

In chapter 4 we have calculated the relative scintillation efficiency for low energy nuclear recoils in liquid xenon. Our idea was to develop a theory that predicts both, ionization and scintillation yield. This aim was achieved by combining Lindhard's theory for the initial production of electronic excitations and the well motivated assumption of energy independent partition between ionization and excitation in the underlying collisions. Our conclusion is that scintillation and ionization are correlated, so that a rapidly dropping $\mathcal{L}_{\text{eff}}$ would imply a drop in the scintillation yield which is incompatible with existing data. Consequently, we exclude the possibility of threshold effects that reduce electronic excitations in the keV range.

All these considerations lead to the conclusion that liquid xenon detectors possess an impressive sensitivity for low energy nuclear recoils corresponding to low mass dark matter. We have calculated the acceptance function for the XENON100 detector (see figure 4.5a) and predicted the sensitivity of the experiment after a runtime of

100 days (see figure 4.5b). In summary, XENON100 should definitely be able to confirm or rule out the results from CoGeNT and DAMA under the assumption of standard spin-independent scattering.

Whether XENON100 observes a dark matter signal or not, larger liquid xenon detectors will be built in the near future to increase the sensitivity and confirm the results from XENON100. We have dedicated chapter 5 to a study of such future detectors. In fact, liquid xenon detectors are very well suited for upscaling. The three factors that we considered above, namely detector resolution, cut acceptance and relative scintillation efficiency, remain essentially unchanged for larger detectors. What changes significantly, however, is the fourth factor, namely the light collection efficiency. With increasing detector dimensions, the light collection efficiency will be reduced. Thus, the low energy threshold of future liquid xenon detectors is expected to rise, leading to a loss of sensitivity for low mass dark matter.

To quantify this effect, we have performed Monte Carlo simulations of the light collection efficiency in dependence of the detector size and the absorption length of liquid xenon. We conclude that, unless the absorption length can be increased significantly, an increase in fiducial mass will not necessarily improve the sensitivity in the low energy region. A better sensitivity for low mass dark matter could, however, be achieved by changing the detector design in order to increase the number of photo-sensors. Specifically, we considered oblate detectors and detectors with 4π QUPID coverage.

While both of these options are promising in terms of the light collection efficiency, a serious problem is the rising background level induced by radioactive contaminants in the photo-sensors. Indeed, Monte Carlo simulations of the internal electron recoil background show, that the QUPIDs are the dominant source of background events. Consequently, the background level will limit the sensitivity of detectors with a large number of QUPIDs, unless the radiopurity can be improved. A similar observation can be made for detectors with fiducial mass of $10\,\mathrm{t}$ or more. Although the internal background from the detector components can be reduced by applying a stronger fiducial volume cut, we cannot reduce the intrinsic background from ^{85}Kr and solar pp-neutrinos. Consequently, it is impossible for liquid xenon detectors to observe dark matter with $\sigma_{\mathrm{p}}^{\mathrm{SI}} < 10^{-48}\,\mathrm{cm}^2$.

If the upcoming results from XENON100 do not confirm the observations from DAMA and CoGeNT, there will be a strong tension between the different experiments. For experimentalists, the challenge will be to understand the backgrounds in the detector very well and provide a convincing analysis of the detector acceptance. For theoretical physicists, the most interesting question will be, whether the results from the different experiments are necessarily in contradiction with each other, or whether the data point towards a novel interpretation of dark matter that allows to reconcile all experiments.

As a first step in this direction, we have performed in chapter 6 a general operator analysis of all possible interactions between fermionic dark matter particles and

quarks. The challenge is to infer the dark matter-nucleus interaction from the fundamental couplings and then calculate the resulting cross sections in the non-relativistic limit. For a few cases, these calculations are well known, giving the standard results for spin-independent and spin-dependent interactions. In many cases, however, new operators may appear in the matching process, and for each of these new operators we have to determine the effective coupling constants and form factors from models of the nucleus.

We have decided to consider also subleading contributions, which are usually neglected but lead to interesting experimental signatures if the leading order terms are absent. For all possible four-fermion interactions of dimension four and five, we have calculated the matrix elements in the non-relativistic limit. It turns out, that for certain combinations of fermion bilinears, the resulting cross sections may depend on the momentum transfer in the scattering process as well as on the velocity of the incoming dark matter particle. Such dependences allow for example to suppress scattering with low momentum transfer, similar to the case of inelastic dark matter [25].

Clearly, much work remains to be done. Concerning the data analysis of XENON100, we believe that detailed Monte Carlo simulations of the nuclear recoil band in XENON100 will play an essential part in determining the acceptance of the single scatter cut and the nuclear recoil cut, which will be necessary for a consistent interpretation of the final results. In addition, such simulations may improve our understanding of the data obtained from AmBe calibration and could even provide a way to determine the scintillation and ionization yields (see [34]).

To check our results for $\mathcal{L}_{\text{eff}}$, it would be very helpful to perform an ab-initio analysis of atomic collisions, including the calculation of exclusive cross sections, as well as a Monte Carlo simulation of the recombination processes. Such an analysis should take into account the electronic structure of the outer electron shells of xenon (for example, using Density Functional Theory). Alternatively, the cross sections could be determined experimentally from the collisions of individual xenon atoms. The final confirmation of our model can of course only come from precise measurements of the ionization yield and the relative scintillation efficiency.

Concerning the studies of future detectors, we suggest to consider thoroughly possible design changes in order to improve the light collection efficiency or reduce the background level. Important questions related to XENON1T will concern the cryostat material and the choice between QUPIDs and ordinary PMTs. The code that we developed may help to make these decisions. Moreover, to complement our simulations of the electron recoil background, a similar study for neutron background needs to be performed. Also, we would like to emphasize the importance of liquid xenon purification for the sensitivity of future detectors — to increase the absorption length and reduce the intrinsic background from ^{85}Kr.

The next steps towards a theoretical understanding of dark matter should include a careful evaluation of the coupling constants and form factors that appear in the

process of matching quark operators to nucleus operators. For the step from quarks to nucleons, these calculations will rely strongly on QCD, while the step from nucleons to nuclei requires a precise model of the nucleus. The subsequent step will then be to see whether any of the new operators that appear at subleading order may reconcile all experimental observations.

In conclusion, there are exciting times ahead for the physics of dark matter. We expect the publication of the results from XENON100 in the near future, and in the following years the competition for the first detector of the next generation (with a fiducial mass of more than 1 t). At the same time, the interpretation of the experimental results will require the ingenuity of theoretical physicists to solve the dark matter puzzle.

The increase in sensitivity that is expected for the dark matter searches within the next decade, combined with the results from the LHC, may very well lead to an unambiguous identification of dark matter. On the other hand, experiments may observe nothing at all — or reveal something completely unexpected. Clearly, we must remain open-minded for unconventional interpretations and new insights (see figure 7.1).
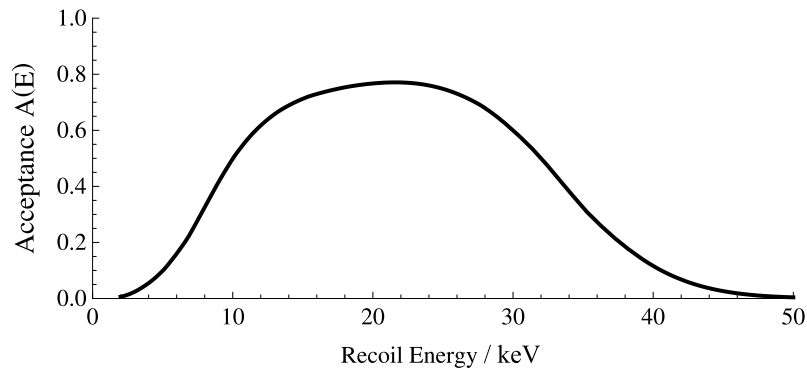
(a) Typical total acceptance function for a liquid xenon detector.
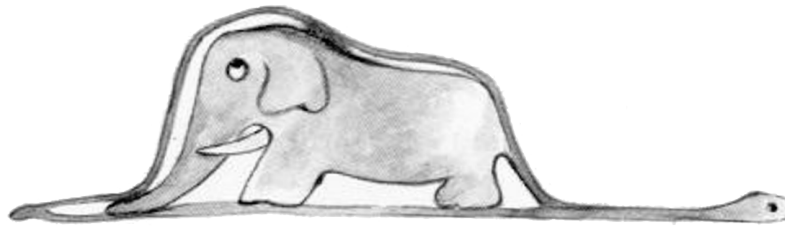
(b) "It was a picture of a boa constrictor digesting an elephant."

Figure 7.1: What will future direct detection experiments reveal about the nature of dark matter? An interpretation of the total acceptance function of a liquid xenon detector in the spirit of Antoine de Saint-Exupéry's *Little Prince* [91].

The Dirac equation

The Dirac equation is the equation of motion for spin-$1/2$ particles, which are described by four-component Dirac spinors ψ:

$$\left(i\gamma^\mu\partial_\mu - m\right)\psi = 0 \ . \tag{A.1}$$

The 4×4 matrices γ^μ satisfy the Clifford algebra

$$\{\gamma^\mu, \gamma^\nu\} = 2g^{\mu\nu} \ , \tag{A.2}$$

where $g^{\mu\nu}$ is the metric tensor. We adopt the sign convention $(+, -, -, -)$.

For the γ-matrices, we take the chiral representation,

$$\gamma^\mu = \begin{pmatrix} 0 & \sigma^\mu \\ \overline{\sigma}^\mu & 0 \end{pmatrix} \ , \qquad\qquad \gamma^5 = i\gamma^0\gamma^1\gamma^2\gamma^3 = \begin{pmatrix} -\mathbb{1} & 0 \\ 0 & \mathbb{1} \end{pmatrix} \ , \tag{A.3}$$

with $\sigma = (\mathbb{1}, \boldsymbol{\sigma})$ and $\overline{\sigma} = (\mathbb{1}, -\boldsymbol{\sigma})$. $\mathbb{1}$ is the 2×2 identity matrix and the σ^i are the Pauli matrices

$$\sigma^1 = \begin{pmatrix} 0 & 1 \\ 1 & 0 \end{pmatrix} \ , \qquad \sigma^2 = \begin{pmatrix} 0 & -i \\ i & 0 \end{pmatrix} \ , \qquad \sigma^3 = \begin{pmatrix} 1 & 0 \\ 0 & -1 \end{pmatrix} \ . \tag{A.4}$$

The Pauli matrices are hermitian and traceless and have the property that

$$\left\{\sigma^i, \sigma^j\right\} = 2\delta^{ij} \ , \qquad\qquad \left[\sigma^i, \sigma^j\right] = 2i\epsilon^{ijk}\sigma_k \ , \tag{A.5}$$

with the Kronecker symbol δ^{ij} and the Levi-Civita symbol ϵ^{ijk}. Consequently,

$$\sigma^i\sigma^j = \delta^{ij} + i\epsilon^{ijk}\sigma_k \ , \tag{A.6}$$

$$\mathrm{tr}\left(\sigma^i\sigma^j\right) = \delta^{ij} \ , \tag{A.7}$$

$$\left(\boldsymbol{p} \cdot \boldsymbol{\sigma}\right)^2 = \mathbb{1}\boldsymbol{p}^2 \ . \tag{A.8}$$

To solve the Dirac equation for a particle with four-momentum $p = (E, \boldsymbol{p})$ and mass $m = \sqrt{p^2}$, we introduce a normalized two-component spinor ξ and write

$$\psi(p) = \frac{1}{\sqrt{2m}} \, \mathrm{e}^{-ip \cdot x} \begin{pmatrix} \sqrt{p \cdot \sigma} \xi \\ \sqrt{p \cdot \overline{\sigma}} \xi \end{pmatrix} . \tag{A.9}$$

With this ansatz, we get

$$\gamma^\mu \partial_\mu \psi = -\frac{i}{\sqrt{2m}} \, \mathrm{e}^{ip \cdot x} \, \gamma^\mu p_\mu \begin{pmatrix} \sqrt{p \cdot \sigma} \xi \\ \sqrt{p \cdot \overline{\sigma}} \xi \end{pmatrix} \tag{A.10}$$

$$= -\frac{i}{\sqrt{2m}} \, \mathrm{e}^{ip \cdot x} \begin{pmatrix} 0 & p \cdot \sigma \\ p \cdot \overline{\sigma} & 0 \end{pmatrix} \begin{pmatrix} \sqrt{p \cdot \sigma} \xi \\ \sqrt{p \cdot \overline{\sigma}} \xi \end{pmatrix} \tag{A.11}$$

$$= -\frac{i}{\sqrt{2m}} \, \mathrm{e}^{ip \cdot x} \begin{pmatrix} p \cdot \sigma \sqrt{p \cdot \overline{\sigma}} \xi \\ p \cdot \overline{\sigma} \sqrt{p \cdot \sigma} \xi \end{pmatrix} . \tag{A.12}$$

Now we use

$$\sqrt{p \cdot \sigma} \sqrt{p \cdot \overline{\sigma}} = \sqrt{(\mathbb{1} - \boldsymbol{p\sigma})(\mathbb{1} + \boldsymbol{p\sigma})} \tag{A.13}$$

$$= \sqrt{\mathbb{1}^2 - (\boldsymbol{p\sigma})^2} = \mathbb{1}\sqrt{1 - \boldsymbol{p}^2} = \mathbb{1}\sqrt{p^2} = \mathbb{1}m \, , \tag{A.14}$$

to get $\gamma^\mu \partial_\mu \psi(p) = -im\psi(p)$. Consequently, $\psi(p)$ as defined in equation (A.9) satisfies the Dirac equation. To simplify notation, we define $\not{p} \equiv \gamma^\mu p_\mu$. The Dirac equation then implies that

$$\not{p}\psi(p) = m\psi(p) \, . \tag{A.15}$$

To conclude this appendix, we note that the Dirac equation can be derived from a Lorentz-invariant Lagrangian density

$$\mathcal{L} = \overline{\psi} \left(i\gamma^\mu \partial_\mu + m \right) \psi \, , \tag{A.16}$$

where $\overline{\psi} = \psi^\dagger \gamma^0$. Note that, in contrast to [79], we have chosen the non-relativistic normalization for ψ. Thus, in our normalization,

$$\overline{\psi}(p)\psi(p) = \frac{1}{2m} \begin{pmatrix} \xi^\dagger \sqrt{p \cdot \sigma}, & \xi^\dagger \sqrt{p \cdot \overline{\sigma}} \end{pmatrix} \begin{pmatrix} 0 & 1 \\ 1 & 0 \end{pmatrix} \begin{pmatrix} \sqrt{p \cdot \sigma} \xi \\ \sqrt{p \cdot \overline{\sigma}} \xi \end{pmatrix} \tag{A.17}$$

$$= \frac{1}{2m} \left(\xi^\dagger \sqrt{p \cdot \overline{\sigma}} \sqrt{p \cdot \sigma} \xi + \xi^\dagger \sqrt{p \cdot \sigma} \sqrt{p \cdot \overline{\sigma}} \xi \right) = \xi^\dagger \xi = 1 \, . \tag{A.18}$$

APPENDIX B
Calculation of exclusion limits

In this appendix, we discuss how to calculate exclusion limits for dark matter direct detection experiments. Such exclusion limits are conventionally calculated under the assumption that no background events are observed. If the experiment does in the end observe background events, the exclusion limits will be weaker. In this case, one needs to use more sophisticated methods — such as the Maximum Gap Method [72] — for the calculation.

In principle, to determine whether an experiment can exclude a choice of the parameters $\sigma_{\mathrm{p}}^{\mathrm{SI}} = \sigma_0$ and $m_\chi = m_0$, we must calculate the total number of events that the experiment is expected to observe for this combination. To do so, we must calculate the differential event rate for these parameters as described in chapter 2.1.

Of course, not all dark matter scattering events will result in a detectable signal, so we must multiply the differential event rate with the total acceptance function of the detector, $A(E_{\mathrm{nr}})$, which we introduce in chapter 3.4. The acceptance function gives the probability that a nuclear recoil of energy E_{nr} leads to a signal in the detector. It takes into account the detector resolution, the light yield and the cut acceptances of the detector (see chapter 3 for a discussion).

Once we have determined the total acceptance function, we can obtain the total event rate by integrating

$$R_{\mathrm{tot}} = \int\limits_0^\infty \frac{\mathrm{d}R}{\mathrm{d}E_{\mathrm{nr}}} A(E_{\mathrm{nr}}) \ . \tag{B.1}$$

Multiplying R_{tot} with the exposure of the experiment now gives the *total number of expected events N*.

Assuming that instead of the expected number of events N, the detector will observe no event at all, we can reject the hypothesis $\sigma_{\mathrm{p}}^{\mathrm{SI}} = \sigma_0$ and $m_\chi = m_0$, if N is sufficiently large. If $N > 2.30$, we can reject the hypothesis with 90% confidence and if $N > 3.00$ the hypothesis is ruled out with 95% confidence [10]. Consequently, 90% confidence exclusion limits, as shown for example in chapter 5 are obtained by calculating all combinations of m_χ and $\sigma_{\mathrm{p}}^{\mathrm{SI}}$ that give $N = 2.30$.

APPENDIX C

Coulomb correction to electronic stopping

For a uniform electron gas the electronic stopping power is proportional to the velocity of the ionizing particle, as stated in equation (4.5). The same result is also valid for liquid scintillators, if the velocity of the passing atom is comparable to the Bohr velocity. However, at very low velocities, colliding atoms do not penetrate each other strongly because of the Coulomb repulsion. In this case, the nucleus passes only through regions of low electron density and consequently experiences a smaller stopping force. As a result, we expect a stronger decrease of the electronic stopping power. This effect has been referred to as the Coulomb correction to Lindhard's theory [53].

It is not clear how to include this correction into the calculation of electronic stopping powers. In reference [43], Tilinin suggested to calculate S_e by integrating dE/dx over the volume accessible for a recoiling nucleus and multiplying the result with the number density of xenon atoms. Following this approach, we obtain from equation (4.5)

$$
S_e = \int\limits_{V_{\text{acc}}} N n_0 v v_{\text{F}} \sigma_{\text{tr}}(v_{\text{F}}) \, dV = N m_e v \int\limits_{V_{\text{acc}}} n(\boldsymbol{r}) v_{\text{F}}(\boldsymbol{r}) \sigma_{\text{tr}} \left(v_{\text{F}}(\boldsymbol{r}) \right) \, dV \, , \qquad (\text{C.1})
$$

where $n = n_0/m_e$ is the number density of electrons. Before we can evaluate this integral, we must determine V_{acc}, $n(\boldsymbol{r})$, $v_{\text{F}}(\boldsymbol{r})$ and $\sigma_{\text{tr}}(v)$.

To obtain the accessible volume, we need to know the interaction potential $V(r)$ for two xenon atoms. This potential has been calculated by Schneider [92] based on a Density Functional Theory calculation done by Gordon and Kim [93]. In a collision process with energy E_{nr}, the distance of closest approach, $r_0(E_{\text{nr}})$, is given by the root of the equation $V(r_0) = E_{\text{nr}}$. The accessible volume V_{acc} is then given by all points with $r \geq r_0$. As expected, r_0 is a function of E_{nr}, which decreases with increasing recoil energy, so the accessible volume will grow.

To simplify the integral in equation (C.1), we assume that the electron density is radially symmetric. Of course, this assumption will not hold strictly, as two atoms approach each other, but it is a good approximation at low energies, when the atoms

stay rather far apart and most of the nuclear charge is screened by inner electrons.[1]
We will therefore replace $n(\boldsymbol{r})$ by the electron density $n(r)$ of a single xenon atom
that Ziegler et al. calculated with Hartree-Fock methods [56].

For a uniform electron gas, we can calculate the Fermi velocity from the electron
density:

$$v_{\mathrm{F}} = \frac{1}{m_e} \sqrt[3]{3n\pi^2} \ . \tag{C.2}$$

In our case, we have a non-uniform electron density, so the Fermi velocity will be
slightly larger [47]:

$$\tilde{v}_{\mathrm{F}}^2 = v_{\mathrm{F}}^2 + \frac{1}{4} \left(a_0 n'(r)/n(r) \right)^2 \ . \tag{C.3}$$

We will, however, neglect this effect in the following, assuming that $n'(r) \ll n(r)/a_0$
and use the approximation of a uniform electron gas.

Finally, the transport cross section σ_{tr} has been calculated by Tilinin in [94].
Consequently, we know all quantities that appear in equation (C.1) and can calculate
the electronic stopping power numerically. Under the assumption of a radially
symmetric electron distribution, we can write

$$S_{\mathrm{e}} = 4\pi N m_e v \int\limits_{r_0}^{\infty} n(r) v_{\mathrm{F}}(r) \sigma_{\mathrm{tr}}(v_{\mathrm{F}}(r)) r^2 \, \mathrm{d}r \ . \tag{C.4}$$

For convenience, we define the dimensionless quantities $x = r/a$ and $T = \sigma_{\mathrm{tr}}/\pi a^2$
and get

$$S_{\mathrm{e}} = 4\pi N m_e v \int\limits_{r_0}^{\infty} n(r) v_{\mathrm{F}}(r) \sigma_{\mathrm{tr}}(v_{\mathrm{F}}) r^2 \, \mathrm{d}r \tag{C.5}$$

$$= 4\pi^2 N m_e v a^5 \int\limits_{x_0}^{\infty} n(x) v_{\mathrm{F}}(x) T(v_{\mathrm{F}}(x)) x^2 \, \mathrm{d}x \tag{C.6}$$

$$= 4\pi^2 N m_e \frac{v}{v_0} e^2 a^4 \frac{1}{4\sqrt{2}} \sqrt[3]{\frac{9\pi^2}{2Z}} a_0 \int\limits_{x_0}^{\infty} n(x) v_{\mathrm{F}}(x) T(v_{\mathrm{F}}(x)) x^2 \, \mathrm{d}x \tag{C.7}$$

$$= \sqrt{8}\pi N e^2 a_0 \frac{v}{v_0} a^4 \frac{\pi^2}{2} \sqrt[3]{\frac{27\pi}{16Z}} \int\limits_{x_0}^{\infty} n(x)^{4/3} T(v_{\mathrm{F}}(x)) x^2 \, \mathrm{d}x \tag{C.8}$$

$$\equiv \sqrt{8}\pi N e^2 a_0 \frac{v}{v_0} \tau(E_{\mathrm{nr}}) \ , \tag{C.9}$$

---

[1]More precisely, radial symmetry should be a valid approximation, if r_0 is greater than the
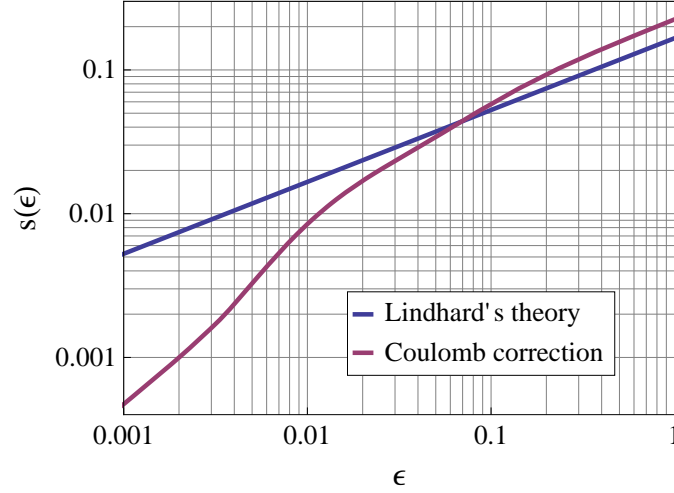Thomas-Fermi screening length a.

Figure C.1: The final result for the dimensionless electronic stopping power $d\epsilon/d\rho$.

where we made use of $a = \frac{1}{4\sqrt{2}} \sqrt[3]{\frac{9\pi^2}{2Z}} a_0$.

The final result has been written in a way that for constant $\tau(E_{\mathrm{nr}})$ we recover a velocity proportional stopping power. In fact, for $\tau(E_{\mathrm{nr}}) \approx 100$, our result coincides with the result from Lindhard's theory. Such a constant value for $\tau(E_{\mathrm{nr}})$ indeed occurs for $v \geq v_0$, because at very small distances, the Fermi velocity is large and the transport cross section becomes negligibly small. We present the result of our calculation in figure C.1, again using the reduced units defined in equation (4.9).

We observe that Tilinin's approach for the Coulomb correction predicts an electronic stopping power that drops rapidly below 100 keV. At 10 keV the corrected stopping power is already a factor of two smaller than the original result from Lindhard. It should be clear from the discussion in chapter 4 that there is no way to explain a rising ionization yield at low energies with this model.

We must conclude that the results for the electronic stopping power derived from equation (C.1) are in contradiction with experimental data. To resolve this contradiction, one could try a more accurate treatment and calculate the trajectories of xenon atoms during a scattering process in order to integrate the electronic stopping power along the path. Tilinin argues, however, that for small angle scattering, which is the most likely to occur at low energies, the volume integral in equation (C.1) should give the same result.

As argued in chapter 4, there appears to be no naive way to include the Coulomb correction to the electronic stopping power. Probably, the assumption of a point-like interaction between nucleus and electron is no longer valid at very low velocities, because the electron cloud can rearrange during the collision. A possible way to account for this effect may be time-dependent Density Functional Theory as described in [95].

Details on the Monte Carlo simulations with Geant4

All simulations have been performed with MaGe [96], a Monte Carlo framework for experiments with low background based on Geant4 [97]. The general structure of the code, the physics list and the event generator have been adapted from the corresponding simulations for XENON100 [32], while the detector design was changed completely and new features were added to improve the user interface.

D.1 Detector design

The detector design employed in our simulations is based on early proposals for XENON1T [70]. In detail it contains:

- A liquid xenon time projection chamber (TPC) that is surrounded by a teflon (PTFE) layer for the reflection of scintillation light,

- A titanium cryostat consisting of an inner and outer vessel with vacuum between them,

- A layer of acrylic (PMMA) that separates the cryostat vessel from the PTFE layer,

- QUPIDs (see section D.2) on the bottom and top of the TPC, placed on a support base made of copper,

- Stainless steel grids for the drift field and the extraction field.

Note that several simplifications have been made and some recent changes in the design are not included.[1] Since this thesis is only concerned with internal electron recoil background, there is no need to include the water shield into the simulation.

---

[1]Most notably, the field shaping rings are not included in the simulation. Also, the XENON collaboration has recently proposed to separate the flange for inner and outer vessel to reduce heat transfer.

Component	Unit	TPC diameter and height in meter				
		1.0	1.2	1.4	1.6	1.8
Liquid Xenon	kg	2291	3958	6286	9383	13360
Titanium	kg	337	447	573	714	870
PTFE	kg	148	241	368	535	742
Copper	kg	155	215	284	363	451
PMMA	kg	198	273	360	459	570
QUPIDs	piece	242	374	508	628	842

Table D.1: Masses of the various detector components (in kg) for different TPC sizes

The main virtue of our code is that the detector dimensions are not fixed. The height and diameter of the TPC can be varied independently, allowing to study larger detectors as well as detectors with a novel design (see chapter 5.3). As the TPC dimensions are changed, the program rescales the relevant parts of the detector, such as the size of the cryostat. Other parts remain fixed, for example the drift gap in the gas phase. The QUPIDs also have a fixed size, but their number increases with larger diameter. The appropriate number of QUPIDs and their placement on a hexagonal grid is automatically determined by the code. For concreteness, we show two examples of different detector dimensions in figure D.1 and give a list of the component masses for some typical choices in table D.1.

D.2 Material properties

D.2.1 QUPIDs

For future experiments, the XENON Collaboration plans to use a newly developed photo-sensor, called QUPID (Quartz Photon Intensifying Detector). The photoelectrons produced in a QUPID are accelerated to 6 keV and focused onto an Avalanche PhotoDiode. QUPIDs are expected to have extremely low radioactivity, a good transparency and a quantum efficiency of $QE > 30\%$ [98]. A schematical drawing of the QUPID design is shown in figure D.2.

D.2.2 Optical properties

In order to determine the light collection efficiency, we need to include the optical properties in the vacuum-ultraviolet (vuv) region for all materials. While the refractive indices are well known, the greatest uncertainty comes from the PTFE reflectivity, which we assumed to equal 0.95. The reflectivity for copper was assumed to equal 0.2. Another important property is the optical transparency of the grid,
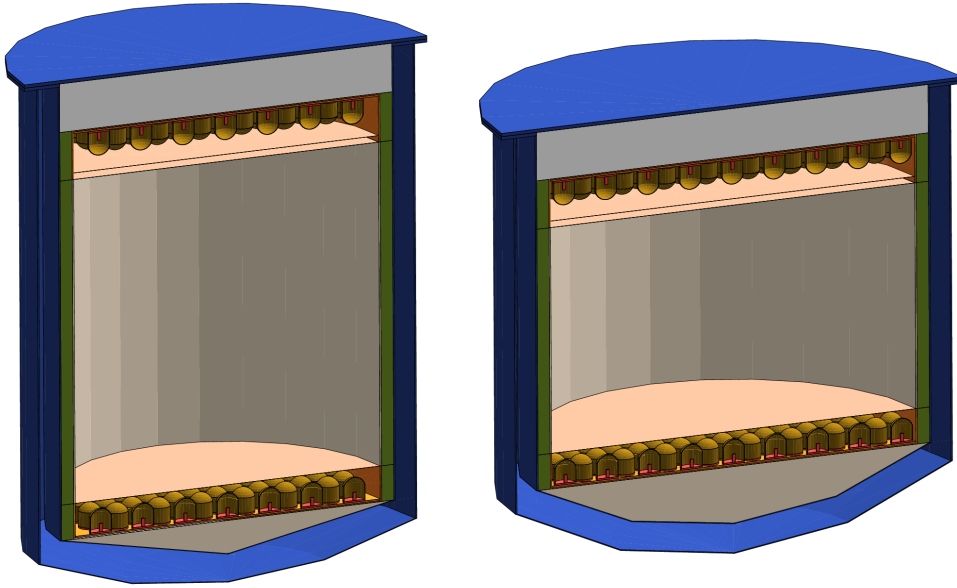
Figure D.1: Examples of the detector design. In both cases, the detector has a fiducial volume of 1 t. While the left one corresponds to the conventional design with equal height and diameter, the right one has a larger diameter to increase the number of QUPIDs and improve the light collection efficiency (see chapter 5.3).
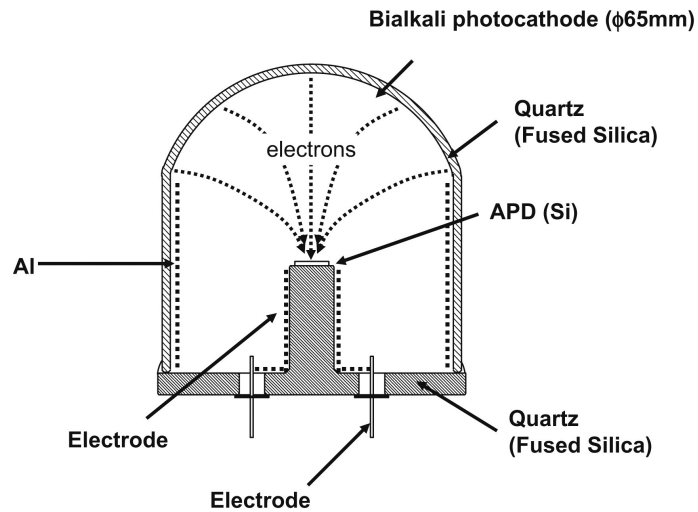

Figure D.2: A scematical drawing of the design of a QUPID. Figure taken from [98].

Component	Unit	Radioactivity in mBq/unit			
		^{238}U	^{232}Th	^{40}K	^{60}Co
Titanium	kg	0.25	0.2	1.3	–
PTFE	kg	0.31	0.16	2.2	0.11
Copper	kg	0.07	0.03	0.5	0.0045
QUPIDs	piece	0.49	0.4	2.4	0.21

Table D.2: Assumed radioactivity for the various components of the detector. The radioactivity of the PMMA is negligible.

which we took to be 0.94, the value from XENON100.[1] For liquid xenon, the optical properties depend on the achieved purity and therefore we keep them as free parameters that can be changed during the simulation.

D.2.3 Radioactivity

For the simulation of internal electron recoil background, we need to make assumptions on the radioactivity of all materials in the detector. These materials have been screened by the XENON Collaboration. In most cases only upper limits are known, but we adapt these values for our simulation. Should the radioactivity turn out to be much lower, the background level can simply be rescaled accordingly. For an overview of the assumed radioactivities, see table D.2.

D.3 Simulation details

D.3.1 Simulation of scintillation light

To simulate scintillation light, we generate a large number of primary scintillation photons at a given position inside the liquid xenon. The photons are traced until they are either absorbed (by the PTFE, the copper, the grids or the liquid xenon itself) or hit a QUPID. This process is repeated many times to determine the average number of photons that reach the QUPID arrays. If we allow the position of the primary scintillation photons to vary randomly, we can also determine the average light collection efficiency of the detector.

D.3.2 Simulation of radioactivity

To simulate radioactivity, one must select a detector component, a radioactive isotope and set a period of time. Based on the assumed radioactivity shown in table D.2,

---

[1]The XENON Collaboration aims to improve the transparency and reach 0.97 in XENON1T.

the program calculates the expected number of decays. Each decay is simulated by placing a radioactive atom at a random position within the selected detector component. The decay products are simulated until their energy falls below the simulation threshold.[1] Whenever energy is deposited inside the active volume, the event is written into a ROOT-file [99].

In a second step, we scan the ROOT-file to look for single-scatter events. This step is very important, because events that deposit their energy in the liquid xenon in more than one step can be easily distinguished from potential dark matter signals and do not contribute to the background. At this point we must take the position resolution (typically 3 mm) of the detector into account. Two events that are separated by a distance less than the position resolution will be indistinguishable experimentally and consequently should be treated as one event.

Finally, we apply the fiducial volume cut and select the events in the relevant energy region. Note that due to the suppression of scintillation light for nuclear recoils, a nuclear recoil energy of 10 keV corresponds to the same amount of scintillation light as a 2 keV electron recoil. Consequently, the dark matter search window ($4 \leq S1 \leq 20$) translates to roughly $2 \text{ keVee} \leq E_{\text{er}} \leq 11 \text{ keVee}$ for electron recoils.

In the end, we are left with a very small number of events: Only about one out of a million decays will give an event that passes all selection criteria. Consequently, we need to simulate very large numbers of decays. To obtain a reasonable estimate of the background expected in a runtime of one year, we must generate up to 10^9 primary events.

---

[1]To simulate the decay chains of ^{238}U and ^{232}Th, the procedure is slightly more complicated: For each event, the program chooses randomly an isotope from the decay chain and simulates its decay products, instantly removing the daughter isotope without further decays. Consequently, to simulate 100 decays of ^{238}U we have to simulate (on average) 1400 decays, in order to include the decays of the 13 daughter isotopes as well.

Bibliography

[1] G. Bertone, D. Hooper, and J. Silk, "*Particle dark matter: Evidence, candidates and constraints*", Phys. Rept. **405** (2005) 279–390, `arXiv:hep-ph/0404175`.

[2] K. A. Olive, "*Dark matter*", `arXiv:astro-ph/0301505`.

[3] P. F. Sorensen, *A Position-Sensitive Liquid Xenon Time-Projection Chamber for Direct Detection of Dark Matter: The XENON10 Experiment.* PhD thesis, Brown University, 2008.

[4] S. M. Carroll, "*Lecture notes on general relativity*", `arXiv:gr-qc/9712019`.

[5] K. G. Begeman, A. H. Broeils, and R. H. Sanders, "*Extended rotation curves of spiral galaxies: Dark haloes and modified dynamics*", Mon. Not. Roy. Astron. Soc. **249** (1991) 523.

[6] D. Clowe *et al.*, "*A direct empirical proof of the existence of dark matter*", Astrophys. J. **648** (2006) L109–L113, `arXiv:astro-ph/0608407`.

[7] E. Komatsu *et al.*, "*Seven-Year Wilkinson Microwave Anisotropy Probe (WMAP) Observations: Cosmological Interpretation*", `arXiv:1001.4538 [astro-ph.CO]`.

[8] J. L. Feng, "*Dark Matter Candidates from Particle Physics and Methods of Detection*", `arXiv:1003.0904 [astro-ph.CO]`.

[9] J. I. Collar, "*Light WIMP Searches: The Effect of the Uncertainty in Recoil Energy Scale and Quenching Factor*", `arXiv:1010.5187 [astro-ph.IM]`.

[10] **Particle Data Group** Collaboration, K. Nakamura, "*Review of particle physics*", J. Phys. **G37** (2010) 075021.

[11] G. Jungman, M. Kamionkowski, and K. Griest, "*Supersymmetric dark matter*", Phys. Rept. **267** (1996) 195–373, `arXiv:hep-ph/9506380`.

[12] D. G. Cerdeno and A. M. Green, "*Direct detection of WIMPs*", `arXiv:1002.1912 [astro-ph.CO]`.

[13] J. D. Lewin and P. F. Smith, "*Review of mathematics, numerical factors, and corrections for dark matter experiments based on elastic nuclear recoil*", Astropart. Phys. **6** (1996) 87–112.

[14] J. Kopp, T. Schwetz, and J. Zupan, "*Global interpretation of direct Dark Matter searches after CDMS-II results*", JCAP **1002** (2010) 014, `arXiv:0912.4264 [hep-ph]`.

[15] C. McCabe, "*The Astrophysical Uncertainties Of Dark Matter Direct Detection Experiments*", Phys. Rev. **D82** (2010) 023530, `arXiv:1005.0579 [hep-ph]`.

[16] A. M. Green, "*Dependence of direct detection signals on the WIMP velocity distribution*", `arXiv:1009.0916 [astro-ph.CO]`.

[17] **The CDMS-II** Collaboration, Z. Ahmed *et al.*, "*Dark Matter Search Results from the CDMS II Experiment*", Science **327** (2010) 1619–1621, `arXiv:0912.3592 [astro-ph.CO]`.

[18] **XENON** Collaboration, J. Angle *et al.*, "*First Results from the XENON10 Dark Matter Experiment at the Gran Sasso National Laboratory*", Phys. Rev. Lett. **100** (2008) 021303, `arXiv:0706.0039 [astro-ph]`.

[19] **CoGeNT** Collaboration, C. E. Aalseth *et al.*, "*Results from a Search for Light-Mass Dark Matter with a P-type Point Contact Germanium Detector*", `arXiv:1002.4703`.

[20] **KIMS** Collaboration, H. S. Lee *et al.*, "*Limits on WIMP-nucleon cross section with CsI(Tl) crystal detectors*", Phys. Rev. Lett. **99** (2007) 091301, `arXiv:0704.0423 [astro-ph]`.

[21] **COUPP** Collaboration, E. Behnke *et al.*, "*Improved Spin-Dependent WIMP Limits from a Bubble Chamber*", Science **319** (2008) 933–936, `arXiv:0804.2886 [astro-ph]`.

[22] S. Archambault *et al.*, "*Dark Matter Spin-Dependent Limits for WIMP Interactions on 19-F by PICASSO*", Phys. Lett. **B682** (2009) 185–192, `arXiv:0907.0307 [hep-ex]`.

[23] V. N. Lebedenko *et al.*, "*Result from the First Science Run of the ZEPLIN-III Dark Matter Search Experiment*", Phys. Rev. **D80** (2009) 052010, `arXiv:0812.1150 [astro-ph]`.

[24] G. Angloher *et al.*, "*Commissioning Run of the CRESST-II Dark Matter Search*", `arXiv:0809.1829 [astro-ph]`.

[25] D. Tucker-Smith and N. Weiner, "*Inelastic dark matter*", Phys. Rev. **D64** (2001) 043502, `arXiv:hep-ph/0101138`.

[26] **DAMA** Collaboration, R. Bernabei *et al.*, "*First results from DAMA/LIBRA and the combined results with DAMA/NaI*", Eur. Phys. J. **C56** (2008) 333–355, `arXiv:0804.2741 [astro-ph]`.

[27] R. Bernabei *et al.*, "*Possible implications of the channeling effect in NaI(Tl) crystals*", Eur. Phys. J. **C53** (2008) 205–213, `arXiv:0710.0288 [astro-ph]`.

[28] D. Hooper, J. I. Collar, J. Hall, and D. McKinsey, "*A Consistent Dark Matter Interpretation For CoGeNT and DAMA/LIBRA*", `arXiv:1007.1005 [hep-ph]`.

[29] E. Aprile and T. Doke, "*Liquid xenon detectors for particle physics and astrophysics*", Reviews of Modern Physics **82** (2010) 2053–2097, `arXiv:0910.4956 [physics.ins-det]`.

[30] **XENON100** Collaboration, E. Aprile *et al.*, "*First Dark Matter Results from the XENON100 Experiment*", Phys. Rev. Lett. **105** (2010) 131302, `arXiv:1005.0380 [astro-ph.CO]`.

[31] C. Savage, G. Gelmini, P. Gondolo, and K. Freese, "*XENON10/100 dark matter constraints in comparison with CoGeNT and DAMA: examining the Leff dependence*", `arXiv:1006.0972 [astro-ph.CO]`.

[32] **XENON** Collaboration, E. Aprile *et al.* Private communication.

[33] A. Manzur *et al.*, "*Scintillation efficiency and ionization yield of liquid xenon for mono-energetic nuclear recoils down to 4 keV*", Phys. Rev. **C81** (2010) 025808, `arXiv:0909.1063 [physics.ins-det]`.

[34] P. Sorensen, "*A coherent understanding of low-energy nuclear recoils in liquid xenon*", `arXiv:1007.3549`.

[35] F. Arneodo *et al.*, "*Scintillation efficiency of nuclear recoil in liquid xenon*", Nucl. Instrum. Meth. **A449** (2000) 147–157.

[36] D. Akimov *et al.*, "*Measurements of scintillation efficiency and pulse-shape for low energy recoils in liquid xenon*", Phys. Lett. **B524** (2002) 245–251, `arXiv:hep-ex/0106042`.

[37] E. Aprile *et al.*, "*Scintillation response of liquid xenon to low energy nuclear recoils*", Phys. Rev. **D72** (2005) 072006, `arXiv:astro-ph/0503621`.

[38] V. Chepel *et al.*, "*Scintillation efficiency of liquid xenon for nuclear recoils with the energy down to 5 keV*", Astropart. Phys. **26** (2006) 58–63.

[39] E. Aprile *et al.*, "*Simultaneous Measurement of Ionization and Scintillation from Nuclear Recoils in Liquid Xenon as Target for a Dark Matter Experiment*", Phys. Rev. Lett. **97** (2006) 081302, `arXiv:astro-ph/0601552`.

[40] P. Sorensen *et al.*, "*The scintillation and ionization yield of liquid xenon for nuclear recoils*", Nucl. Instrum. Meth. **A601** (2009) 339–346, `arXiv:0807.0459 [astro-ph]`.

[41] E. Aprile *et al.*, "*New Measurement of the Relative Scintillation Efficiency of Xenon Nuclear Recoils Below 10 keV*", Phys. Rev. **C79** (2009) 045807, `arXiv:0810.0274 [astro-ph]`.

[42] A. Hitachi, T. Doke, and A. Mozumder, "*Luminescence quenching in liquid argon under charged-particle impact – relative scintillation yield at different linear energy transfers*", Physical Review B **46** (1992) no. 18, 11463–11470.

[43] I. Tilinin, "*Quasi-classical expression for inelastic energy-losses in atomic particle collisions below the Bohr velocity*", Physical Review A **51** (1995) no. 4, 3058–3065.

[44] J. Valdes, J. Eckardt, G. Lantschner, and N. Arista, "*Energy-loss of slow protons in solids - deviation from the proportionality with projectile velocity*", Physical Review A **49** (1994) no. 2, 1083–1088.

[45] P. Echenique, R. Nieminen, J. Ashley, and R. Ritchie, "*Nonlinear stopping power of an electron-gas for slow ions*", Physical Review A **33** (1986) no. 2, 897–904.

[46] T. Ferrell and R. Ritchie, "*Energy-losses by slow ions and atoms to electronic excitation in solids*", Physical Review B **16** (1977) no. 1, 115–123.

[47] H. Winter, J. Juaristi, I. Nagy, A. Arnau, and P. Echenique, "*Energy loss of slow ions in a nonuniform electron gas*", Physical Review B **67** (2003) no. 24, 245401.

[48] J. Lindhard and M. Scharff, "*Energy dissipation by ions in keV region*", Physical Review **124** (1961) no. 1, 128.

[49] O. Firsov, "*A qualitative interpretation of the mean electron excitation energy in atomic collisions*", Soviet Physics Jetp-Ussr **9** (1959) no. 5, 1076–1080.

[50] D. J. Ficenec, S. P. Ahlen, A. A. Marin, J. A. Musser, and G. Tarle,
"*Observation of electronic excitation by extremely slow protons with applications
to the detection of supermassive charged particles*", Phys. Rev. **D36** (1987)
311–314.

[51] J. Brenot, D. Dhuicq, J. Gauyacq, J. Pommier, V. Sidis, M. Barat, and
E. Pollack, "*Collisions between rare-gas atoms at low keV energies – Symmetric
Systems*", Physical Review A **11** (1975) no. 4, 1245–1266.

[52] S. Ovchinnikov, G. Ogurtsov, J. Macek, and Y. Gordeev, "*Dynamics of
ionization in atomic collisions*", Physics Reports-Review Section Of Physics
Letters **389** (2004) no. 3, 119–159.

[53] D. Semrad, "*Coulomb effect and threshold effect in electronic stopping power
for slow protons*", Physical Review A **33** (1986) no. 3, 1646–1652.

[54] P. Sigmund, "*Stopping Of Heavy Ions - A Theoretical Approach*", vol. 204 of
Springer Tracts In Modern Physics, pp. 1–5. Springer-Verlag Berlin, 2004.

[55] K. Winterbon, P. Sigmund, and J. Sanders, "*Spatial distribution of energy
deposited by atomic particles in elastic collisions*", Kongelige Danske
Videnskabernes Selskab, Matematisk-Fysiske Meddelelser **37** (1970) no. 14,
5–61.

[56] J. Ziegler, J. Biersack, and U. Littmark, *Stopping and range of ions in solids.*
Pergamon Press, New York, 1985.

[57] J. Lindhard, V. Nielsen, M. Scharff, and P. Thomsen, "*Integral equations
governing radiation effects*", Mat. Fys. Medd. Dan. Vid. Selsk. **33** (1963) no. 10,
1.

[58] C. Dahl, *The physics of background discrimination in liquid xenon, and first
results from Xenon10 in the hunt for WIMP dark matter.* PhD thesis,
Princeton University, 2009.

[59] R. Platzman, "*Total ionization in gases by high-energy particles - an appraisal
of our understanding*", International Journal Of Applied Radiation And
Isotopes **10** (1961) 116.

[60] U. Fano and W. Lichten, "*Interpretation of Ar^+–Ar Collisions at 50 KeV*",
Phys. Rev. Lett. **14** (1965) 627–629.

[61] R. Spicuzza and Q. Kessel, "*Ionization due to multiple n-shell and m-shell
excitation in penetrating collisions of 0.15-1.20 MeV Xe^+ with Xe*", Physical
Review A **14** (1976) no. 2, 630–637.

[62] M. Kimura and N. Lane, "*The low-energy, heavy-particle collisions – a close coupling treatment*", Advances In Atomic Molecular And Optical Physics **26** (1989) 79–160.

[63] A. Manalaysay, *Response of liquid xenon to low-energy ionizing radiation and its use in the XENON10 Dark Matter search*. PhD thesis, University of Zurich, 2010.

[64] **ICARUS** Collaboration, S. Amoruso *et al.*, "*Study of electron recombination in liquid argon with the ICARUS TPC*", Nucl. Instrum. Meth. **A523** (2004) 275–286.

[65] J. Thomas and D. A. Imel, "*Recombination of electron-ion pairs in liquid argon and liquid xenon*", Physical Review A **36** (1987) 614–616.

[66] A. Hitachi, "*Quenching factor and electronic LET in a gas at low energy*", J. Phys. Conf. Ser. **65** (2007) 012013.

[67] A. Hitachi, "*Properties of liquid xenon scintillation for dark matter searches*", Astropart. Phys. **24** (2005) 247–256.

[68] D.-M. Mei, Z.-B. Yin, L. Stonehill, and A. Hime, "*A Model of Nuclear Recoil Scintillation Efficiency in Noble Liquids*", Astropart. Phys. **30** (2008) 12–17, `arXiv:0712.2470 [nucl-ex]`.

[69] V. Tretyak, "*Semi-empirical calculation of quenching factors for ions in scintillators*", Astropart. Phys. **33** (2010) 40–53, `arXiv:0911.3041 [nucl-ex]`.

[70] **XENON** Collaboration, E. Aprile *et al.*, "*XENON1T at LNGS*". Proposal April 2010.

[71] K. Arisaka *et al.*, "*XAX: a multi-ton, multi-target detection system for dark matter, double beta decay and pp solar neutrinos*", Astropart. Phys. **31** (2009) 63–74, `arXiv:0808.3968 [astro-ph]`.

[72] S. Yellin, "*Finding an upper limit in the presence of unknown background*", Phys. Rev. **D66** (2002) 032005, `arXiv:physics/0203002`.

[73] **XMASS** Collaboration, K. Abe *et al.*, "*Distillation of Liquid Xenon to Remove Krypton*", `arXiv:0809.4413 [physics.ins-det]`.

[74] S. Lindemann, "*Reinigung und Nachweis von Edelgasen mit miniaturisierten Proportionalzählrohren*". Diploma thesis, University of Heidelberg, 2009.

[75] J. N. Bahcall, "*Gallium solar neutrino experiments: Absorption cross sections, neutrino spectra, and predicted event rates*", Phys. Rev. **C56** (1997) 3391–3409, `arXiv:hep-ph/9710491`.

[76] R. N. Mohapatra and P. B. Pal, "*Massive neutrinos in physics and astrophysics. Second edition*", World Sci. Lect. Notes Phys. **60** (1998) 1–397.

[77] A. Gutlein *et al.*, "*Solar and Atmospheric Neutrinos: Background Sources for the Direct Dark Matter Searches*", Astropart. Phys. **34** (2010) 90–96, `arXiv:1003.5530 [hep-ph]`.

[78] J. Fan, M. Reece, and L.-T. Wang, "*Non-relativistic effective theory of dark matter direct detection*", `arXiv:1008.1591 [hep-ph]`.

[79] M. E. Peskin and D. V. Schroeder, *An Introduction to quantum field theory*. Addison-Wesley, Reading, 1995.

[80] A. Kurylov and M. Kamionkowski, "*Generalized analysis of weakly-interacting massive particle searches*", Phys. Rev. **D69** (2004) 063503, `arXiv:hep-ph/0307185`.

[81] J. R. Ellis and R. A. Flores, "*Realistic prediction for the detection of supersymmetric dark matter*", Nucl. Phys. **B307** (1988) 883.

[82] J. Engel, "*Nuclear form-factors for the scattering of weakly interacting massive particles*", Phys. Lett. **B264** (1991) 114–119.

[83] M. T. Ressell and D. J. Dean, "*Spin-dependent neutralino nucleus scattering for A approx. 127 nuclei*", Phys. Rev. **C56** (1997) 535–546, `arXiv:hep-ph/9702290`.

[84] H. An, S.-L. Chen, R. N. Mohapatra, S. Nussinov, and Y. Zhang, "*Energy Dependence of Direct Detection Cross Section for Asymmetric Mirror Dark Matter*", Phys. Rev. **D82** (2010) 023533, `arXiv:1004.3296 [hep-ph]`.

[85] A. L. Fitzpatrick and K. M. Zurek, "*Dark Moments and the DAMA-CoGeNT Puzzle*", Phys. Rev. **D82** (2010) 075004, `arXiv:1007.5325 [hep-ph]`.

[86] E. Masso, S. Mohanty, and S. Rao, "*Dipolar Dark Matter*", Phys. Rev. **D80** (2009) 036009, `arXiv:0906.1979 [hep-ph]`.

[87] T. Banks, J.-F. Fortin, and S. Thomas, "*Direct Detection of Dark Matter Electromagnetic Dipole Moments*", `arXiv:1007.5515 [hep-ph]`.

[88] V. Barger, W.-Y. Keung, and D. Marfatia, "*Electromagnetic properties of dark matter: dipole moments and charge form factor*", `arXiv:1007.4345 [hep-ph]`.

[89] S. Chang, N. Weiner, and I. Yavin, "*Magnetic Inelastic Dark Matter*", `arXiv:1007.4200 [hep-ph]`.

[90] G. Belanger, F. Boudjema, A. Pukhov, and A. Semenov, "*Dark matter direct detection rate in a generic model with micrOMEGAs2.1*", Comput. Phys. Commun. **180** (2009) 747–767, `arXiv:0803.2360 [hep-ph]`.

[91] A. d. Saint-Exupéry, *The Little Prince*. Reynal & Hitchcock, 1943.

[92] B. Schneider, "*Study of potential curves of xenon with other rare-gas atoms*", Journal Of Chemical Physics **58** (1973) no. 10, 4447–4451.

[93] R. Gordon and Y. Kim, "*Theory for forces between closed-shell atoms and molecules*", Journal Of Chemical Physics **56** (1972) no. 6, 3122.

[94] I. Tilinin, "*Elastic-scattering of medium energy electrons and positrons by complex atoms*", Zhurnal Eksperimentalnoi I Teoreticheskoi Fiziki **94** (1988) no. 8, 96–103.

[95] H. Ludde, "*Time-dependent density functional theory in atomic collisions*", in *Many-Particle Quantum Dynamics in Atomic and Molecular Fragmentation*, vol. 35 of *Springer Series on Atomic, Optical, and Plasma Physics*, pp. 205–220. Springer-Verlag Berlin, 2003.

[96] Y.-D. Chan *et al.*, "*MaGe - a Geant4-based Monte Carlo framework for low-background experiments*", `arXiv:0802.0860 [nucl-ex]`.

[97] **GEANT4** Collaboration, S. Agostinelli *et al.*, "*GEANT4: A simulation toolkit*", Nucl. Instrum. Meth. **A506** (2003) 250–303.

[98] A. Fukasawa, K. Arisaka, H. Wang, and M. Suyama, "*QUPID, a single photon sensor for extremely low radioactivity*", Nucl. Instrum. Meth. **A623** (2010) 270–272.

[99] R. Brun and F. Rademakers, "*ROOT: An object oriented data analysis framework*", Nucl. Instrum. Meth. **A389** (1997) 81–86.

Index

Erklärung:

Ich versichere, dass ich diese Arbeit selbstständig verfasst habe und keine anderen als die angegebenen Quellen und Hilfsmittel benutzt habe.

Heidelberg, den 26. 11. 2010

....
(Felix Kahlhöfer)